Precision Photometric and Astrometric Calibration for Exoplanet Imaging

By

Ananya Sahoo

A thesis submitted to
The Graduate University for Advance Studies, SOKENDAI
for the degree of
DOCTOR OF PHILOSOPHY

Department of Astronomical Science
School of Physical Sciences
The Graduate University for Advance Studies, SOKENDAI, JAPAN
August 2020

ABSTRACT

With the development of high contrast imaging techniques, direct imaging of faint companions or circumstellar disk at a small angular separation from the stellar hosts is now viable. In order to constrain the properties of companions, photometric and astrometric calibrations has to be done very precisely. Often coronagraphs are used to occult the on-axis starlight so as to image faint companions. Performing relative photometry and astrometry of the companion with respect to the host star is difficult in post coronagraphic images as central starlight cannot be directly used as a photometric and astrometric reference. My approach is to add fiducial incoherent copies of the host star in the image plane and alternate the spatial pattern of these copies between exposures. Subtracting two frames with different calibration patterns helps in removing static and slowly varying incoherent speckle halo components without losing calibration references for each frame. We implemented this on-sky by modulating the deformable mirror of the Subaru Coronagraphic Extreme Adaptive Optics instrument at high speed to generate artificial incoherent speckles. The photometric and astrometric stability of these artificial speckles for 10 second frame exposures were measured to 0.3% and 1.7 mas precision in H-band respectively over a cadence of 30 seconds. The measurements do not show correlated residuals, indicating that residual noise averages as the inverse square root of number of exposures in longer time series. The technique is now currently used at the Subaru Telescope for regular science observations.

DEDICATION

This thesis is dedicated to all the women in science who
strive forth unwavering in their pursuit of knowledge despite all adversities.

ACKNOWLEDGMENTS

I am indebted to many institutions and even more so to the people who constantly motivated and supported me during the course of my graduate studies. I would like to thank the Department of Astronomical Sciences, The Graduate University for Advanced Studies (SOKENDAI), the National Astronomical Observatory of Japan (NAOJ) and the Subaru Telescope for making it possible for me to pursue a PhD while being a regular member of the vibrant astronomy community at the Subaru Telescope.

My greatest gratitude is towards my advisor Prof. Olivier Guyon for his constant wisdom, tireless support and unending encouragement. I still remember the very many skype calls he made and emails he sent for making it possible for me to be a part of the SCExAO team which is the best exoplanet instrumentation team at one of the biggest telescopes in the world. Throughout my doctoral studies he has given me the much needed independence to pursue my ideas. I would also like to thank my co-supervisors Prof. Yosuke Minowa who not only provided me meaningful feedback on my thesis but also helped me countless times in dealing with the administrative work, and Prof. Takayuki Kotani and Prof. Naruhisa Takato for giving me an opportunity to apply the work I carried out in developing certain aspects of the new REACH module which will be used to study high resolution spectra of exoplanets around nearby stars.

The researchers who were a part of my thesis committee, Prof. Yutaka Hayano, Prof. Jun Nishikawa, Prof. Masatoshi Ohishi, Prof. Norio Narita and Prof. Hajime Kawahara, have also helped me in improving the work that I presented in this thesis. It is their detailed feedback and comments that encouraged me to explore certain subtle aspects of my research which otherwise might have gone unnoticed.

It was not just the support and supervision of the people I have mentioned thus far which made my time in Subaru an immense yet fun-filled learning experience, other (current and former) members of the SCExAO team have come forward any and every time I needed them, be it for a professional cause or during a personal crisis. Dr Julien Lozi, Dr Sebastien Vievard, Dr Nemanja Jovanovic, Dr Vincent Deo, Dr Prashant Pathak and Dr Garima Singh have helped me dive into

and develop critical insights necessary to pursue a career ahead in research, particularly in the field of adaptive optics.

The fraternity at the Subaru Telescope is not just composed of scientists and researchers, there are many whose contributions often go unnoticed — for instance they are not often acknowledged in scientific articles. Nevertheless, their input to my work is second to none. I am forever indebted to the technical staff and the administrators at Subaru especially Ms Carolyn Medeiros, Ms Rieko Murai and Ms Noriko Otsuki. I would also like to thank Dr. Kathy Guyon for always including me in all the American festivals and helping me develop a fondness for cats.

I would also like to thank my friends in Hawai'i especially Amy Durham, John Kuntz, Alex Walter, Wailea Collins, Garrette Collins, Zander Carver, Mikkel Gantzler, Blaire Langston, Talei Elizabeth for their fun company, hikes, late night cooking and painting parties and never letting me be homesick. The list can go on and on but like everything memorable in life, including but not exclusive to the time I spent in Hawai'i, this too has to come to an end.

I take a brief moment to acknowledge the constants in my life: my parents, Mr. Bhagyarathi Sahoo and Mrs. Sanjukta Sahoo, my brother Anshuman for always believing in me and my best friend Kaushal Gianchandani for always motivating me to be the best version of what I can be.

I hope many a future astronomer gets to experience the unique culture and environment of Hawai'i. It is truly heaven on Earth for those of us who love to gaze at the night sky.

Table of Contents

List of Figures

List of Tables

List of Abbreviations

AO	Adaptive Optics
AO188	Subaru 188-elements Adaptive Optics system
APD	Avalanche Photo Diode
CHARIS	Coronagraphic High Angular Resolution Imaging Spectrograph
COMICS	Cooled Mid-Infrared Camera and Spectrograph
DM	Deformable Mirror
ExAO	Extreme Adaptive Optics
FIRST	Fibered Imager foR a Single Telescope
FOCAS	Faint Object Camera And Spectrograph
FOV	Field of View
FPWFS	Focal Plane Wavefront Sensing
IFS	Integral Field Spectrograph
IR	Infrared Wavelength Regime
IRCS	Infrared Camera and Spectrograph
IRD	Infrared Doppler
IRDIS	The infra-red dual imaging and spectrograph
GPI	Gemini Planet Imager
HDS	High Dispersion Spectrograph

HSC	Hyper Suprime-Cam
HWP	Half Wave Plate
HZ	Habitable Zone
LGS	Laser Guide Star
MagAO	Magellan Adaptive Optics
MEC	MKID Exoplanet Camera
MOIRCS	Multi-Object Infrared Camera and Spectrograph
NCPA	Non-Common Path Aberrations
NGS	Natural Guide Star
NIR	Near Infrared wavelength regime
OAP	Off Axis Parabolic
P1640	Project 1640
PyWFS	Pyramid Wavefront Sensor
QE	Quantum Efficiency
REACH	Rigorous Exoplanetary Atmosphere Characterization with High dispersion coronography
RMS	Root Mean Square
RTC	Real Time Control
SCExAO	Subaru Coronagraphic Extreme Adaptive Optics
SHWFS	Shack Hartmann Wavefront Sensor
SPHERE	Spectro Polarimetric Highcontrast Exoplanet REsearch
SR	Strehl Ratio
VAMPIRES	Visible Aperture Masking Polarimetric Imager for Resolved Exoplanetary Structures

VIS	Visible Bench
WFS	Wavefront Sensor
ZIMPOL	Zurich Imaging Polarimeter

Chapter 1

Exoplanets and their Direct Imaging

An exoplanet or extrasolar planet is defined as a planet found outside our Solar System. The first exoplanet was discovered in the year 1992 orbiting around the pulsar PSR B1257+12 by the astronomer Aleksander Wolszczan and Dale Frail by time series analysis of the periodic signal from the pulsar [Wolszczan and Frail (1992)]. Three years later, two Jupiter like exoplanets were discovered orbiting around Sun-like star 51 Pegasi and 70 Virginis [Mayor and Queloz (1995), Marcy and Butler (1996)]. Presently around 4200 exoplanets have been confirmed via various detection techniques. Out of these confirmed exoplanets, only 1% have been directly imaged and the rest of them are discovered through various indirect detection methods such as radial velocity, transit, microlensing, pulsar timing variation, disk kinematics etc [Sartoretti and Schneider (1999), Lovis and Fischer (2010), Seager and Deming (2010)]. A detailed statistical distribution of the exoplanets can be seen from figure 1.1, which shows the number of exoplanets detected each year by different detecting methods. Figure 1.2 provides a distribution of exoplanets as a function of their mass and orbital time period and we infer that the exoplanets discovered till date by direct imaging resemble more of a warm young massive planet with size similar to that of the Jupiter on large orbits. Whereas, transit and radial velocity methods have been successful in detecting planets placed in the Habitable Zone (HZ) [Turbet et al. (2016), Barstow and Irwin (2016), Jenkins et al. (2015)]. The radial velocity method infers the presence of a planet by measuring the Doppler shift in the spectrum of the host star [Lovis and Fischer (2010)]. The radial velocity method reveals the orbit, mass of a planet. The transit detection method reveals the radius, atmospheric composition (via transit spectroscopy) [Schneider (1994)]. Together with these two indirect methods, we can

characterize an exoplanet. However, the combination of both the transit and the radial velocity method limits the sample size, data quality and thus lowers the chances of detecting an exoplanet.

Contrary to this, the direct imaging of an exoplanet which literally means capturing the images of an exoplanet provides the information about the planet's orbit (via multi-epoch observations), surface features, temperature and atmosphere composition (via dispersing the exoplanet's light through a spectrograph)[Marois, Macintosh, et al. (2008), Kalas et al. (2008), Seager and Deming (2010)]. The discovery of the exoplanet Fomalhaut b furthermore lead to the study of planet-star interaction, constrained the planet's mass and validated the presence of a circumstellar disk [Chiang et al. (2009)]. The discovery of four planets around HR 8799 has enormously contributed towards understanding the dynamics of a planet-star system [Jason J Wang et al. (2018), Madhusudhan, Burrows, and Currie (2011), D. C. Fabrycky and Murray-Clay (2010)] and revolutionized the field of direct imaging. The direct imaging is not as simple as it sounds. The key challenges lie in the fact that the light reflected or emitted from an exoplanet is often overshadowed in the presence of the host starlight and we lack technologies which can provide high angular resolution (< 1") and detect fainter companions ($\sim$4 -10 magnitudes fainter than the central host). On top of these challenges, the presence of atmospheric turbulence, instrumental aberrations hinders the process of direct detection by broadening the Full Width Half Maximum (FWHM) of the Airy disk (as will be discussed in later section, the image of a point source such as stars taken with a telescope an Airy disk. The size of this disk depends on the primary diameter of the telescope.), speckles etc. As a result of these, direct imaging works well in detecting self luminous planets with wide orbits. However, together with the development of large (35-40m) telescopes equipped with Adaptive Optics (AO) systems, coronagraphy, wavefront control techniques and data analysis, spectroscopy, the detection of Earth-like exoplanets may be feasible in the next decade. In this chapter I will limit my discussions to the direct imaging technique.

1.1 Adaptive Optics Concepts

The light rays from a celestial source for most part of its journey travels uninterrupted through space till it reaches Earth's atmosphere and then the imaging instrument. The atmospheric turbulence can be understood as the fluctuations in the air density or temperature variations leads to changes in the

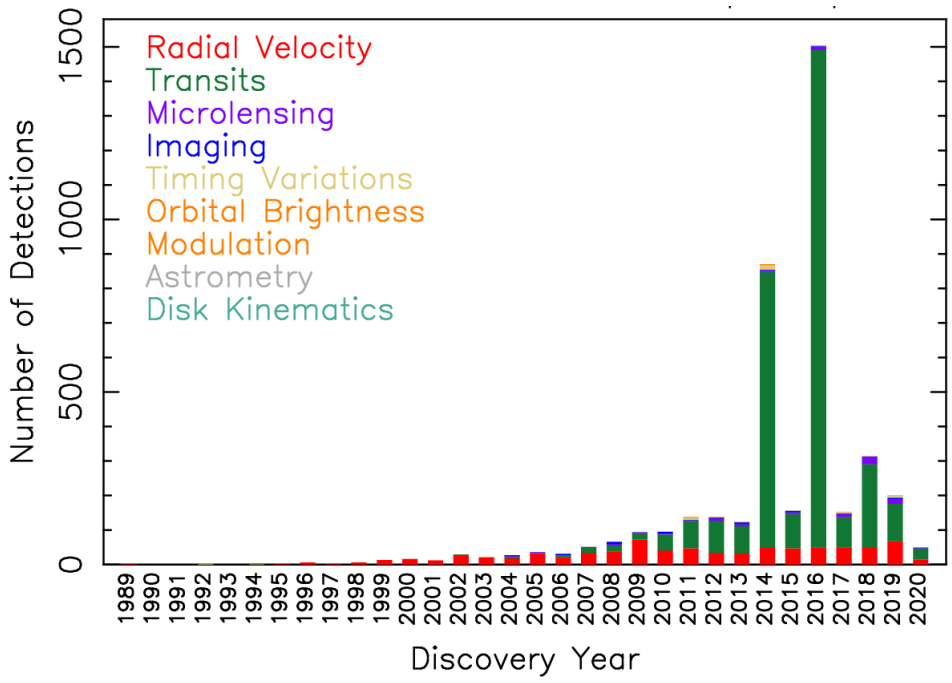

Figure 1.1 Number of exoplanets detected each year. Picture Courtesy: *https://exoplanetarchive.ipac.caltech.edu/*

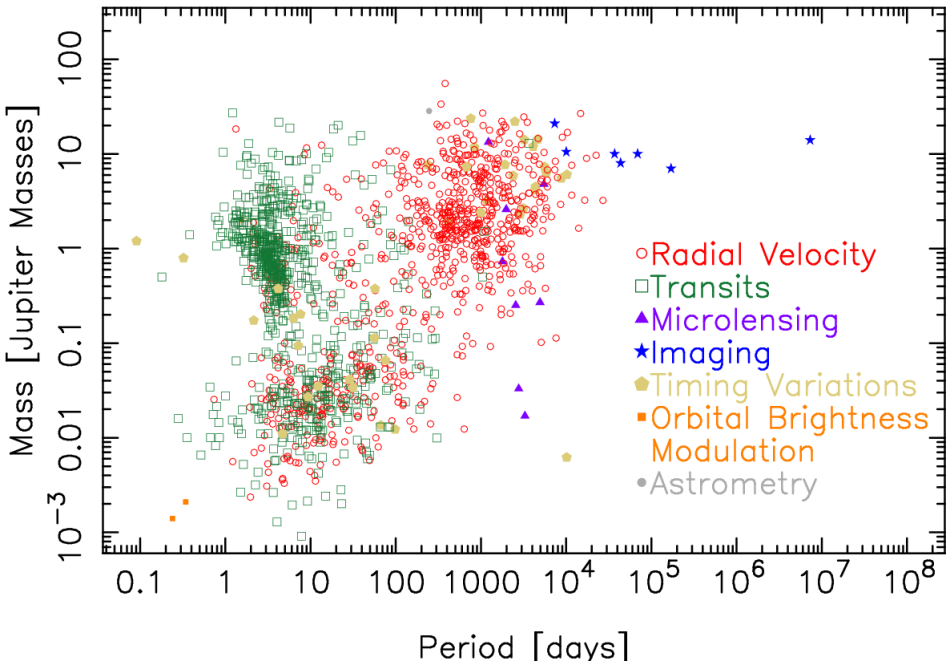

Figure 1.2 Exoplanets distribution as a function of Mass and Orbital Time Period. Picture Courtesy: *https://exoplanetarchive.ipac.caltech.edu/*

refractive index of the air and distorts the incident wavefront. This wavefront distortion degrades the quality of the image by blurring, deforming or destabilizing the image. An Adaptive Optics (AO) system measures this distortion and compensate these effects in real time. Babcock (1953) first proposed the concept of reducing the distortion in the incoming wavefront due to atmospheric turbulence using deformable mirrors. Some of the early uses of this concept involved tracking of Soviet satellites by US millitary during the Cold War [Tyson (2015)]. Later, Rousset et al., 1990 successfully demonstrated that AO systems can be used to achieve diffraction limited images using the European Southern Observatory's 3.6m telescope at La Silla, Chile.

1.1.1 Image formation by a Telescope

Using Fraunhofer diffraction theory in the far-field approximation, the electric field $E(r,t)$ due to a point source at the focal plane of a telescope of circular aperture is given by:

$$E(r,t) = \frac{Ae^{i(wt-kz)}}{z} 2\pi a^2 \left(\frac{z}{kRr}\right) J_1\left(\frac{kRr}{R}\right) \tag{1.1}$$

where r denotes the distance from center of the focal plane, t denotes time, A is the amplitude of the incident beam in the pupil plane, z is the distance between the pupil plane and the point at which electric field is measured, R is the radius of the circular aperture, $k = 2\pi/\lambda$ and J_1 denotes the Bessel function of the first kind. The intensity $I(r)$ in the focal plane is given by:

$$I(r) := < |E(r,t)|^2 > = \frac{2A^2\pi^2R^4}{z^2} \left[\frac{J_1(kRr/z)}{kRr/z}\right]^2 \tag{1.2}$$

The equation 1.2 is the Point Spread Function (PSF) for a telescope with circular aperture and is called an Airy disk. At $r = 0$, the maximum peak intensity $I(0)$ is given by:

$$I(0) = \frac{2A^2\pi^2R^4}{z^2} \tag{1.3}$$

Intensity in terms of angle θ (where θ is the angle between the centre of the Airy disk and any point in the focal plane) can further be defined as:

$$I(\theta) = I(0) \left[\frac{J_1(kR\sin\theta)}{kR\sin\theta}\right]^2 \tag{1.4}$$

Therefore, in an idealized environment i.e. when we have a flat wavefront at the pupil, the resolution of an image is limited by the instrument's aperture size. Figure 1.3 (a) provides the

(a) No turbulence **(b)** With turbulence

Figure 1.3 (a) Simulated image of a PSF obtained in the absence of atmospheric turbulence by telescope with circular aperture with zero phase aberrations (Airy pattern), (b) Simulated image of the PSF with 0.1 radian rms random phase aberrations.

image of a point source seen through an optical telescope without any atmospheric turbulence. The image obtained is a perfect Airy disk. The angular radius of this Airy disk is $1.22\lambda/D$, where λ is the wavelength of the incident electromagnetic field and D is the diameter of the primary mirror. However, when we add a 0.1 radian rms wavefront fluctuations, we see speckles in the image, and the peak intensity decreases (see figure 1.3(b)). The effect of atmospheric turbulence can be quantified using the Fried parameter r_0 [Fried (1966)]. It is a scalar quantity having the dimension of length and is used to represent in a global way the strength of the refractive index fluctuations over the entire atmosphere. r_0 is dependent on the atmospheric conditions, temperature of the air, the wavelength of the observation (in the case of constant atmospheric conditions). When $D < r_0$, i.e. for small aperture telescopes, the effect of turbulence is negligible. For $D > r_0$, the atmospheric turbulence the resolution of the image quality degrades to $\sim \lambda/r_0$. Further, the height of the peak intensity decreases as more light diffract away from the core. The performance of an optical system can be evaluated using Strehl ratio SR [Strehl (1895)]. It is defined as the ratio of the peak intensity of an aberrated PSF (I) to that of the un-aberrated PSF (I^*) and this ratio is equal to the mean wavefront error ϕ in the pupil plane.

$$SR = \frac{I}{I^*} = | < e^{i\phi} > |^2 \tag{1.5}$$

The main objective of an AO system is to minimize the wavefront error i.e. make the wavefront as flat as possible for scientific studies. This in turn improves the Strehl ratio as more light is now concentrated to the core of the Airy disk and thus enables the detection of nearby fainter sources.

The rest of the subsections discusses how the aberration is detected and compensated by an AO system in real-time.

1.1.2 Wavefront Sensors

A wavefront sensor is a device used to measure the aberration in the wavefront of the incoming light beam across the pupil aperture. The gradient of an wavefront is generally used as metric for the aberrations. For a plane incident wavefront, the gradient is zero i.e. the phase difference between any two incoming light beam is zero. When, the incident beam is aberrated, the gradient is a non-zero quantity and the phase difference between any two points in the pupil may or may not be zero. A WFS computes these phase aberrations from the intensity and position variations of images formed by several sub-apertures across the pupil. Firstly, it collects light from several sub-apertures of the pupil plane and produces multiple images of the incident point source each corresponding to a particular sub-aperture. Secondly, it measures the displacement of these spots from their ideal positions. A commonly used Shack-Hartmann wavefront sensor (SHWFS) is based on this principle [R. V. Shack (1970), Platt and R. Shack (2001), Hartmann (1900)]. Apart from measuring the displacements of spots, one can also measure the intensities of these spots. This is the case for a Curvature Wavefront Sensor. A simple Curvature based wavefront sensor measures intensities of two defocused images one placed before the focal plane and other behind the focal at same separations from the focal plane. These intensities are then used to measure the spherical curvature of the wavefront [Francois Roddier (1988)]. The more recently developed Pyramid wave front sensor has gained much popularity because of its higher sensitivity than a Shack-Hartmann wavefront sensor in detecting small wavefront errors [Ragazzoni and Farinato (1999)]. This WFS is now preferred for doing extreme AO corrections. A pyramid WFS uses a prism to split the PSF and reconjugate four wavefront-encoded pupil like images. The optical setup is similar to the Foucault's knife edge measurement test. In the case of no optical aberrations, all the four images will be identical to each other. In the presence of aberrations, the intensity distribution will be different among the four images. This change in intensity distribution is recorded to compute wavefront gradients [Ragazzoni (1996)]. The choice of choosing a WFS depends on the degree of the wavefront correction, wavelength of operation, luminosity of the source and on the nature of the atmospheric turbulence.

1.1.3 Wavefront Reconstruction and Control

The primary goal of a wavefront reconstruction tool is to convert the measurement-outputs from a WFS into a set of commands to be sent to the wavefront corrector. The corrector then uses these commands to change the shape of the incoming wavefront beam. Therefore, at the end the science detector achieves a flat unaberated wavefront. The outputs from a WFS can be represented in terms of a vector W. The shape of this vector depends on the nature of the WFS used. Assuming a linear relation between WFS and corrector command ϕ, it can represented as follow:

$$W = A\phi \tag{1.6}$$

where A is the response matrix for the AO system. A is experimentally predetermined by measuring W at first for a known corrector configuration. Therefore, the command to be sent to the corrector is computed by multiplying the generalised inverse, compensated for small singular values of A with recent W:

$$\phi = A^{-1}W \tag{1.7}$$

There are broadly two methods of reconstructing wave-fronts:(1) zonal reconstruction method, (2) modal reconstruction method. The main difference between these two methods is the type of basis set used to calculate the command to the wavefront-corrector. In the case zonal wavefront sensing method, the wavefront is represented in terms of the optical path difference and the local gradient over a small number of independent sub-apertures called zones. In the case of modal wavefront sensing, the wavefront is represented in terms of Zernike polynomial which forms a complete orthogonal basis. Using zonal reconstruction method, the wavefront error is corrected at fixed spatial frequency and this spatial frequency can be easily expanded by increasing the number of zones. Whereas with modal reconstruction, higher order optical aberrations are difficult to measure and compensate. This approach also generates smooth phase maps which is easier to implement. In most practical cases it is difficult to calculate the exact inverse because of the computation limit, or when the matrix itself cannot be inverted, or when we want to ignore certain WFS measurements because of low signal-to-noise ratio. In such cases, we compute a regularized pseudo inverse of the response matrix by using the Singular Value Decomposition method.

1.1.4 Wavefront Correctors

A wavefront corrector is a device with flexible surface used to change the shape of the aberrated wavefront. There are broadly three types of wavefront corrector: deformable mirror, segmented mirror and bimorph mirrors. A deformable mirror (DM) comprises of a thin continuous reflective faceplate placed on the top of an array of actuators. The actuators are made up of multilayer piezoelectric substances and poke the faceplate to deform it's surface as desired. A base plate made up of similar material as the faceplate, holds the actuators together. As evident from the name, a segmented mirror comprises an array of mirrors packed closely either in triangular, square or hexagonal arrangement. Each segment has three degree of freedom and zero cross talk. Similar to the DM, a bimorph mirror consists of a continuous faceplate with disk shaped actuators attached to it through a layer of piezo material. The quality of wavefront correction also depends on the parameters of corrector such as the number of actuators, actuator pitch, stroke, response time, minimal cross-talk between the neighbouring actuators, influence function.

1.1.5 Closed AO loop operations

An AO system includes one or more WFS(s), one or more DM(s), a Real Time Control (RTC) system and a science camera. A conceptual diagram of an AO system is depicted in the figure 1.4. As can be seen from figure 1.4, at first the incident aberrated wavefront is reflected by the DM. A part of this incident light beam then reflected and falls on a WFS and the rest of the beam is transmitted and is incident on the science camera for direct imaging. The WFS measures the optical aberrations and sends command to the RTC. The RTC computes the command to be send to the DM from wavefront measurements. Finally, the DM receives command from the RTC to modify its surface in a way so that incident aberrated wavefront can be reflected as flat from its surface. After this complete cycle, the science camera receives a flat wavefront which upon focusing, yields diffraction limited image to conduct scientific studies. The quality of wavefront correction depends on a numerous factor such as the type of DM, WFS, speed of operation of the AO loop, brightness of the celestial source. A detailed quantitative analysis of this topic can be found in Hardy (1998), François Roddier (1999) and Tyson (2015).

Adaptive optics systems optimized to deliver extreme wavefront corrections to image an exo-

planet or circumstellar disk are called Extreme Adaptive Optics system (ExAO). Normally these systems take coarsely corrected AO light from the generic facility AO instrument and perform fine corrections using only the on-axis starlight. These systems high strehl ratio 0.8 in H-band.

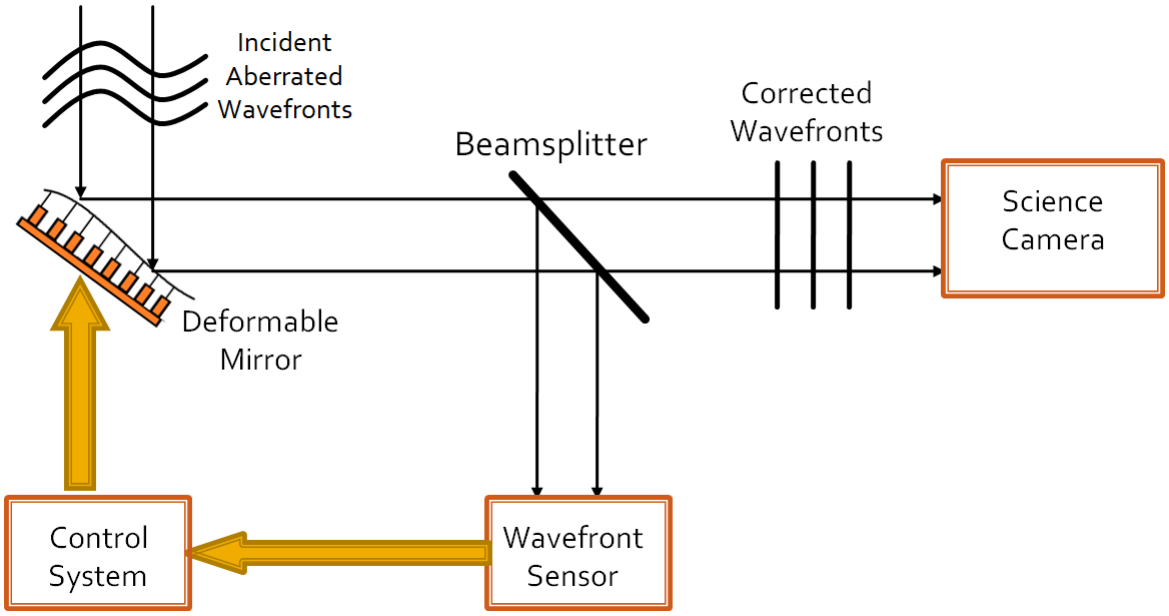

Figure 1.4 Conceptual diagram of an Adaptive Optics system that senses and corrects wavefront. The incident aberrated wavefront is reflected by the DM. A part of this incident light beam is further reflected and falls on a WFS and the rest of the beam is transmitted and is incident on the science camera for direct imaging. The WFS measures the optical aberrations and sends command to the RTC. The RTC computes the command to be send to the DM from wavefront measurements. Finally, the DM receives command from the RTC to modify its surface in a way so that incident aberrated wavefront can be reflected as flat from its surface. After this complete cycle, the science camera receives a flat wavefront which upon focusing, yields diffraction limited image to conduct scientific studies

1.2 Coronagraphic Imaging

A coronagraph is an optical element (or a mask) placed in the pupil or focal plane of the detector and is used to block the on-axis starlight as well as suppress the diffracted starlight surrounding the PSF core. Coronagraph was invented by the French astronomer Bernard Lyot to image the Sun's corona [Lyot (1939)]. Later on this technology was adapted to image exoplanets [Nakajima (1994), Sivaramakrishnan, Koresko, et al. (2001)]. An ideal coronagraph optimized to image Earth-like planet should deliver high contrast (i.e. intense dark zones created around the PSF's core) at close separation to the host. Limited by its fixed shape, it can only block the static diffraction pattern in the focal plane. Figure 1.5 (left) shows an image obtained by subtracting two consecutive

frames with central PSF unblocked by a coronagraph and 1.5 (right) shows the image obtained by subtracting two frames where the central PSF is blocked by a coronagraph. From a qualitative point of view, we can see that there is a relatively lower speckle noise in figure 1.5 (right) than in figure 1.5 (left). Thus, adding a coronagraph, improves the contrast and reduces the photon noise due to bright central stellar PSF. A detailed review about the type and properties of the coronagraphs can be found in Olivier Guyon, Pluzhnik, et al. (2006).

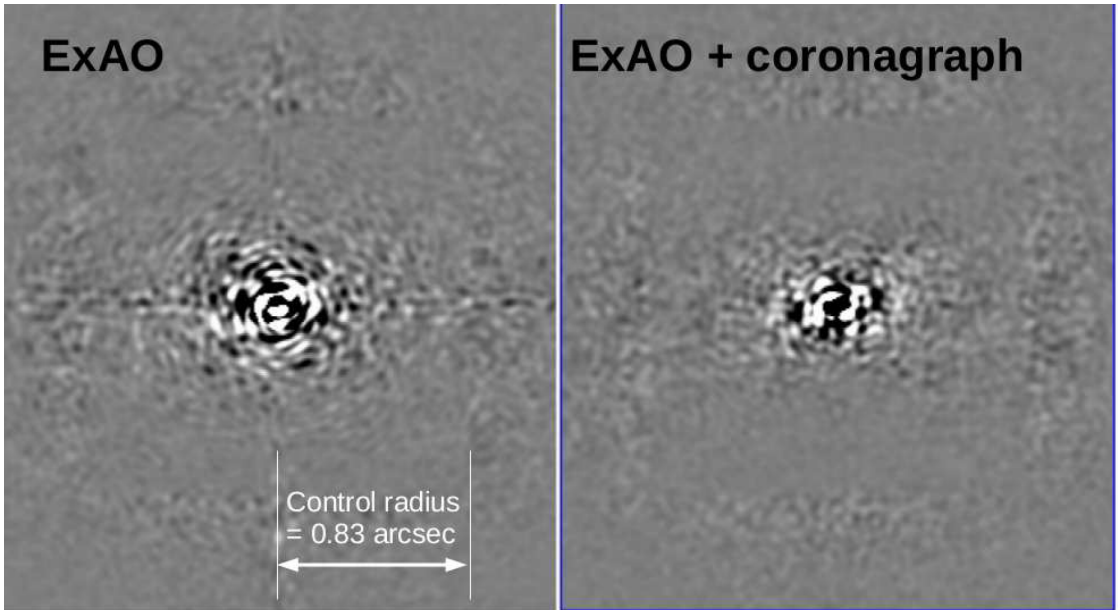

Figure 1.5 PSF subtracted extreme AO images (left) without coronagraph (right) with coronagraph. Adding a coronagraph improves the contrast and reduces the photon and speckle noise due to stellar background. Picture courtesy: Olivier Guyon (2018)

1.3 Post-processing Techniques

Even after the extreme AO correction, the final image taken by the science detector contains residual speckles. These speckles are mostly formed due to the aberrations which goes "unseen" by the WFS. The aberrations which are present in the optical path between corrected wavefront and the science detector goes unnoticed by the WFS. These aberrations are called Non-Common Path Aberrations. For example in the figure 1.4, the NCPA aberrations between the beamsplitter and the science camera is undetected by the WFS and this form residual speckles in the image which can mimic a planet signal. Various post-processing methods are used to subtract these residual speckle noises from the image. These are briefly discussed below:

- **Angular Differential Imaging (ADI)** In this technique a set of consecutive images are acquired where the telescope's tracking rotator is turned off. Or apparently, the sky is allowed to rotate, while the detector relative position remains fixed. A planet if present, will also rotate with the same parallactic angle as of the host star, where as the intrinsic residual speckles will not follow the same rotation. Subtracting two images with different rotations will enable detecting exoplanets [Marois, Lafreniere, Doyon, et al., 2006].

- **Spectral Differential Imaging (SDI)** This technique conveniently applies to the case where the images are taken by a spectrograph. During an exposure, a spectrograph takes images at several different wavelengths. The distance of the residual speckles from the center of the core to a first order approximation scales linearly with the wavelength. Also, the intensity of the speckle varies inversely with the square of the wavelength. A companion signal is invariant to this phenomenon, and is the working principle for the SDI method [Racine et al. (1999),Marois, Doyon, et al. (2000)]. A detailed analytical discussions about the nature of the speckles will be presented in Chapter 2.

- **Polarimetric Differential Imaging (PDI)** The method is based on the concept that the starlight reflected by the planet's atmosphere or circumstellar disk is polarized. Output from an ExAO system is imaged at two different orthogonal polarisations. Subtracting two images with orthogonal polarisations is used to detect faint companions and characterize debris disk [B. Norris et al. (2015), Roelfsema et al. (2010), Canovas et al. (2013)].

1.4 Current Extreme AO Projects

The search for planets in the habitable zone and 'exo-life' is the main motivation for the development of ExAO sytems. The residual wavefront aberrations induces speckle noises in the image plane. The size of the speckles is diffraction limited (λ/D) and they can mimic planet signal. The main objective of the ExAO system is to eliminate this speckle noise via coronagraphy, higher order wavefront correction, post-processing techniques. Apart from detecting planets, these ExAO systems also include modules which acquire high resolution spectra ($\frac{\Delta R}{R} \sim 100 - 100,000$) which can be useful to study the atmosphere of the planet. Table 1.1 provides the list of current ExAO systems around the world including the type of WFS, number of DM actuators across the pupil and the name of

Table 1.1 Current ExAO Projects

NAME	Telescope	Year of Operation	DM	Primary WFS	Science Instrument
P1640	Palomar	2012-17	66	SHWFS	IFS
GPI	Gemini South	2014-	50	SHWFS	IFS
SCExAO	Subaru	Development+2012-	50	PyWFS	CHARIS, VAMPIRE
SPHERE	VLT	2014-	50	PyWFS	IFS, IRDIS, ZIMPOL
KPIC	Keck	2019-	32	PyWFS	NIRSPEC
MagAO-X	Magellan	Development+2019-	50	PyWFS	IFS

the science modules present in these instruments.

Chapter 2

Photometric and Astrometric Calibrations in Coronagraphic Images

2.1 Introduction

In this chapter I discuss the methodologies currently used to measure the brightness and position of a companion in ExAO coronagraphic images. Accurate measurement of the exoplanet flux and position in post AO-corrected images is essential for orbit determination and characterization (chemical composition, mass, effective temperature). Precise astrometry can be useful to confirm companionship (via common parallactic and proper motion) at a timescale smaller than the regularly used proper motion measurement techniques alone (Zimmerman et al., 2010). The relative flux measurement between the companion and the stellar host can reveal their physical properties such as atmospheric composition, mass, radius etc. Any periodic flux modulation of the planet-light curve will help us constraint the properties of atmosphere, cloud structures and evolution. From rotational modulation, we can phase map the cloud decks, and the slow evolution of the light curve can provide insight into the atmospheric dynamics [Apai et al., 2016]. Time resolved precise photometry has enabled us to measure the sinusoidal modulation of the flux and thereby measure the rotational period of the exoplanet 2M1027b [Zhou et al. (2016)]. Another application of precise photometry would be to study the dependence of cloud structures, effective temperature on the surface gravity [Marley and Sengupta (2011),Marois, Zuckerman, et al. (2010)]. A brief discussion about the scientific use of relative flux measurements is discussed in Section 2.2. Photometric and astrometric measurements rely mostly on how one precisely measures the PSF core's position and flux. In the case of a non-coronagraphic images, the relative brightness between a companion and its host star is easily measured from the relative flux counts received during an exposure, thanks

to the presence of the PSF of star (can be treated as reference object to calibrate the faint nearby companion). Further, the effect of Strehl ratio (considered to be the same for both the companion and the host) is removed by taking the flux ratio between the companion and host. Thus the final measurement is limited by the photon noise, detector readout noise and residual speckles. However, in coronagraphic ExAO corrected images the setup is different; the on-axis host starlight is now occulted by a coronagraph. It is difficult to calibrate the companion light without any reference source in the common field of view. In such cases, usually astronomers calibrate the flux and position of the obscured PSF with a different known reference source at a different observation epoch, or they measure the PSF flux before and after placing the coronagraph. This measurement is further used to calibrate the planets or circumstellar disk. In this coronagraphic case, there is no-axis reference source to directly track the Strehl factor for each exposure. In addition to Strehl, several other factors can be responsible for alteration of the PSF brightness and location. For space based AO observations, thermal instability, vibrations can alter the PSF position and flux. For ground based AO systems, slow drift of the optical elements in the AO system, field rotation, residual background speckles generated due to Adaptive Optics residual wavefront errors etc, introduces small drift in the PSF's position. Sky absorption (or transmission) and varying atmospheric seeing changes the measured brightness of the PSF. Therefore, the flux count of the PSF on the detector will vary with time. The method of measuring the flux and position of unsaturated host PSF without coronagraph, and then using it to calibrate the flux of companion is less accurate and prone to large errors. As evident now, we need a dynamic calibration of the coronagraphic PSF during an observation sequence to monitor the flux and position of the occulted PSF behind the coronagraph. Section 2.3, 2.4, 2.5 briefly discusses the solutions to track the PSF flux and positions by using information from a closed AO loop operation to track the central PSF, or create off-axis copies of the central PSF by modulating the pupil plane.

2.2 Stellar Flux Concepts

In this section, I discuss the concepts behind measuring the stellar and companion flux. A star is treated close to a black body as it can emits electromagnetic radiations across all wavelength regime and is in thermal equilibrium. From the Planck radiation law, the spectral radiance $B(\lambda, T)$ (or

specific intensity at a given wavelength) is defined as follows:

$$B(\lambda, T) = \frac{2hc^2}{\lambda^5} \frac{1}{e^{\frac{hc}{\lambda K_B T}} - 1} \tag{2.1}$$

where h is the Planck constant, T is the absolute temperature, $K_B B$ is the Boltzmann constant and c is the speed of light in the medium. In equation 2.1, we see that by measuring intensity of star light, we can calculate the temperature of the star. Stellar flux $f_\lambda(m)$ can a expressed as a function of apparent magnitude m and the zero point magnitude a in a spectral band:

$$f_\lambda(m) = 10^{a-0.4m} \tag{2.2}$$

Direct imaging allows convenient measurement of planet flux as well the star flux. The relative flux measurement can reveal various planetary characteristics such as the geometric albedo, temperature and radius. In visible imaging wavelength region, the contrast C_{vis} can be expressed as:

$$C_{vis} = \frac{f_c}{f_s} = p\phi(\alpha) \left(\frac{r}{a}\right)^2 \tag{2.3}$$

where f_c is reflected planet light flux, f_s is the flux of the star, p is the geometric albedo, r radius of the planet, $\phi(\alpha)$ is the integral phase function and a separation between the planet and the star. Table 2.1 shows the geometric albedo for our planets in the solar system. Constraining the albedo parameter will us to characterize a given exoplanet with the set up planets known to us. In infrared wavelength regime, the infrared contrast C_{ir} between the planet and host star depends on the effective temperatures, their corresponding radii[Seager and Deming (2010), Perryman (2018)]. It can expressed as follows:

$$C_{ir}(\lambda) = \frac{B_\lambda(T_p){r_p}^2}{B_\lambda(T_s){r_s}^2} \tag{2.4}$$

where, $B_\lambda(T_p)$ and $B_\lambda(T_s)$ are the Planck function for the planet and star respectively, r_p and r_s are the radii of the planet and the star. The effective temperature can be measured by fitting the a black-body curve to the experimentally measured C_{ir} contrast. The effective temperatures T_{eff} for the planets in our Solar system is mentioned in table 2.1.

2.3 Instrument Design for Stable Astrometry

As discussed previously in coronagraphic images, the star is occulted and its location cannot be determined in a straight forward manner. In case of no wavefront aberrations the PSF is stable

Table 2.1 Solar System Planet and their Albedo values, Effective Temperature

Planet	Geometric Albedo p	T_{eff} (in K)
Mercury	0.138	433
Venus	0.84	231
Earth	0.367	254
Mars	0.15	210
Jupiter	0.52	124.4
Saturn	0.47	95.0
Uranus	0.51	59.1
Neptune	0.41	59.3

behind the coronagraph thus its position remains intact before and after inserting the coronagraph. Where as in case of wavefront aberrations, PSF has distorted Airy rings with time-varying speckles, and its shape and position changes with time. A small tip tilt wavefront error displaces the PSF position, and it is challenging to track the displacement when a coronagraph is inserted in the beam. Digby et al. (2006) came up with the idea of tracking the PSF drift behind the coronagraphic mask from the information retained in a feedback loop operating at a speed of 1 kHz. Figure 2.1 provides a schematic representation of the experimental setup. This experiment was conducted as a part of The Lyot Project [Ben R Oppenheimer et al. (2004)]. A fast steering mirror (FSM) directs the input beam towards a focal plane mask (FPM) with a occulting spot in its center. The FSM is used to maintain alignment to the beam with occulting spot. Four lenslet array mounted on a fiber head behind the FPM further receives the light and sends it four Avalanche PhotoDiodes (APD). Any drift in the PSF position affects centroid of the APD counts. The tip tilt computer collects this information and maintains the star alignment by adjusting the angle of FSM. This entire feedback loop operates at 1 kHz. The lenslet array is mounted on 2D xy stage. The central star can be moved to any position on the occulting spot by tuning the FSM and successively aligning the lenslet array to the new position. The lenslet array can be moved to a maximum position of $2.5\lambda/D$ from the center of the occulting spot. Thus, the star position can be inferred by changing the lenslets array's motor position. This is explained in detail in the following paragraph.

Initially, the system is calibrated using a binary target, where one of the sources is injected to the

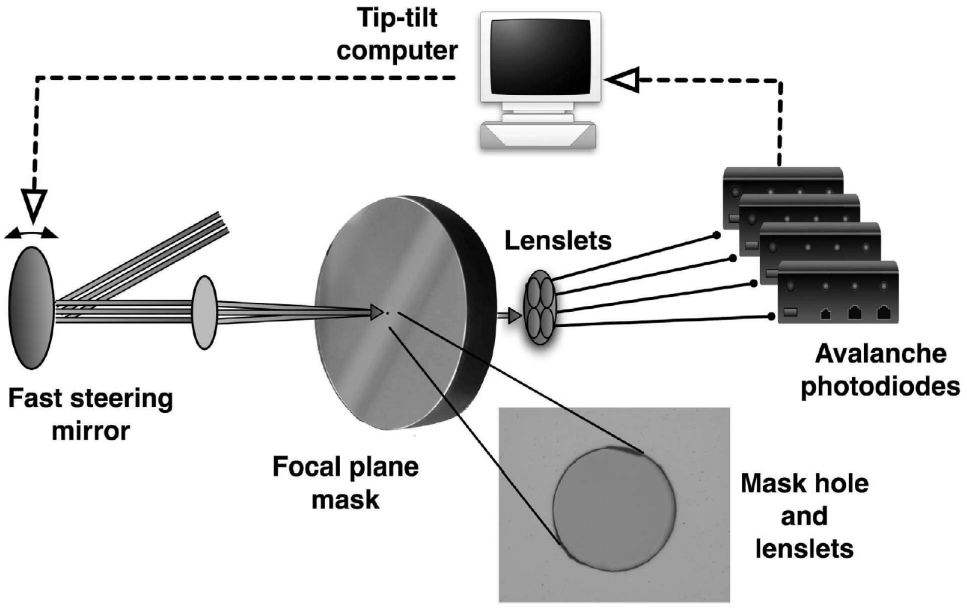

Figure 2.1 Schematic representation of the coronagraphic tip tilt loop from the Lyot Project [Ben R Oppenheimer et al. (2004)]. Any drift of the PSF behind the hole, changes the PSF structure and thereby affects the APD counts. The tip tilt computer takes this information from the APDs to adjust the drift by altering the angle of FSM. Courtesy: Digby et al. (2006)

FPM mask and the other one is used to track the actual position of the injected source. The primary occulted star is then moved by changing the position of lenslet array. The lenslet array position is recorded in the FITS Header file. The star position behind the occulting spot (estimated from the companion's position) and the lenslet array position are then compared. It is found that there exists a linear correlation between the lenslet motor position and the star's pixel position. This relation is further used to calculate the obscured PSF position for other targets. The astrometric precision in this case depends on the precision of the motor stage movement, tip tilt loop measurement precision, readout noise of the APDs, extent of atmospheric dispersion correction, etc. This type of feedback loop is easy to implement in high-contrast extreme AO systems. It can be primarily used to stabilize the core of the PSF. This is the earliest method undertaken to stabilize the PSF's drift behind a coronagraph, and indirectly measure the position of the PSF from the information retained in a feedback loop. However, this method lacks tracking the PSF's flux behind a coronagraph. This is issue is addressed in section 2.4 which discusses a robust way to do simultaneous photometry and astrometry of the PSF situated behind a coronagraph.

2.4 Pupil Plane Phase and Amplitude Modulation

The strong need to have an off-axis calibration source in narrow field post AO corrected images motivated astronomers to create copies of the central stellar target and situate them in coronagraphic dark region. These copies can then be directly used to calibrate stellar host, if present faint companions too. This approach can be considered analog to a multi-slit diffraction experiment. Following Huygens-Fresnel light propagation principle, a periodic slit placed in the path of an input beam will divert light along several directions. With a converging optical element, this diverted rays are focused to form an image with multiple spots. Equivalently, this can also be achieved by introducing a conjugated pupil plane phase and amplitude mask [Marois, Lafreniere, Macintosh, et al., 2006,Sivaramakrishnan and Ben R. Oppenheimer (2006)]. The effect of pupil plane modulation can be described using Fraunhofer diffraction method using far field approximation, i.e. the focal plane is the Fourier transform of pupil plane. Let $A(x, y)$ and $\phi(x, y)$ be the amplitude and phase of the electric field at a point (x,y) in the pupil plane. Then the intensity ($I(k_x, k_y)$) and electric field ($E(k_x, k_y)$) at a point (k_x, k_y) in the focal plane is defined as follows:

$$I(k_x, k_y) = |E(k_x, k_y)|^2 = |\mathcal{FT}[A(x, y)e^{i\phi(x,y)}]|^2 \tag{2.5}$$

and $\mathcal{FT}$ denotes the Fourier transformation. The rest of the subsection discusses effect of amplitude and phase aberrations on the focal plane image.

2.4.1 Amplitude Modulation

Let ϵ be the amplitude modulation mask with a standard deviation σ_{mask} and let $\mathcal{E}$ be the Fourier transform of ϵ . The resultant intensity at the focal plane is computed as follows:

$$\begin{aligned}
I_{amp}(k_x, k_y) &= |\mathcal{FT}[(A + A\epsilon)e^{i\phi(x,y)}]|^2 \\
&= |\mathcal{FT}[Ae^{i\phi(x,y)}] + \mathcal{FT}[A\epsilon e^{i\phi(x,y)}]|^2 \\
&= [\mathcal{FT}[Ae^{i\phi(x,y)}] + \mathcal{FT}[A\epsilon e^{i\phi(x,y)}]][\mathcal{FT}[Ae^{i\phi(x,y)}] + \mathcal{FT}[A\epsilon e^{i\phi(x,y)}]]^* \\
&= [\mathcal{FT}[Ae^{i\phi(x,y)}][\mathcal{FT}[Ae^{i\phi(x,y)}]^* + \mathcal{FT}[Ae^{i\phi(x,y)}]\mathcal{FT}[A\epsilon e^{i\phi(x,y)}]^* \\
&+ \mathcal{FT}[A\epsilon e^{i\phi(x,y)}]\mathcal{FT}[Ae^{i\phi(x,y)}]^* + \mathcal{FT}[A\epsilon e^{i\phi(x,y)}]\mathcal{FT}[A\epsilon e^{i\phi(x,y)}]^* \\
&= |\mathcal{FT}[A(x,y)e^{i\phi(x,y)}]|^2 + E\mathcal{FT}[A\epsilon e^{i\phi(x,y)}]^* + \mathcal{FT}[A\epsilon e^{i\phi(x,y)}]E^* + |\mathcal{FT}[A\epsilon e^{i\phi(x,y)}]|^2 \\
&= I(k_x, k_y) + E(\mathcal{FT}[(Ae^{i\phi(x,y)})\epsilon]^*) + E^*(\mathcal{FT}[(Ae^{i\phi(x,y)})\epsilon]) + |\mathcal{FT}[(Ae^{i\phi(x,y)})\epsilon]|^2
\end{aligned} \tag{2.6}$$

where $*$ denotes the complex conjugate operator. Using Fourier transform convolution theorem, i.e. for two arbitrary functions f and g, $\mathcal{FT}(fg) = \mathcal{FT}(f) \star \mathcal{FT}(g)$ and '$\star$' denotes the convolution operator. Equation 2.6 can be reduced further reduced to:

$$I_{amp}(k_x, k_y) = I(k_x, k_y) + 2\mathcal{R}[E(E^* \star \mathcal{E}^*)] + |E \star \mathcal{E}|^2 \tag{2.7}$$

where $\mathcal{R}$ denotes the real part. If amplitude mask ϵ is chosen to be periodic, then $\mathcal{E}$ is sharply peaked at symmetrical positions. The second and third term in the equation 2.7, therefore are the replicas of the central PSF. If $\mathcal{E} \gg E$ at the maximas of $\mathcal{E}$, the second term in equation 2.7 can be neglected. It can be further simplified as follows:

$$I_{amp}(k_x, k_y) \cong I(k_x, k_y) + |E \star \mathcal{E}|^2 \tag{2.8}$$

The resultant focal plane intensity is due to the convolution of the PSF and the amplitude mask function. The second term in the equation 2.8 denotes copies of the central PSF. These copies are called artificial or satellite speckles. They are used to track the position and flux of the PSF core. The amplitude and location of these satellite spots are determined by the periodicity and thickness of the grid. For a sinusoidal amplitude mask, the brightness of these spots is proportional to ${\sigma^2}_{mask}$ i.e. proportional to the square of the amplitude of the sine wave. The separation of the first-order satellite spot from the central star is equal to the number of cycles of the sine waves times λ/D,

where D is the diameter of primary mirror of the telescope. This technique has been implemented in GPI to create satellite speckles for image calibration [Jason J. Wang et al. (2014)]. Figure 2.2 shows the pupil plane grid deployed on GPI instrument with the satellite spots in monochromatic and poly-chromatic wavelength.

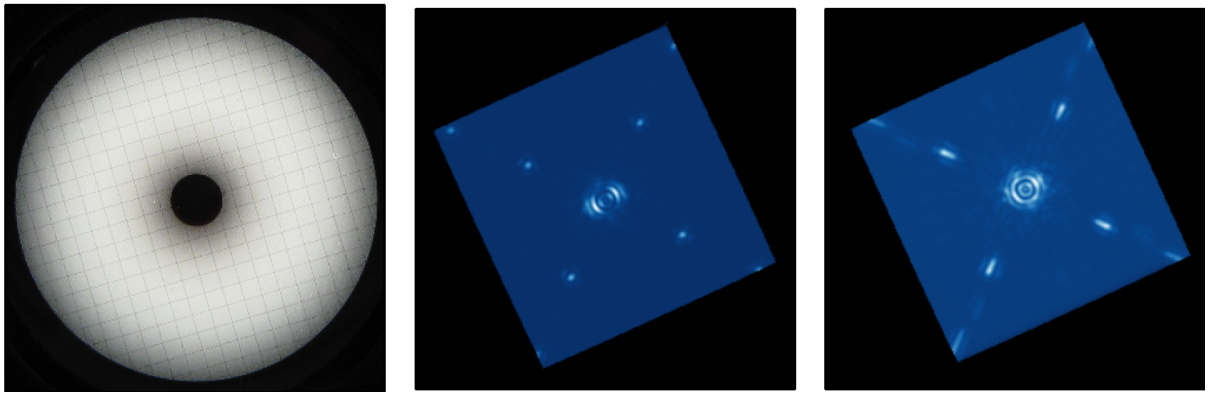

Figure 2.2 Left: An image of the H-band Pupil Plane Grid mask deployed in GPI. Center: Monochromatic image (H-band) showing both the first and second order satellite spots. Right: Broadband image (H-band) showing both the first-order and second-order elongated satellite spots. Picture Courtesy: Jason J. Wang et al. (2014)

2.4.2 Phase modulation

Similarly to the amplitude modulation, the phase of the starlight in the pupil plane can be modulated so as to constructively (or destructively) interfere to create a set of diffraction spots [Marois, Lafreniere, Macintosh, et al. (2006)]. Let $\phi_{mask}(x, y)$ with standard deviation σ_{mask} be the phase aberration introduced to the pupil plane having a Fourier transformation equal to Φ_{mask}. The focal plane intensity can be reduced:

$$\begin{aligned} I_{ph}(k_x, k_y) &= |\mathcal{FT}[A(x,y)e^{i[\phi(x,y)+\phi_{mask}(x,y)]}]|^2 \\ &= |\mathcal{FT}[A(x,y)e^{i\phi(x,y)} \times e^{i\phi_{mask}(x,y)}]|^2 \\ &= |\mathcal{FT}[A(x,y)e^{i\phi(x,y)}(1 + i\phi_{mask} - \frac{\phi^2_{mask}}{2} + \cdots)]|^2 \end{aligned} \tag{2.9}$$

Using Fourier transform convolution theorem, equation 2.9 can be further reduced to:

$$I_{ph}(k_x, k_y) = I(k_x, k_y) - 2\mathcal{I}[E^*(E \star \Phi_{mask})] - \mathcal{R}[E^*(E \star \Phi_{mask} \star \Phi_{mask})] + |E \star \Phi_{mask}|^2 \tag{2.10}$$

Following the arguments in § 2.3.1, the above equations can be further reduced to:

$$I_{ph}(k_x, k_y) \cong I(k_x, k_y) + |E \star \mathcal{E}|^2 \tag{2.11}$$

As discussed in the previous section if Φ_{mask} is chosen to be periodic, the term $|E \star \Phi_{mask}|^2$, introduces copies of central PSF in the focal plane. Thus again we are able to create satellite speckles by modulating the phase instead of amplitude in pupil plane. This feature has been in deployed on several high contrast imaging instruments such as SPHERE [J. Beuzit et al. (2008)], MagAO[Males et al. (2006)] and SCExAO[N. Jovanovic et al. (2015a)]. In these instruments, satellite spots are generated by adding a waffle pattern or sine waves on the DM. Both amplitude and phase modulation can be used for calibration. However a phase grid is easier to implement rather an amplitude grid for which we do not need additional hardware to be installed. With the phase grid we can make the satellite spots incoherent and this is not possible with an amplitude grid. A detailed description about the incoherent satellite spots is provided in the §2.5. This was the main reason why Subaru/SCExAO adopted the phase modulation. In the case of a static amplitude grid, one has to change the pupil plane mask physically each time if there is a need to change separation or intensity of satellite speckles, whereas a periodic phase grid provides flexibility both in terms controlling the position and the intensity. Each satellite speckle has its own phase and amplitude, and the interference between speckles is governed by addition of complex amplitude. Figure 2.3a shows the simulated image of the pupil from Subaru Telescope with sinusoidal phase modulation, and figure 2.3b represents the satellite speckles generated in the image plane. It should be noted here that the orientation of the phase modulation on the DM with respect to the telescope's spider were chosen to be perpendicular and horizontal with axis of the DM for the convenience. In principle, the relative orientation should not affect the accuracy of the photometry and astrometry. The telescope's spider introduces static speckles in the AO corrected images. When subtracting two consecutive frames, this would remove the static speckles. However, it is usually preferred not to place the satellite spot on top of the speckle halo formed due to the telescope's spider as these static speckles are not very well calibrated (i.e. phase, amplitude and separation w.r.t central PSF are not rigorously pre-determined) and thus the total intensity at the location of the satellite spot would depend both on the satellite spot and these static speckles.

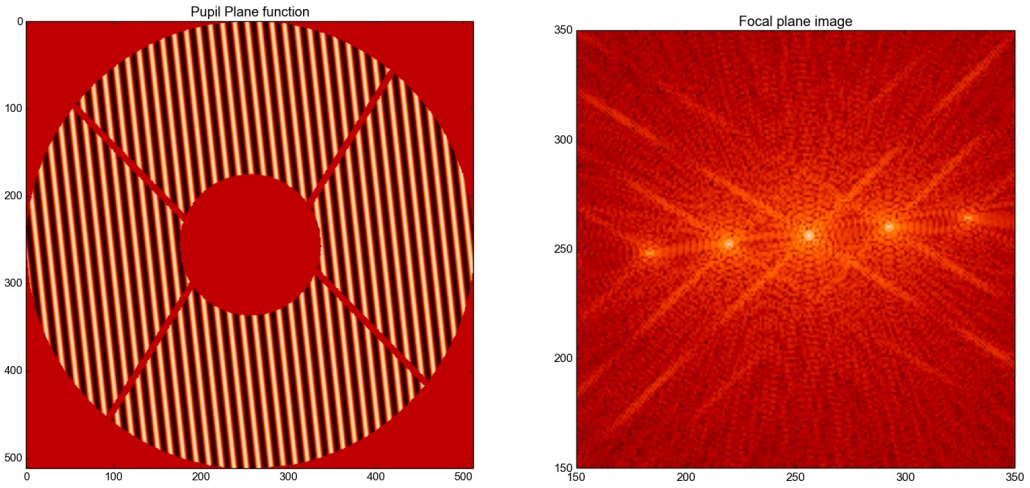

(a) Sinusoidal Phase Modulation **(b)** Corresponding focal plane image

Figure 2.3 Sinusoidal phase modulation in the pupil plane (a) generates satellite speckles in the focal plane (b).

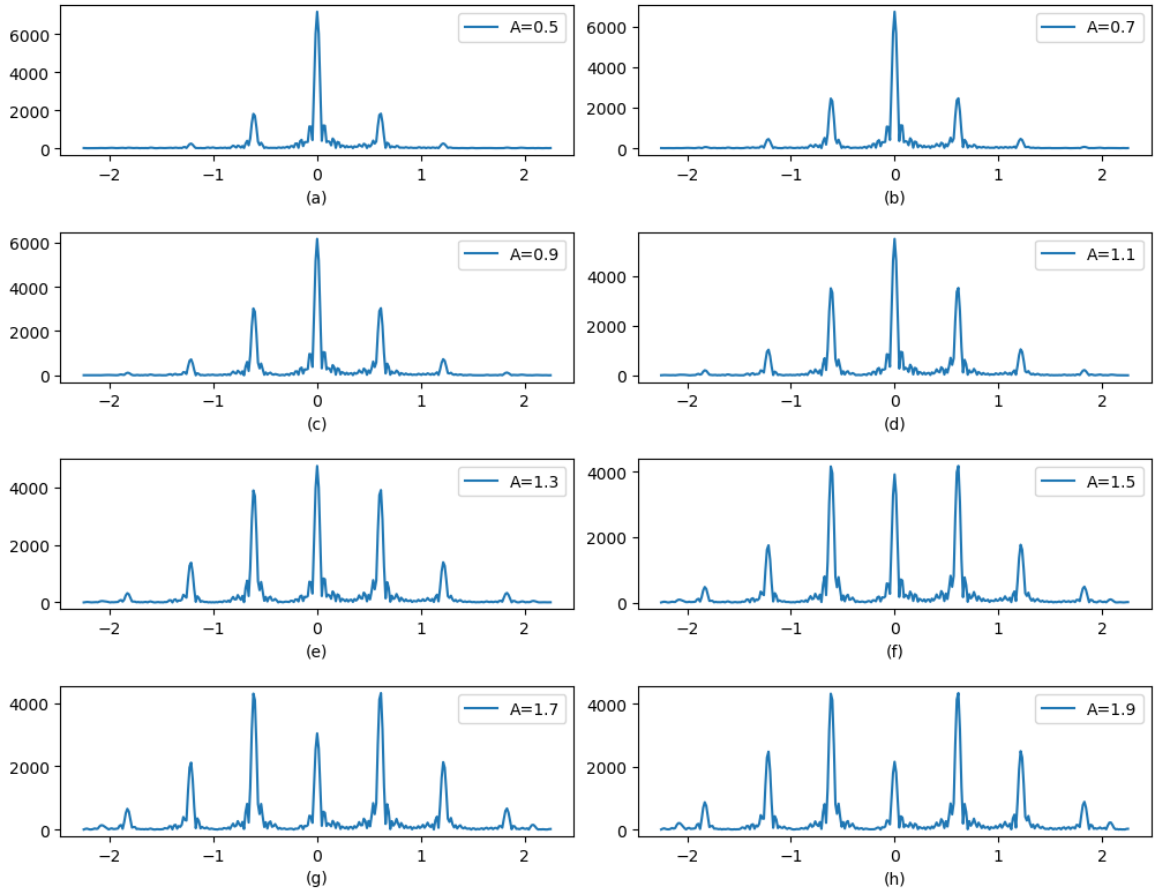

Figure 2.4 Variation of intensity of the satellite spot with different amplitudes (A) of sine-wave.

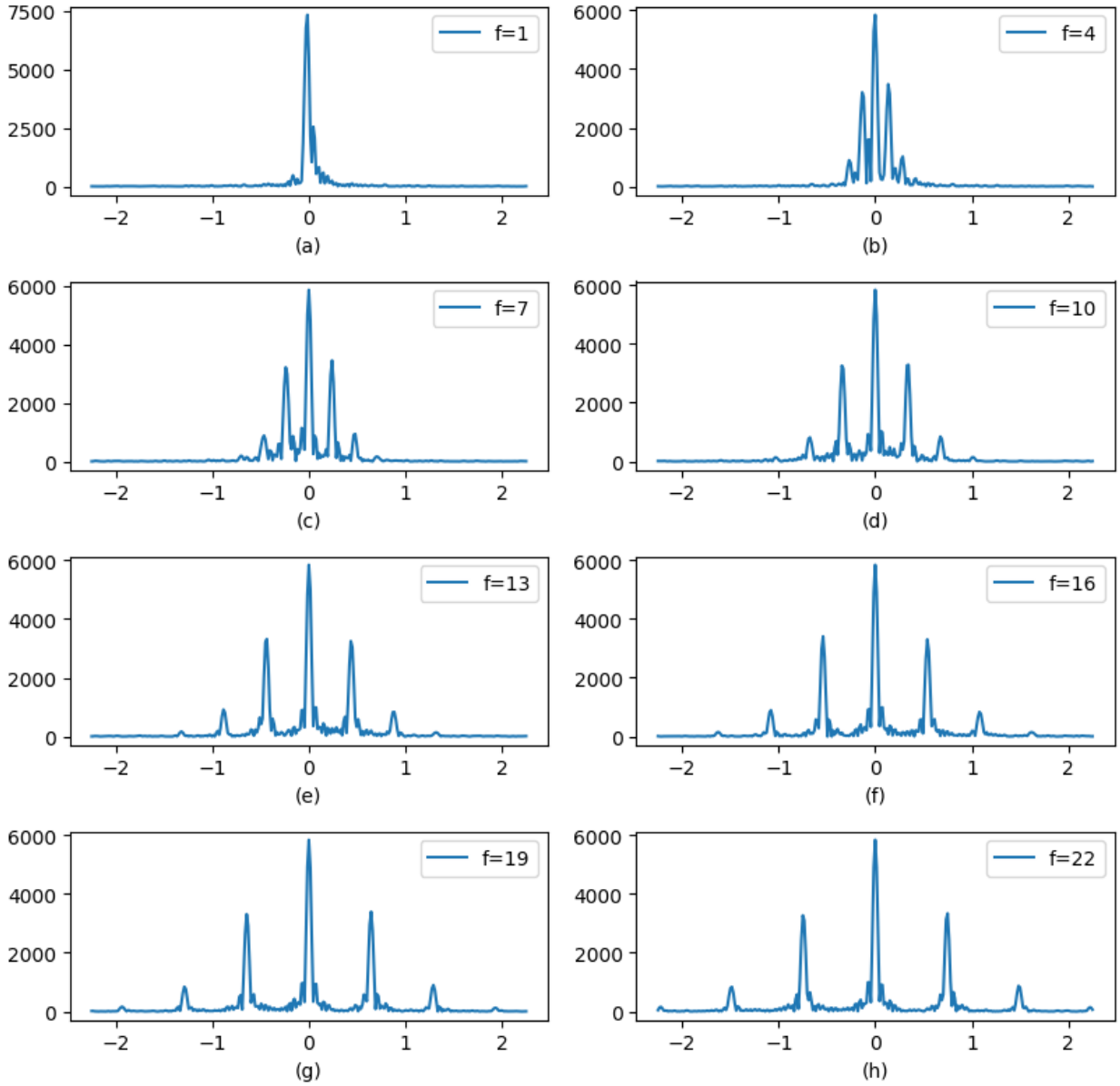

Figure 2.5 Variation of separation between spots with different frequencies (f) of sine-wave.

2.5 Creating Incoherent Satellite Speckle

The satellite speckles generated due to phase or amplitude modulation interfere with the underlying background speckle halo. This leads to distortion of satellite speckles and henceforth reduces the accuracy with which the PSF can be located and its brightness be determined. This can be understood through analytical equations of beam interference. Let A_h and ϕ be the amplitude and phase of the underlying background speckle halo respectively, and A_s and θ be the amplitude and phase of the satellite speckle. The total intensity I due to the interference between the background speckle halo and satellite speckle can computed as follows:

$$\begin{aligned} I &= |A_h e^{i\phi} + A_s e^{i\theta}|^2 \\ &= |A_h(cos\phi + isin\phi) + A_s(cos\theta + isin\theta)|^2 \\ &= |(A_h cos\phi + A_s cos\theta) + i(A_h sin\phi + A_s sin\theta)|^2 \\ &= (A_h cos\phi + A_s cos\theta)^2 + (A_h sin\phi + A_s sin\theta)^2 \\ &= A_h^2 cos^2\phi + A_s^2 cos_\theta^2 + 2A_h A_s cos\phi cos\theta + A_h^2 sin_\phi^2 + A_s^2 sin^2\theta + 2A_h A_s sin\theta sin\phi \\ &= A_h^2 + A_s^2 + 2A_h A_s(cos\phi cos\theta + sin\theta sin\phi) \\ &= A_s^2 + A_h^2 + 2A_h A_s cos(\phi - \theta) \end{aligned} \tag{2.12}$$

Equation 2.12 shows that the resultant intensity at the location of satellite spots is the sum of intensity of the satellite speckle A_s^2, intensity of the background speckle halo A_h^2 and the interference term $A_s^2 + 2A_h A_s cos(\phi - \theta)$ between them.

The presence of an additional underlying speckle halo (A_h) hinders precise calibration. Let these resultant speckles be named as "coherent" speckles as they interact with background speckle halo. To eliminate this issue (or interaction), one can make the satellite speckles brighter than the underlying speckle halo, i.e. $A_s \gg A_h$ and this case the second and third term of equation 2.12 can be neglected. However doing so will divert a significant amount of starlight from the PSF core and disrupt other background operations such as wave front sensing and short wavelength imaging. In the case of SCExAO instrument which used large sinusoidal modulation amplitude ($\sim$25 to 50nm), these spots lie well within the detector dynamic range of the near Infrared wavelength integral field spectrograph (CHARIS), however are too bright to be used by the visible instrument(VAMPIRES). Thus satellite brighter speckles may not always be the solution for precise calibration. N. Jovanovic et al. (2015b) have addressed this limitation by rapidly switching the phase of these speckles between

0 and π within an exposure to create temporarily "incoherent" speckles which do not interfere with the underlying background. Consider an image taken at time $t = 0$ with satellite spot having phase 0, and then subsequently another image is taken at time $t = \delta$ with satellite speckle having phase π. If the timescale between these two images is quite small than the timescale of variation of background speckle halo, then by co-adding these two images, we can eliminate the coherent background interference. This can be understood through following equations:

$$\begin{aligned} t = 0 : I_1 &= A_{s1}^2 + A_{h1}^2 + 2A_{h1}A_{s1}cos(\phi_1) \\ t = \delta : I_2 &= A_{s2}^2 + A_{h2}^2 + 2A_{h2}A_{s2}cos(\phi_2 - \pi) \\ &= A_{s2}^2 + A_{h2}^2 - 2A_{h2}A_{s2}cos(\phi_2) \end{aligned} \tag{2.13}$$

For a short timescale we can assume the background variation to be negligible i.e. $A_{h1}^2 = A_{h2}^2 := A_h^2$ and $\phi_1 = \phi_2$, further the phase grid parameters are chosen to be constant over this timescale, therefore $A_{s1}^2 = A_{s2}^2 := A_s^2$. If the images are averaged together, the coherent interference term cancels out:

$$\begin{aligned} I_{avg} &= (I_1 + I_2)/2 \\ &= (A_{s1}^2 + A_{h1}^2 + 2A_{h1}A_{s1}cos\phi_1 + A_{s2}^2 + A_{h2}^2 - 2A_{h2}A_{s2}cos\phi_2)/2 \\ &= A_s^2 + A_h^2 \end{aligned} \tag{2.14}$$

Thus by averaging frames closely spaced in time while modulating the phase of the artificial satellite speckles between 0 and π, it possible to get the resultant intensities depending only on amplitudes of the speckles interacting, and can be defined as "incoherent" speckles. Figure 2.6 represents a qualitative comparison of the incoherent satellite speckles with the coherent ones.

Figure 2.6 (a) and (b) represent the typical speckle halo with Airy rings, diffraction from the spiders and residual background speckles obtained from SCExAO instrument after post-AO correction with a pair of artificial satellite speckles of similar brightness. Figure 2.6 (a) has incoherent artificial speckle in it while Figure 2.6(b) has coherent ones. After subtracting a reference image from these two images, it can be clearly seen that incoherent artificial speckles represents true replicas of the actual PSF (Figure 2.6 (c)) rather than the coherent ones (Figure 2.6 (d)). In addition, incoherent speckles are more identical to one another as compared to the coherent ones. N. Jovanovic et al. (2015b) have demonstrated that there is a clear improvement of $\sim$ 2 to 3 times in photometric and astrometric measurement when incoherent satellite speckles are used instead of coherent ones.

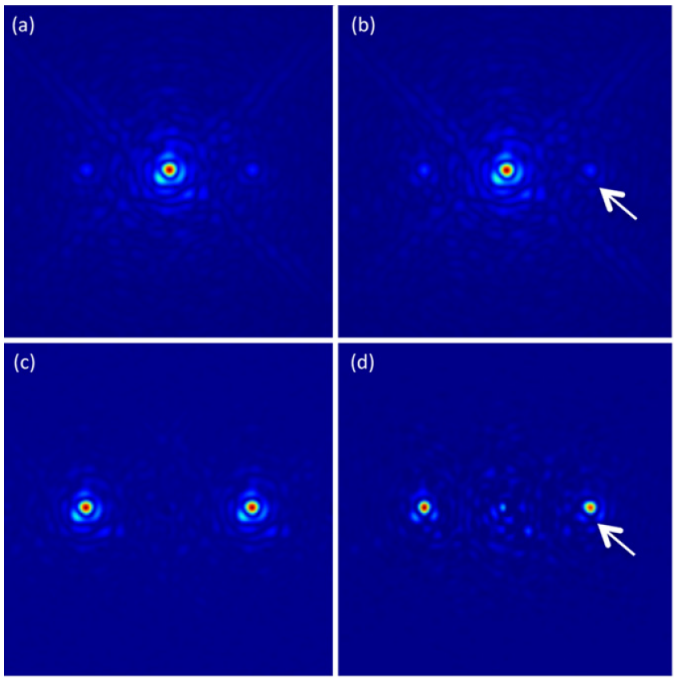

Figure 2.6 (Top) PSF with two artificial speckles at 10 λ/D from the PSF. (a) Incoherent speckles. (b) Coherent speckles. (Bottom) PSF-subtracted image (c) with incoherent speckles and (d) with coherent speckles. Picture Courtesy: N. Jovanovic et al. (2015b)

Modulating the phase of the pupil grid has been an ideal approach for improving precision. The measured intensity of incoherent satellite speckle is the total intensity due to the actual satellite speckle and the underlying speckle halo. The presence of this underlying speckle halo (i.e. A_h^2 in equation 2.14) will ultimately limit the photometric and astrometric precision. The effect of the underlying background halo will be significant in the case where satellite speckles are made fainter. As has been discussed earlier fainter satellite speckles are desirable. For they can be used to concurrent calibrations in two different wavelength regimes. The subsequent chapters deals with removing this incoherent background halo from the measurement.

2.6 Summary

In this chapter we discussed various approaches undertaken in the early days for precise photometric and astrometric calibrations. We started with discussing some of the issues related to locating the PSF position in coronagraphic images, such as using a lenslet array in the focal plane can be useful to track the PSF position via feedback loop. This method was however was inadequate to do precise photometry. Modulating the amplitude (or phase) in the pupil plane was used to create off-axis

copies of the central PSF, and then was named as artificial or satellite speckles. These were then used for simultaneous photometric and astrometric measurement. As discussed above, the presence of an underlying background speckle halo will interfere with these fiducial copies and can ultimately limit the accuracy. The subsequent chapters in my thesis deals with removing this underlying background halo, and arrive at a more precise photometric and astrometric measurement.

Chapter 3

Precision Photometry and Astrometry with Alternating Speckles

3.1 Introduction

Accurate astrometric and photometric calibrations of nearby faint companions in post coronagraphic images is difficult as the central starlight which is predominantly used to track the flux and position of the companion has been blocked by a coronagraph. As discussed in Chapter 2, off-axis symmetric copies of the central starlight defined as satellite spots (or artificial spots) are introduced in the focal plane to track the flux and position of the starlight as well as perform relative photometry and astrometry of the nearby companion. Several factors such as residual wave front corrections, atmospheric dispersion, chromatic aberrations distort these satellite spots, thus reducing the accuracy to which the central PSF can be located and the flux be determined. These aberrations induces static speckles (caused by geometry of the pupil and aberrations), quasi-static speckles (due to slowly varying instrument alignment or telescope pointing) or dynamic speckles (due to atmospheric dispersion, Strehl variation) in the image plane. These background speckles then interfere with the satellite speckles, produce some other spots which are not true replicas of the central PSF. The shape, position and flux of the resultant copies produced due to the interference will depend on the phase and amplitude of the underlying residual speckles. To make these satellite spots temporarily independent of the underlying background speckle halo, the phases are swapped in high speed ($\sim$kHz) and time-averaged within an exposure [N. Jovanovic et al. (2015b)]. A detailed explanation of this phase swapping technique has been discussed in chapter 2. The incoherent copies hence produced resembles more of the true replicas of the central PSF. However, there still remains a temporarily static background (refer to A_h^2 term in the equation 2.14) will ultimately limit our

flux measurement and position. This chapter deals with eliminating the static background (i.e. A_h^2). The approach as will be discussed in this chapter was developed by me during my PhD. In section 4.2, I discuss the effect of underlying static background on the relative flux measurement. In section 4.3, I introduce a new method named as the *Alternating Technique* to remove the underlying background speckles. In section 4.4, I conclude the chapter with a qualitative comparison of the alternating technique with the regular approach of estimating the underlying background and removing it from the measurement.

3.2 The underlying background halo

In this section, I discuss the effect of the static background on the total flux, relative flux measurement between companion and the central PSF and how removing this background would eliminate the effect of Strehl variation on measurement. To begin with, I discuss how the satellite spots are primarily used by astronomers to do photometric and astrometric measurements.

The relative flux measurement between the companion and the host is the goal of photometric calibration (i.e. F_p/F_s, where F_p is the companion flux and F_s is the flux of stellar host). In post-coronagraphic images, F_p/F_s is derived from measurement of F_p/F_{ss} where F_{ss} is the measured flux of one of the satellite speckles. The grid parameters can be adjusted to provide a given contrast between the host star and the satellite speckle, i.e. $F_{ss}/F_s = c$ where c is a constant quantity. In the case of an amplitude grid, the value of c depends on thickness, wire spacing of the grid and wavelength of incoming light [Marois, Lafreniere, Macintosh, et al. (2006), Sivaramakrishnan and Ben R. Oppenheimer (2006)]. Similarly in the case of sinusoidal phase modulation, the value of c is proportional to the amplitude of sine wave, and inversely proportional to the square of wavelength of the starlight (refer to §4.3 for detailed derivation). During an observation sequence the grid parameters of the amplitude mask or phase mask are kept to be constant. This ensures that the flux ratio of the satellite spots and the central PSF are kept as stable as possible during the observation sequence.Using the satellite speckles, F_p/F_s can be computed as:

$$\frac{F_p}{F_s} = \frac{F_p}{F_{ss}} \times \frac{F_{ss}}{F_s} \tag{3.1}$$

$$= \frac{F_p}{F_{ss}} \times c\ . \tag{3.2}$$

Using propagation of error theory (i.e. if $f = aA$, then error in f, $\sigma_f = |a|\sigma_A$, where a and

A is a constant and variable respectively), we conclude that the error in measurement of F_p/F_s is directly proportional to the error in F_p/F_{ss}. Equation 3.2 physically suggests that the error in the measurement of the relative flux between the companion to central starlight is directly dependent on the error in the measurement of relative flux between the calibrator source and the central starlight. Hence one needs to measure F_{ss} precisely and then F_s can be directly computed by scaling F_{ss}. As discussed in chapter 2, incoherent artificial satellite spots is currently the preferred mode calibration during a coronagraphic observation sequence. However while using the incoherent satellite spot, astronomers count the total flux of the actual incoherent speckle plus the underlying static background in an image (refer to equation (2.14), where the flux at the location of the speckle grid, ($I_{avg} = A_s^2 + A_h^2$). Therefore, without the loss of generality, we consider the measured flux of the satellite speckle (or companion) is the sum of the flux from the actual speckle (or companion) and the incoherent background level and can be expressed as follows:

$$\tilde{F_{ss}} = SR \times F_{ss} + F_{bg} \tag{3.3}$$

$$\tilde{F_p} = SR \times F_p + F'_{bg}, \tag{3.4}$$

where $\tilde{F_{ss}}$ and $\tilde{F_p}$ are the measured satellite speckle and companion flux respectively, F_{ss} and F_p are the actual satellite speckle and companion flux, F_{bg} and F'_{bg} are the incoherent background levels at the locations of the satellite speckle and companion respectively and SR is the Strehl ratio. In high contrast imaging instruments, we use a narrow field of view ($\sim$2 arcsecond), the SR value is kept to be constant. In equation (3.3) and (3.4) we have considered incoherent speckles instead of a static amplitude or phase grid which renders coherent speckles, using the latter will additionally introduce a coherent mixing term (i.e. $A_s^2 + A_h^2 + 2A_hA_scos(\phi - \theta)$ term in to equation (2.12)). For slowly varying quasi-static speckles, we can eliminate F_{bg} or F'_{bg} by subtracting a frame from an adjacent frame in time where the satellite speckle and companion are absent at the position where they used to be in the previous frame. This leads to the following revised equations:

$$\tilde{F_{ss}} \approx SR \times F_{ss} \tag{3.5}$$

$$\tilde{F_p} \approx SR \times F_p\ . \tag{3.6}$$

The presence of incoherent background affects the relative flux measurement as evidenced from equation (3.3) and (3.4). Just taking the ratio of $\tilde{F_{ss}}$ and $\tilde{F_p}$ will not give us true relative photometry.

Moreover, taking average value from large number of measurement will not converge to the true flux ratio, as the we consider SR and F_{bg} will add to the correlated noise. Therefore, we need to remove the background more accurately so that our measurement is limited by uncorrelated noise (or random noise) instead of correlated noise. Doing so will ensure us that with more number of measurements, we are arrive at the actual flux ratio between the companion and the central star. This is crucial to study the dynamic evolution, characterization of the companion.

3.3 The Alternating Speckle Technique

Our approach to remove the static background from the relative flux measurement is to spatially modulate the speckle pattern and put them at location different from the previous frame for each exposure. With this approach, we can directly measure the underlying background F_{bg} speckle at the location where there was incoherent speckle in the previous frame (or will be in the next adjacent frame). The directly measured F_{bg} can then be subtracted from the satellite spot's flux. We used spatial switching (or toggling) of the incoherent speckle pattern so as not to loose calibration spots in each frame. We name this technique as the *Alternating Technique* as the incoherent phase grid geometry toggles for each frame. F'_{bg} can be precisely estimated by using dedicated advanced post-processing techniques such as Spectral Differential Imaging (SDI) or Angular Differential Imaging (ADI), which are introduced in chapter 1. The effect of Strehl on the measured fluxes can be eliminated by dividing the two measurements as shown below.

$$\frac{\tilde{F}_p}{\tilde{F}_{ss}} = \frac{F_p}{F_{ss}} = \frac{1}{c} \times \frac{F_p}{F_s} \tag{3.7}$$

In order to implement our alternating scheme, we used two orthogonal sinusoidal phase grid. The phase of each of the sine waves were swapped between 0 and π at high speed within an exposure. For each exposure, we use one direction of the sine wave at a time, and then change the direction for the next exposure. Figure 3.1 depicts a schematic representation of our technique. Figure 3.1 (a) and (b) represents the Subaru Telescope Pupil plane function with sinusoidal phase modulation in two different directions for two consecutive frames. Figure 3.1 (c) and (d) represents the corresponding focal plane image. By alternating the direction of sine-wave, incoherent satellite spots are made to be located at place different than before. Azimuthal rotation of the phase modulation about

the optical axis rotates the spots in the image plane. The 1-D sinusoidal phase map shown in Figure 3.1 can be used to generate a single pair of speckles (we do not consider here higher order fainter spots). In our scheme, we keep the amplitude of the sine waves identical and only change the orientation. This ensures that the intensity of the corresponding satellite spots are kept same for each frame. The Alternating switching works well for any location of the satellite spot in the frame. Ideally, they should not be placed at a location very similar to that of the previous frame. Subtracting two frames with nearly two similar spatial patterns might double subtract a part of the Airy intensity profile, and the spots may not be well resolved for further calibration. For simplicity, I used two orthogonal phase map for the DM that already existed for regular science observation to demonstrate my technique. An additional benefit would be that in a subtracted image, we get four spots (2 spots with positive flux and other 2 spots with negative flux). The point of intersection of the lines joining each of the pairs (having same sign) reveals the position of the central PSF. This extra information can be used to monitor more precisely the drift of the central PSF.

One more similar approach is to use one direction of the sine-wave, and then turn "off" the grid pattern for the next exposure. With this approach, we loose calibration spots in the 50% of data frames during an observation sequence. Therefore, by using two different speckle patterns, generated by a single distinct sinusoid each, and alternating them between adjacent frames it is possible to produce all the data needed to remove the effect of the background and SR and achieve a precise relative photometry and astrometry, while maintaining calibration speckles in every science frame.

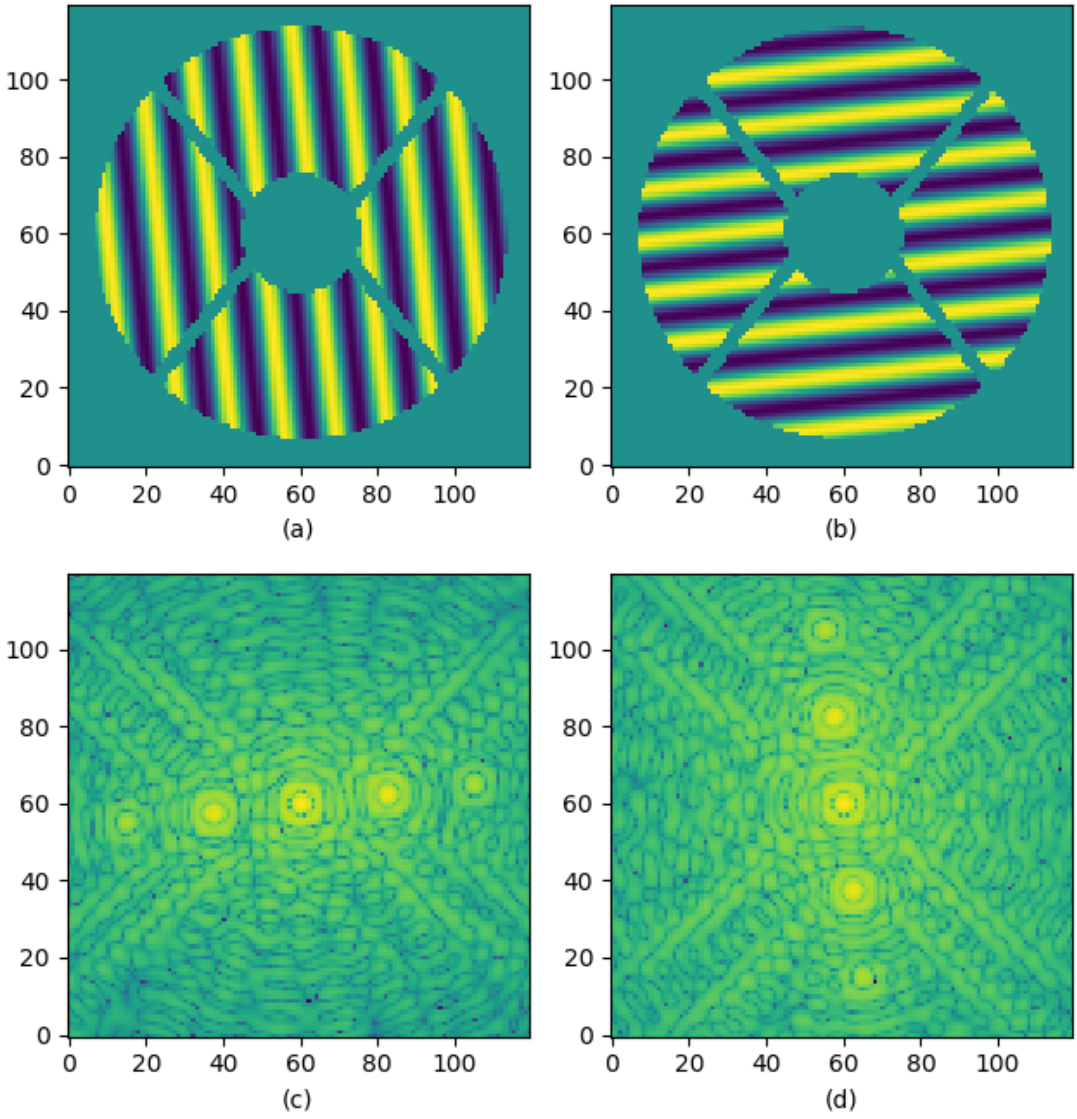

Figure 3.1 (a) and (b) represents simulated pupil image obtained from the Subaru Telescope with two different orthogonal sinusoidal phase modulation. Figure (c) and (d) represents the corresponding focal plane images with artificial incoherent satellite spots.

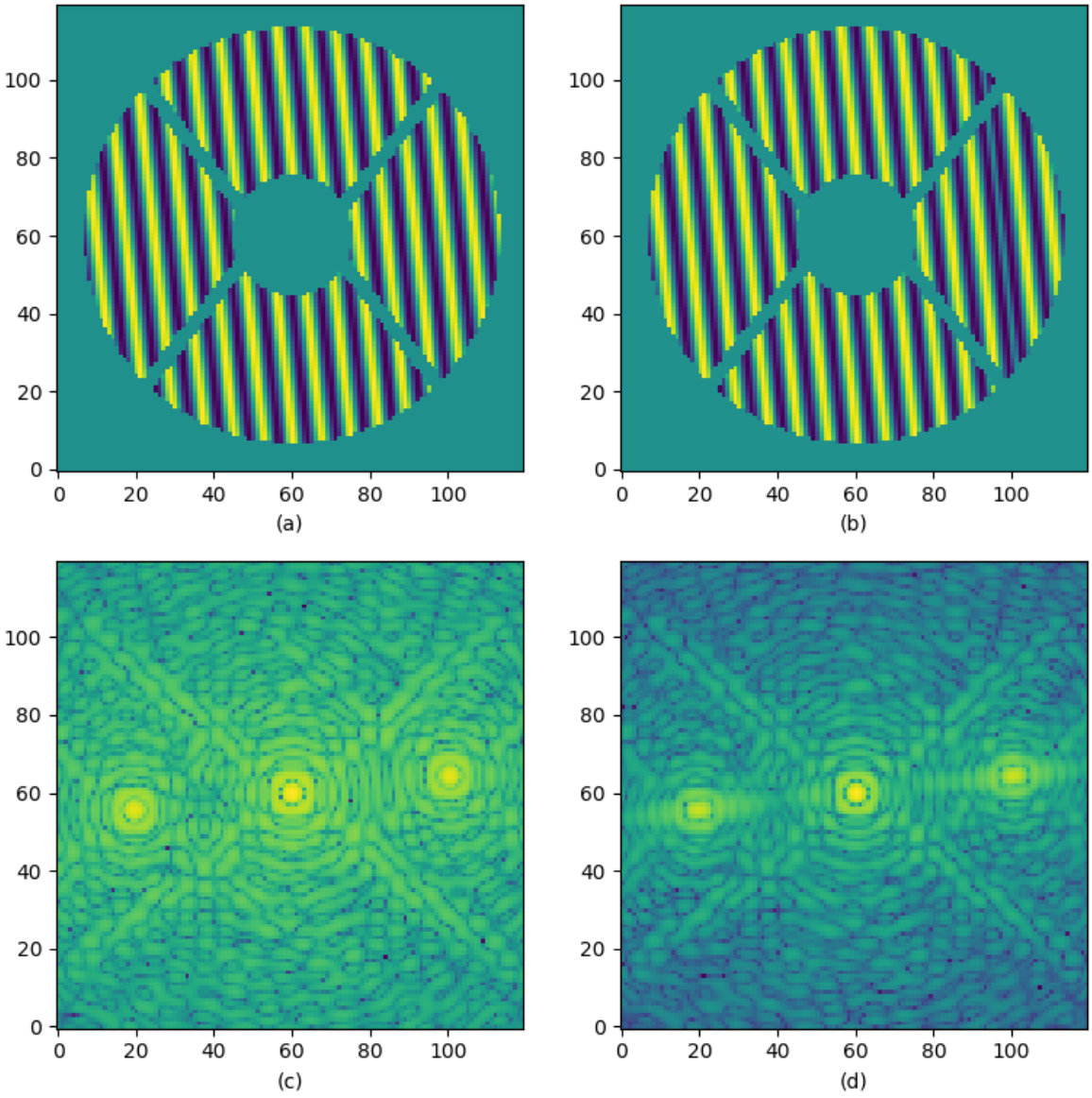

Figure 3.2 Image (a) and (b) represent simulated pupil obtained of the Subaru Telescope with vertical sinusoidal phase modulation. Figure (c) and (d) are the corresponding focal plane images. In image (c) the satellite spots are perfectly symmetrical because of the uniform sine wave across the pupil, where as in (b) there are two sine-waves with opposite phases (note the phase changes at the right edges of figure (b). Due to this phase shift, the satellite spots are elongated as in (c). This situation may occur when the command to the DM is not perfectly synchronized, and a given instance the DM sees combination of two sine-wave with different phases.

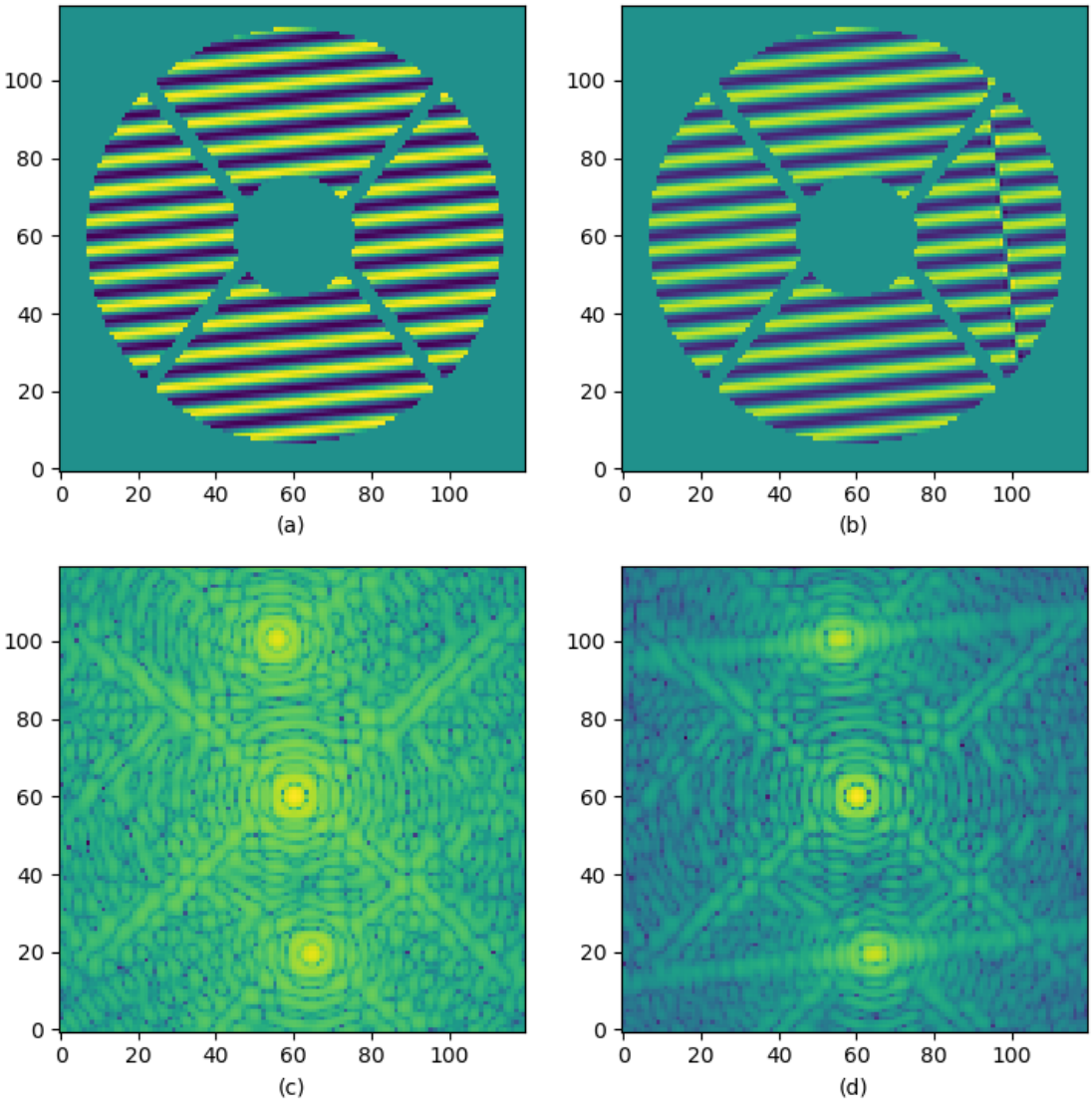

Figure 3.3 Image (a) and (b) represent simulated pupil obtained of the Subaru Telescope with horizontal sinusoidal phase modulation. Figure (c) and (d) are the corresponding focal plane images. Using Similar arguments as in Figure 3.2, the satellite spots are elongated along the same direction to non-uniform phase across the pupil.

3.4 Summary

In this chapter we discussed the effect of the underlying incoherent speckle halo on relative photometric measurements. The resultant flux of the calibrator spot includes the underlying background. Often astronomers assume this background to be equal to the average flux count in an annulus surrounding the satellite spot. However, due to imperfect AO corrections, or with varying atmospheric condition, this assumption is not true. The background speckles will vary in time. Average flux count in annulus is highly dependent on the selected annulus region. Therefore, estimating the background from the annulus is not an accurate way of measuring the relative flux. This will be quantitatively demonstrated in the upcoming chapters. The *Alternating Technique* introduced in this chapter is a robust way to dynamically determine the static background during an observation sequence. Here we considered the simplest case (i.e. use one only direction of the sine-wave at a time) to demonstrate the alternating scheme and generate at least a pair of incoherent satellite speckles. Using more than one direction will further improve the precision by a factor of $\sqrt{n}$, where n is the number of sine-waves used. However, more satellite spots in the image plane means more light is diffracted away from the central PSF core. This might affect the efficiency of the extreme AO corrections which operates in conjunction with phase modulation scheme. In the next chapter, I will be discussing the practical implementation of the *Alternating Technique* in the SCExAO instrument.

Chapter 4

Implementation of Alternating Scheme On SCExAO Instrument

In this chapter, I discuss in detail the implementation of the *Alternating Technique* on the SCExAO instrument.§4.1 starts with a brief discussion about the Subaru Telescope where the SCExAO instrument is currently operated. We temporarily and spatially modulated the pupil plane deformable mirror (DM) of the SCExAO instrument to generate incoherent satellite speckles with oscillating spatial patterns. I used the integral field spectrograph CHARIS and the near infrared fast frame-rate C-RED2 camera for data acquisition. The phase modulation command to the DM is synchronized with the camera's data acquisition as is required to achieve alternating incoherent speckles. For relatively fainter satellite spots (contrast of the order of $\sim 10^{-3}$), the absolute flux ratio (c) was computed using a classical set of "ladder" frames using the laboratory laser source.

4.1 The Subaru Telescope

The Subaru Telescope operated by the National Astronomical Observatory of Japan (NAOJ), National Institutes of Natural Sciences (NINS) is currently one of the world's largest optical telescope with a primary mirror of diameter 8.2m. The telescope is situated at an altitude of 4139m on the summit of Maunakea, Hawaii (see Figure 4.1a),at a latitude of $19^0 49' 32.16" N$ thus can scan the sky from the North Star to the Southern cross. The telescope, built on the concept of Ritchey-Chrétien Telescope design has four foci: Prime focus ($f/2.0$), Cassegrain focus ($f/12.2$), Nasmyth optical focus ($f/12.6$) and Nasmyth infrared focus ($f/13.6$). The Prime focus is optimized for wide field observations (diameter of FOV = 1.5deg) whereas the Cassegrain focus is used to observe a relatively narrow field (diameter of FOV = 0.1deg) with a long focal length. The Nasmyth foci host

several facility as well as visiting instruments (refer to figure 4.1b). Following is a list of the current facility and visiting instrument installed in the telescope.

Facility Instruments

- **AO188** The 188-elements Adaptive Optics system installed at the Nasmyth IR is the primary AO system at the Subaru Telescope and covers of 2.7′ FOV. It comprises of a 188-element bimorph deformable mirror, high-order curvature wavefront sensor with 188 photon counting Avalanche Photo Diodes (APD)s and a low order SHwFS with 16 APDs. It operates both in Natural Guide Star (NGS) and Laser Guide Star modes (LGS). Under normal seeing condition (0.6") it achieves a SR of $\sim 30-40\%$ in H-band [Hayano, Takami, Oya, et al. (2010), Minowa et al. (2010)].
- **COMICS** The Cooled Mid-Infrared Camera and Spectrograph installed at the Cassegrain focus is used for wide field imaging (FOV 42" × 32") and spectroscopy (R ∼250-8500) [Kataza et al. (2000), Okamoto et al. (2003)]. The main purpose of this instrument is to study the structure and evolution of planet forming disks.
- **FOCAS** The Faint Object Camera And Spectrograph is also installed at the Cassegrain focus of the telescope. The instrument is used for imaging (FOV 6′ × 6′), multi slit spectroscopy and polarimetry in the optical band (0.4-1.0μm). Its main objective is to acquire spectra of distant galaxies, supernovae, quasars etc [Kashikawa et al. (2000)].
- **HDS** The High Dispersion Spectrograph is situated on the Nasmyth Optical platform of the telescope. It provides high resolution spectra (R∼100,000) in the visible band of stars which can used to study their atmosphere, chemical composition and detect exoplanets via Doppler shift in the spectrum [Noguchi et al. (2002), Bun'ei Sato et al. (2002)].
- **HSC** The Hyper Suprime-Cam instrument is installed at the Prime focus of the telescope and covers wide FOV ($1.5^0 \times 1.5^0$) with 87 million pixels and each having a spatial resolution of 0.17arcsec per pixel sampling. The instrument is used to conduct surveys and study dark matter distribution in optical band [Miyazaki et al. (2018)].
- **IRCS** The Infrared Camera and Spectrograph is installed on the Nasmyth IR Platform of the telescope. It is used in combination with AO188 to provide diffraction limited images (FOV 20"-54") in near IR band and as well as conduct long slit spectroscopy (R

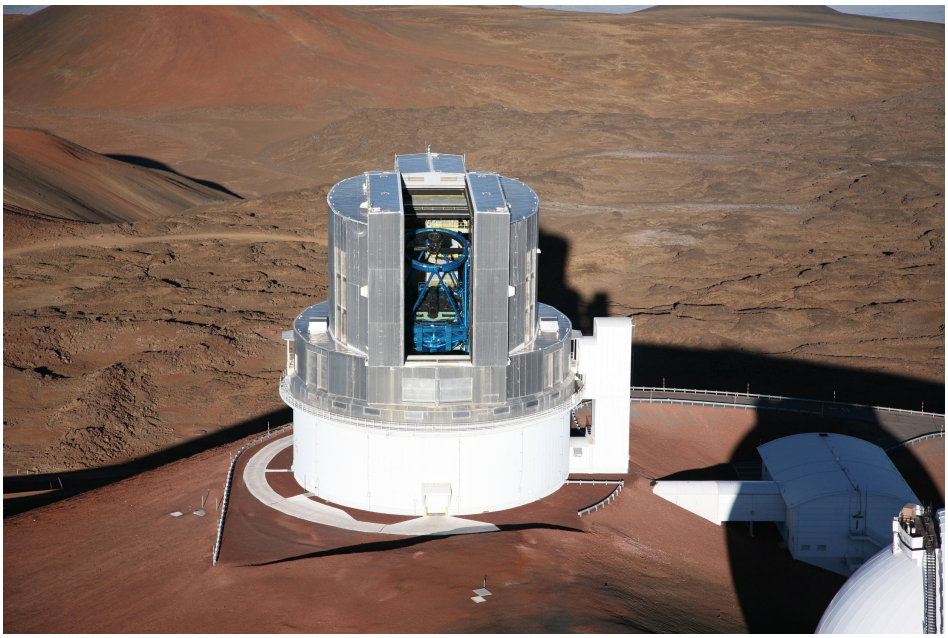

(a)

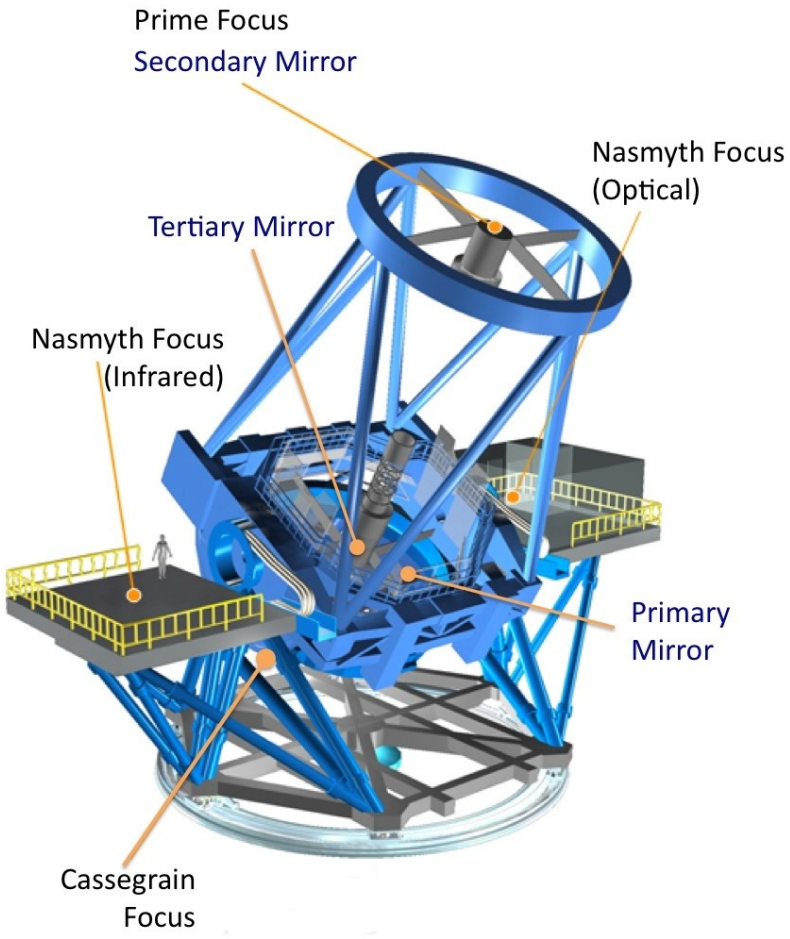

(b)

Figure 4.1 (a)The Subaru Telescope located on the Maunakea, Hawaii (b) Conceptual diagram of the telescope's architecture with the four focii. SCExAO instrument is located on the Nasmyth IR focus. Picture Courtesy: https://subarutelescope.org/en/, META Corporation, Japan.

$\sim 100 - 20,000$) of distant galaxies, brown dwarfs, star forming regions etc [Kobayashi et al. (2000), Tokunaga et al. (1998)].

– **MOIRCS** The Multi-Object Infrared Camera and Spectrograph instrument is used at the Cassegrain focus of the telescope for conducting out multi-object spectroscopy (R ∼500-3000) and wide-field imaging in the near IR wavelength band. The total FOV is 4'×7' with a spatial resolution of 0.116". The instrument is primarily used for characterization of numerous distant galaxies, large celestial structures nebulae [Ichikawa et al. (2006), Suzuki et al. (2008)].

Visiting Instruments

– **IRD** The Infrared Doppler instrument is fiber fed echelle spectrograph with a maximum spectral resolution of 70,000 in the near infrared wavelength region (0.97-1.75 microns). The instrument is located in the Coude room of the Subaru Telescope and recieves AO corrected light from the AO188 instrument. It is capable of measuring radial velocity of the star to a precision of 2m/s [Tamura et al. (2012), Takayuki Kotani, Motohide Tamura, Hiroshi Suto, et al. (2014), Takayuki Kotani, Motohide Tamura, Jun Nishikawa, et al. (2018)].

– **SCExAO** The Subaru Coronagraphic Extreme Adaptive Optics is the high contrast imaging instrument optimized for direct detection of faint companions and disks around nearby stars. §4.2 gives a detailed hardware architecture of the instrument and the science modules taking AO corrected light from it.

For my PhD work, I used the SCExAO instrument which receives partially low-order AO corrected light from the AO188 instrument. As will be discussed later, I used the integral field spectrograph CHARIS, and the high frame-rate low noise infrared camera C-RED2 for the final image acquisition and validation of my technique.

4.2 SCExAO Test-Bed

The Subaru Coronagraphic Extreme Adaptive Optics [SCExAO; N. Jovanovic et al. (2015a)] is a high-contrast imaging instrument dedicated to high angular resolution and direct imaging of

exoplanets, circumstellar disk around nearby stars. Currently it is commissioned at the Nasmyth platform of the Subaru Telescope. SCExAO performs fine wave front corrections and calibrations up to 1000 modes on the partially AO corrected light from the facility Adaptive Optics system[AO188; Minowa et al. (2010), Hayano, Takami, Olivier Guyon, et al. (2008)]. SCExAO comprises of a pyramid based high order wave front sensor (PyWFS) to measure high order modes and a Lyot based low order wave front sensor to identify low order modes such as tip-tilt, coma, defocus, astigmatism etc. The wave front correction is performed by a MEM technology based 2000-actuator DM running at up to 3.5kHz. The current system achieves 80-90% SR in H-band [Sahoo et al. (2018)]. A picture of the DM with its specification is provided in the Figure 4.4.

Figure 4.2 The SCExAO instrument with its science modules: CHARIS (the red box in the right), MEC (the silver tower in the left end), Visible bench on the top. Picture Courtesy: https://www.naoj.org/Projects/SCEXAO/

4.2.1 System architecture

Figure 4.3 depicts the optical layout of the SCExAO instrument. It primarily comprises of two optical benches; the near-Infrared (NIR) bench and the visible (VIS) bench placed on top of the NIR bench. The calibration bench hosts several light sources such as super continuum laser source, 1.53μm HeNe Laser, Halogen lamp etc which are used to conduct laboratory testings and calibra-

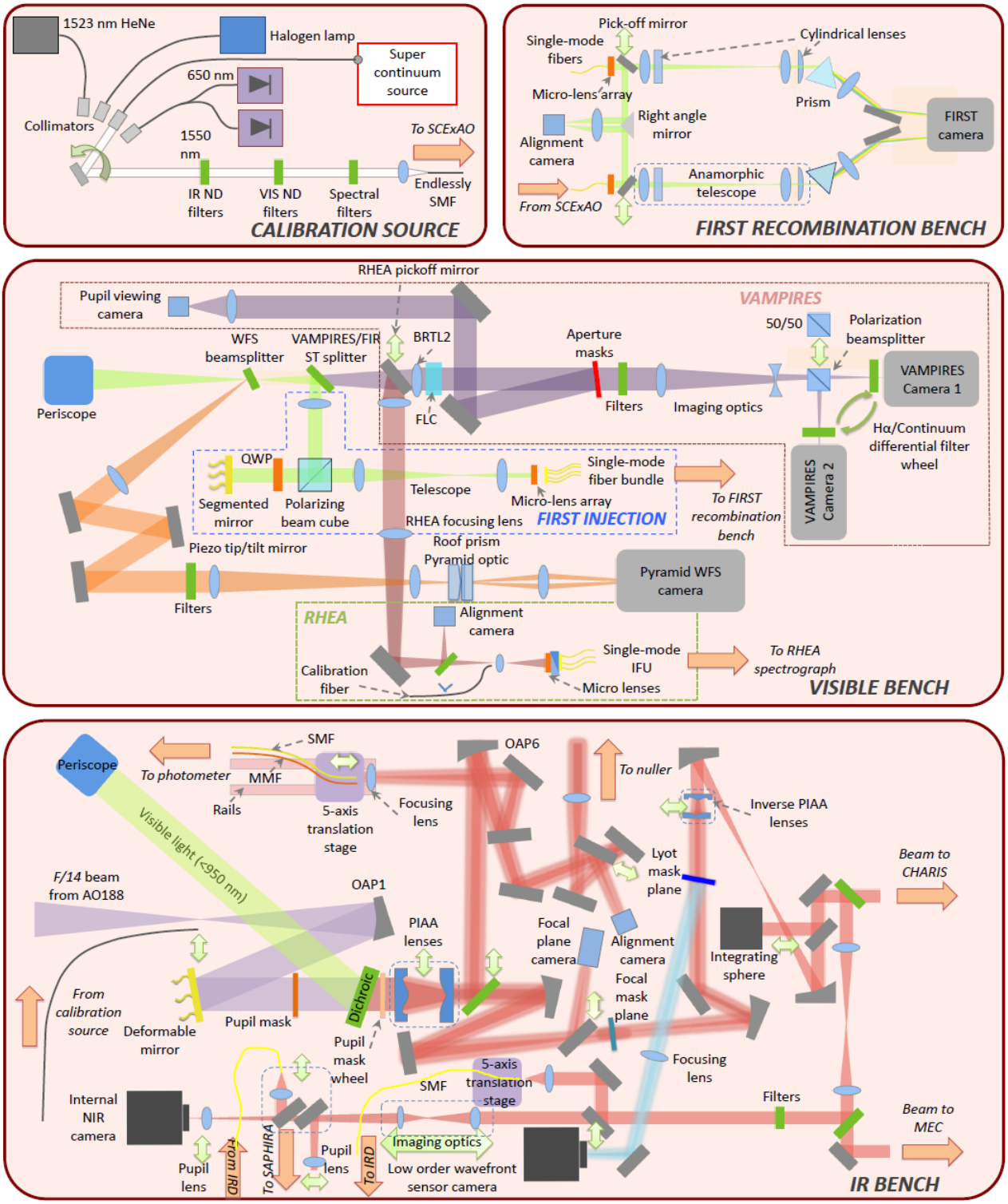

Figure 4.3 Optical layout of the SCExAO instrument commissioned at the Subaru Telescope. Picture Courtesy of Julien Lozi, Nemanja Jovanovic

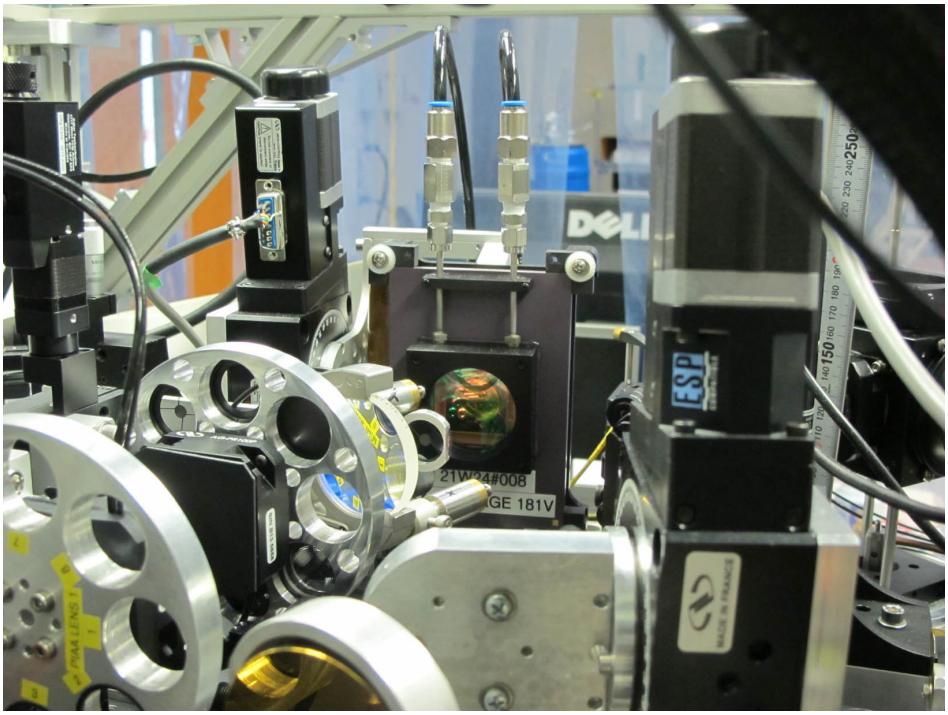

(a)

DM Specifications	
Parameters	Values
Actuator Count	2040 (50 across the active aperture)
Stroke	1.5μm
Aperture	19.6mm
Pitch	400μm
Mechanical Response	<75μs
Inter-actuator Coupling	15%

(b)

Figure 4.4 (a)A picture of the MEMs technology based deformable mirror manufactured by Boston Micromachines Corporation used in the SCExAO instrument, (b) Specifications of the deformable mirror.

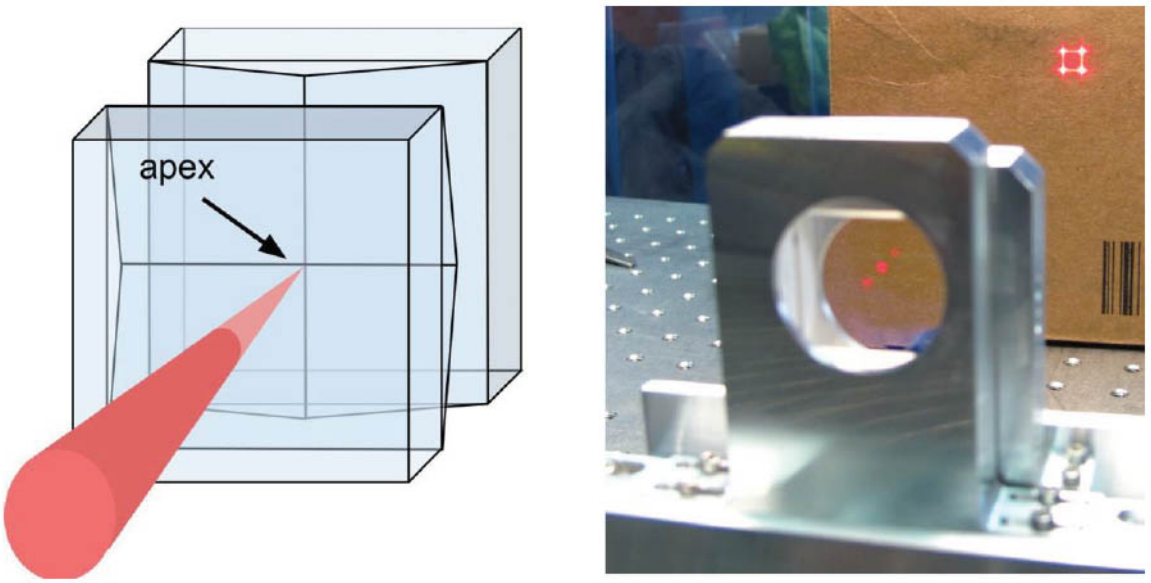

Figure 4.5 Image of the Pyramid Wavefront Sensor Used in the SCExAO.

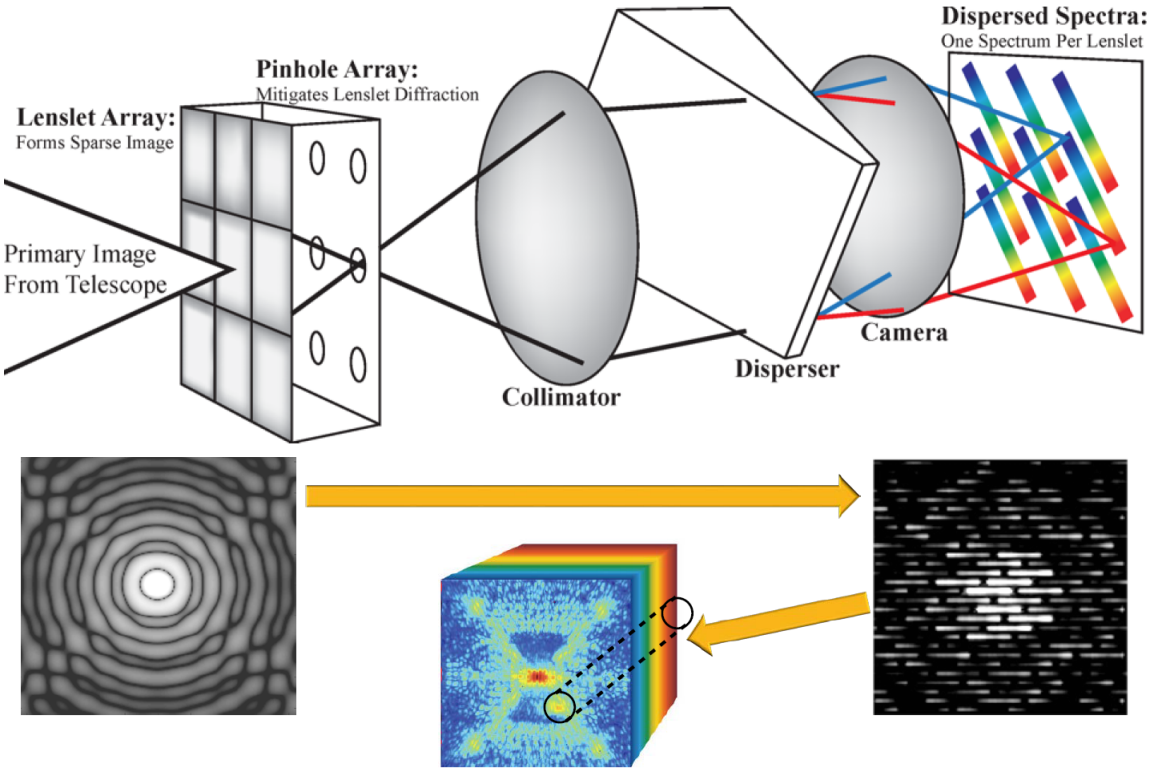

Figure 4.6 Conceptual Diagram of the CHARIS instrument. Picture Courtesy: Tyler Groff

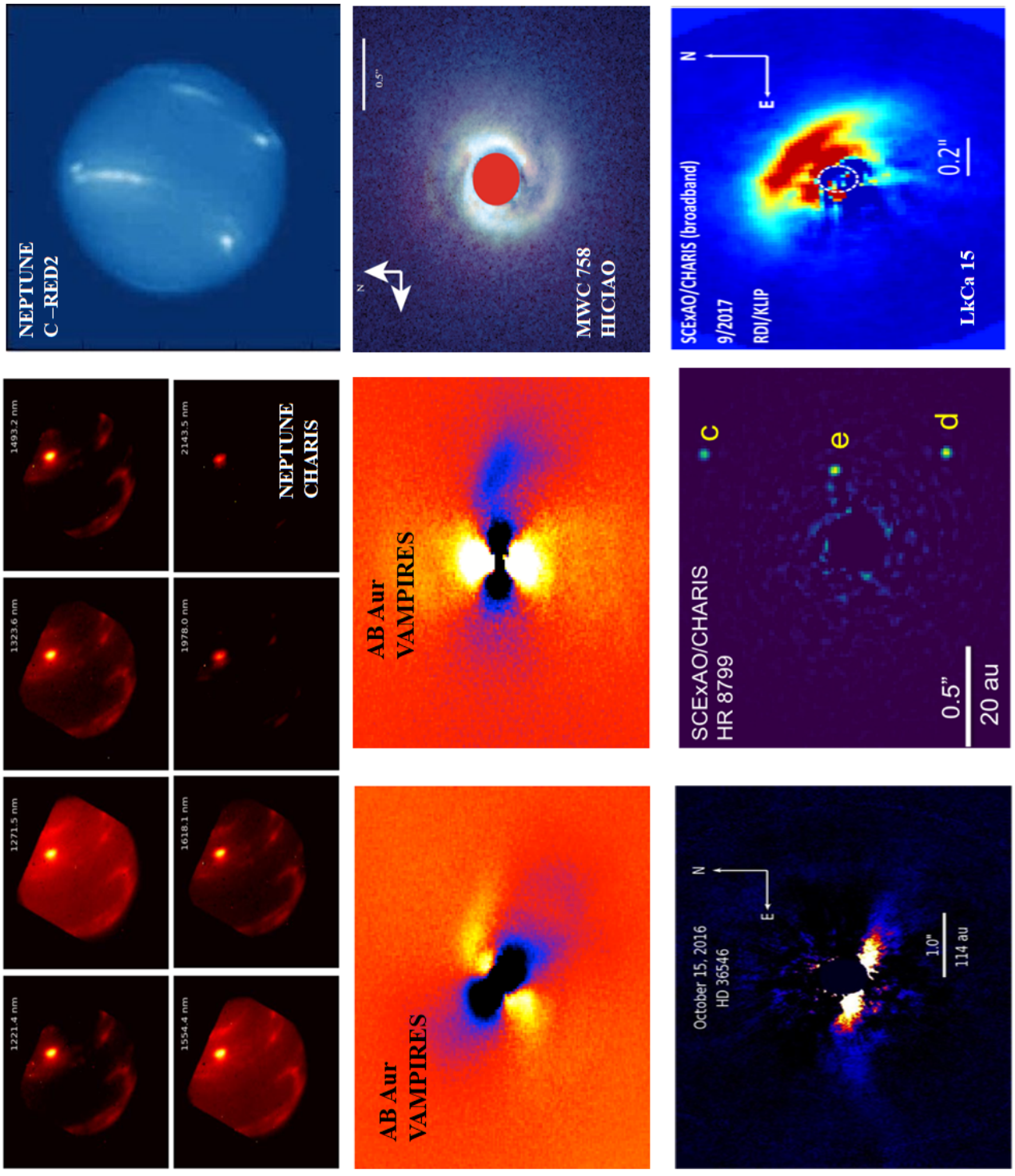

Figure 4.7 Images of exoplanets and circumstellar disk observed with SCExAO. Picture Courtesy: Thayne Currie, Tyler Groff, Barnaby Norris, Carol A. Grady, Timothy Brandt, Julien Lozi

tions. The IR bench contains 2000 actuator MEMS technology based Deformable Mirror (DM) manufactured by Boston Micromachines Corporation. The NIR bench receives the incoming light from AO188, and this beam is collimated by an off-axis parabolic (OAP) mirror to form a pupil image on the DM. The reflected beam from the DM is incident on a pupil plane mask and subsequently on a dichroic. The pupil plane mask replicates the spiders of the Subaru Telescope and is used for both on-sky and off-sky observation. The dichroic splits the incident light into two wavelength regimes. The dichroic reflects the visible light (< 940 nm) to the VIS bench through a periscope. The infrared light (> 940 nm) is transmitted through and is further used for coronagraphy, low order wave front sensing, imaging by the science instruments CHARIS. A variety of coronagraphic focal plane masks housed in a wheel is situated in this path of the transmitted light from the dichroic. These focal plane masks are used to suppress the on-axis starlight. Then the light travels through subsequent imaging optics and is finally intercepted by the science beam splitter to direct it towards CHARIS, Internal NIR camera (C-RED 2). The light directed to the C-RED2 camera passes through band pass and optical density filter wheel for spectral and flux selectivity respectively. The visible light reflected from the dichroic is directed towards the PyWFS mounted on the VIS bench for high order wave front corrections. Note that from Figure 4.3 we see that incident light do not fall perpendicular to the surface of the DM. The angle of incident of the incoming beam on the deformable mirror is nearly 11 degrees. Thus, the projection of the incoming beam on the surface is an oval shape rather than a perfect circular shape. This projection induces slightly larger separation between the horizontal spots than the vertical satellite spots. As will be further discussed, I monitored the stability of the relative flux and separation between spots. Therefore this static incident angle does not affect my calibration technique. Several modules which are attached to the SCExAO's NIR and VIS bench are listed below.

- **CHARIS** The Coronagraphic High Angular Resolution Imaging Spectrograph [CHARIS; T. Groff et al. (2017)] is an integral field spectrograph capable of providing simultaneous direct direct images and spectra of stellar targets in near infrared wavelength regime (1154 nm to 2387 nm) over a small field of view (2.07"×2.07"). The low and high spectral resolution (R) are ∼19 and ∼70 respectively.

- **REACH** Rigorous Exoplanetary Atmosphere Characterization with High dispersion coronog-

raphy[REACH; Takayuki Kotani, Motohide Tamura, Jun Nishikawa, et al. (2018), Julien Lozi et al. (2018)] is the new module at the Subaru Telescope and is now available to the community for scientific observation. This module takes extreme AO corrected light from the SCExAO instrument and injects it to a infrared doppler (IRD) radial velocity instrument. This module comprises of a single mode multi-core fiber, and this fiber bundle can be placed anywhere within the 2"×2" high contrast field of view. The aim of this module to provide high resolution spectra (R∼100,000) of exoplanets or circumstellar disk.

- **VAMPIRES** The Visible Aperture Masking Polarimetric Interferometer for Resolving Exoplanetary Signatures [VAMPIRES; B. Norris et al. (2015), B. R. Norris et al. (2012)] instrument offers diffraction limited visible images circumstellar disk, also simultaneous polarized images of the circumstellar environment. It is based on differential polarimetry and non redundant aperture masking technique.

- **FIRST** The Fibered Imager foR a Single Telescope [FIRST; Elsa Huby et al. (2012), Vievard et al. (2019)] instrument relies on the pupil remapping technique using single mode fibers for spatial filtering of wave front technique is optimized to provide high angular resolution image,spectra of surface of stars, and discover any nearby close companion in the visible band (600-850 nm).

- **MEC** MKID Exoplanet Camera [MEC; Day et al. (2003), Walter et al. (2018), B. Mazin (2014)] is a ultra fast camera with temporal resolution ∼2 microseconds. It is optimized to count the number of photons, their arrival timing on the detector and the wavelength of incident photons.

4.2.2 Software Architecture

The software to implement the switching pattern, command to the DM is written in Bash script and C++. The script to temporarily modulate the phase of the grid is also integrated into a Graphical User Interface (GUI) for the ease of operation. The command to change the orientation of the sine-wave is synchronized with the CHARIS data acquisition. This synchronization command uses a data-log file generated by CHARIS instrument. This data-log file is dynamically updated

Table 4.1 Current Satellite Spot Parameters

Satellite Spot Configuration	
Features	Suggested Options
Separation (from the central PSF)	22.5λ/D (max), 15.9λ/D, 11.2λ/D, 10.6λ/D, 7.5λ/D, 5.3λ/D
Brightness (w.r.t to central PSF)	10^{-4} - 10^{-2}
Number of Spots	2 or 4
Spot Modulation	Temporal Modulation - Phase of the spot is modulated between 0 & π in an exposure
	Spatial Modulation - Spatial position of the spot is changed between exposures
Coronagraph	Lyot, Vortex

Table 4.2 CHARIS Basic Instrument Parameter

FOV	2.07" × 2.07"
Detector	Hawaii 2RG
Wavelength Coverage	1154 nm to 2387 nmm
Coronagraph modes	Lyot, vAPP, PIAACMC, Vortex
Plate Scale	16.2 mas/lenslet
Satellite Spot contrast	$10^{-1} - 10^{-3}$
Satellite Spot location	$11.25\lambda/D, 15.9\lambda/D$
Spectral Resolution (R)	19-90

as soon as a new exposure starts for CHARIS. The synchronization script toggles between the two orientation command as soon as it sees the new exposure, and then it sends command to the SCExAO computer which controls the DM. The time taken to switch from one-spatial pattern to the other is directly linked to CHARIS's cameras exposure (i.e. if CHARIS's exposure is 10s, the spatial pattern will change every 10s just before the exposure begins.) The time taken to send command to the DM is of the order of $10^{-4}s$. Therefore, the maximum speed of the response time of the DM (which includes both actuator displacement and time-lag due to software) is ∼10kHz. The speed modulation pattern is ∼1kHz, which is eight times slower than the typical DM response time. The error caused by this time-lag is considered to be negligible. Also, in my thesis I did not determine the zero point of modulated phase pattern. The zero point of the modulated phase pattern (can be referred to as zero point of the DM) is dynamically controlled by the background extreme AO loop. In this case, the zero point of the DM surface is maintained by the command from the Pyramid Wavefront Sensor loop and is updated at high speed (roughly 200Hz i.e. speed of the extreme AO loop). On top of this zero-point command from the Pyramid wavefront sensor, I apply small amplitude sine wave. The zero point on the DM adds coherence to the static satellite spot, and this coherence is best eliminated by using two same amplitude sine-waves and switching their phases between 0 and π at high speed within an exposure. Also, in this work I used small amplitude sinusoidal waves which correspond to small actuator displacement (roughly of the order of 10nm) perpendicular to the surface of the DM. The actuator stroke of the DM installed on the SCExAO bench is 1.5μm. In this regime the relation between the actuator displacement and the voltage to the DM is linear and doesn't show hysteresis effect. However for large actuator stroke, there might be some non-linear effect which I plan to explore in the future. The following points summarizes in sequence the entire architecture.

- Begin data acquisition with CHARIS
- Start synchronization code
- First CHARIS image is saved.
- Synchronization code toggles to orientation 1, adds incoherent speckle pattern 1 to the DM.
- Second CHARIS image is saved.

- Synchronization code toggles to orientation 2, adds incoherent speckle pattern 2 to the DM.

  ⋮

- Last image is saved.
- Stop synchronization code
- Stop data acquisition with CHARIS

The time lag between two successive commands is not uniform. It depends on the nature of the command. Currently the command to start CHARIS data acquisition and then the start Alternating technique is not fully automated. These are two separate independent commands. After the CHARIS data acquisition command has started, I run the Alternating switching command. My switching code reads a data log file generated by CHARIS computer. As soon as a new exposure starts (or vice-versa the previous exposure ends), the log file is dynamically updated. My switching code detects this update and sends command immediately (∼0.001s) to the DM to change the orientation of sine-wave and also switch the phase of sine-wave at high speed within that exposure. The time lag between two commands from CHARIS data computer to the DM is roughly equal to the exposure time of the images. The Alternating code runs throughout the entire data acquisition period without stopping anywhere in the middle. After the last CHARIS image is saved, I stop the synchronization code and then the CHARIS data acquisition code. The pseudo code and algorithm below was used to acquire CHARIS images with alternating incoherent satellite speckles. The synchronization code was successfully first tested on-sky on the target HR 8799 (H_{mag}=5.3, Spectral type = F0) with brighter (sine-wave amplitude on DM = 25 nm) incoherent satellite speckles. Figure 4.8 shows the on-sky images of HR 8799 with alternating speckle pattern taken on the engineering night of 2018 September 3, 11:37-11.57 (UTC).

```
tail -fn0 data.log | \
while read line ; do
        echo "$line" | grep "Image Saved"
        if [ $? = 0 ]
        then
TOGGLE=$HOME/.toggle
```

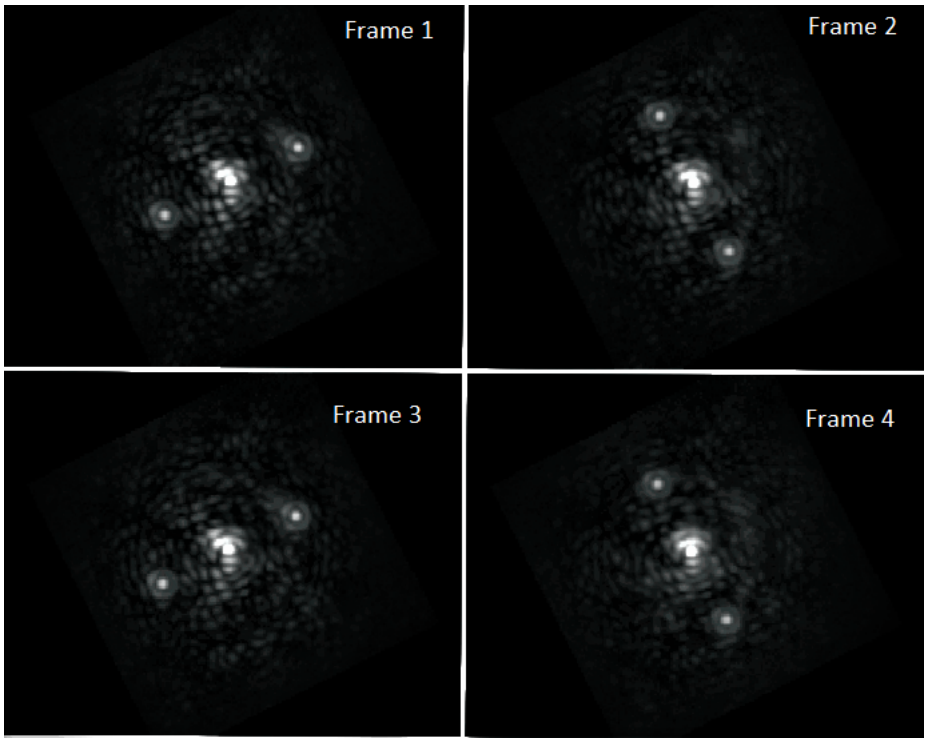

Figure 4.8 Images of four consecutive reduced data slices of HR8799 obtained from CHARIS at 1630 nm showing two alternate speckle patterns created by a single sine wave with an amplitude of 25 nm applied on the DM, at a separation of approximately 0.46" from the central PSF

```
if [ ! -e $TOGGLE ]; then
     touch $TOGGLE
(Add Incohorent Speckle Pattern 1) &
else
     rm $TOGGLE
(Add Incoherent Speckle Pattern 2) &
fi
fi
done
```

4.3 Absolute Contrast Determination

After the first successful on-sky implementation of the *Alternating Speckle Technique*, I acquired data with different brightness of the incoherent satellite speckles in the subsequent engineering

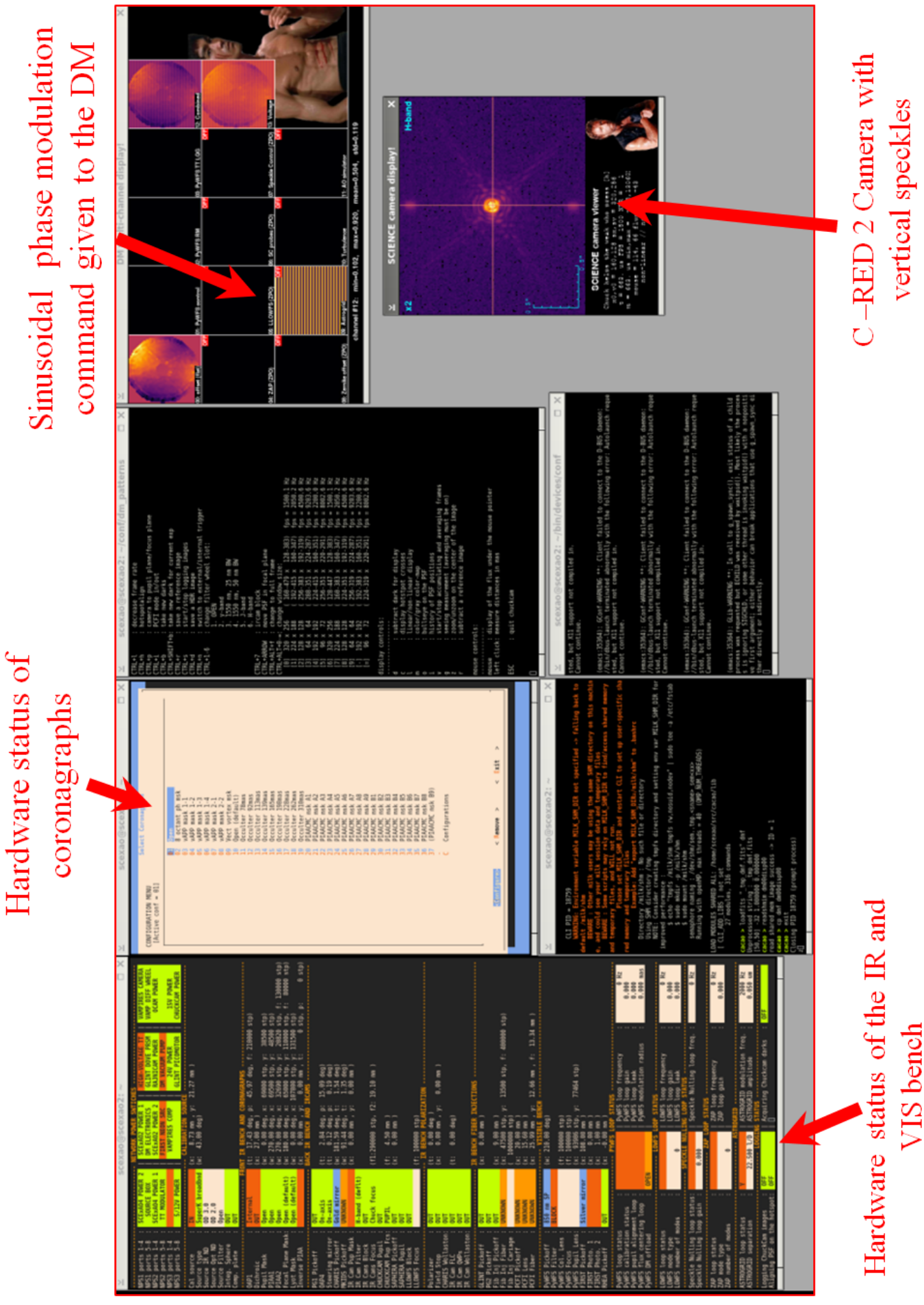

Figure 4.9 A picture of the Graphical User Interface of the SCExAO instrument.

nights. The amplitude of the sine-wave was varied from 6.25 nm to 25 nm to acquire data with satellite spots of different contrast ($\sim 10^{-3} - 10^{-2}$). Due to detector dynamic range limitations, the flux ratio between a fainter satellite spots and the central PSF was indirectly measured with the help of brighter satellite spot using the laboratory super continuum laser source. Figure 4.10 shows the schematic representation of this method where I compute the contrast of 8.8 nm speckle grid through a brighter 50 nm speckle grid. The 50 nm speckle grid was used to register the relative flux between the PSF core and the 50 nm non-coronagraphic satellite speckles at first, and then the relative flux between 50 nm and 8.8 nm satellite spots was computed by inserting a focal plane mask and increasing the exposure time. The spots generated by the 8.8 nm amplitude were expected to be 32 times fainter than the 50 nm amplitude. We obtained a set of 8 monochromatic images as shown in the Figure 4.10 for absolute contrast calibration. This set consists of an unsaturated image of the central PSF (top left), the central PSF with the 50 nm speckles for two different speckle patterns (top middle), the 50 nm speckle grid with the Lyot coronagraph for the two patterns (top right and bottom left), the 8.8 nm speckles with the Lyot coronagraph for the two patterns (bottom middle) and an exposure with the Lyot coronagraph and no additional speckles (bottom right). I address this set of images as 'ladder frames' as I acquired them in steps of decreasing order of sine-wave amplitude on the DM. The relative flux and position of the central PSF and the 50 nm speckle grid without any coronagraph was measured at first and then we measured the flux and position between the 50 nm and the 8.8 nm speckle grid with the Lyot coronagraph. Using these measurements I computed the relative flux and position between the central source and the 8.8 nm speckle. The exposure with the Lyot coronagraph without any satellite speckles is used to subtract the background speckle halo in the coronagraphic images.

The images in figure 4.10 were taken using the CHARIS instrument in broadband mode. In this mode, CHARIS produces a 3D data cube of 22 slices, where each slice corresponds to a 2-D monochromatic spatial image. Therefore, I computed the contrast of 8.8 nm and 50 nm speckle grids at 22 different wavelengths. Figure 4.11 shows the measured contrast variation of the 50 nm and 8.8 nm speckle grids as a function of the wavelength. The flux-ratio between 50 nm and 8.8 nm speckle grid was measured to be 29. The flux of the satellite spots varies inversely proportional to the square of the wavelength of the incident light. This can be analytically understood by the

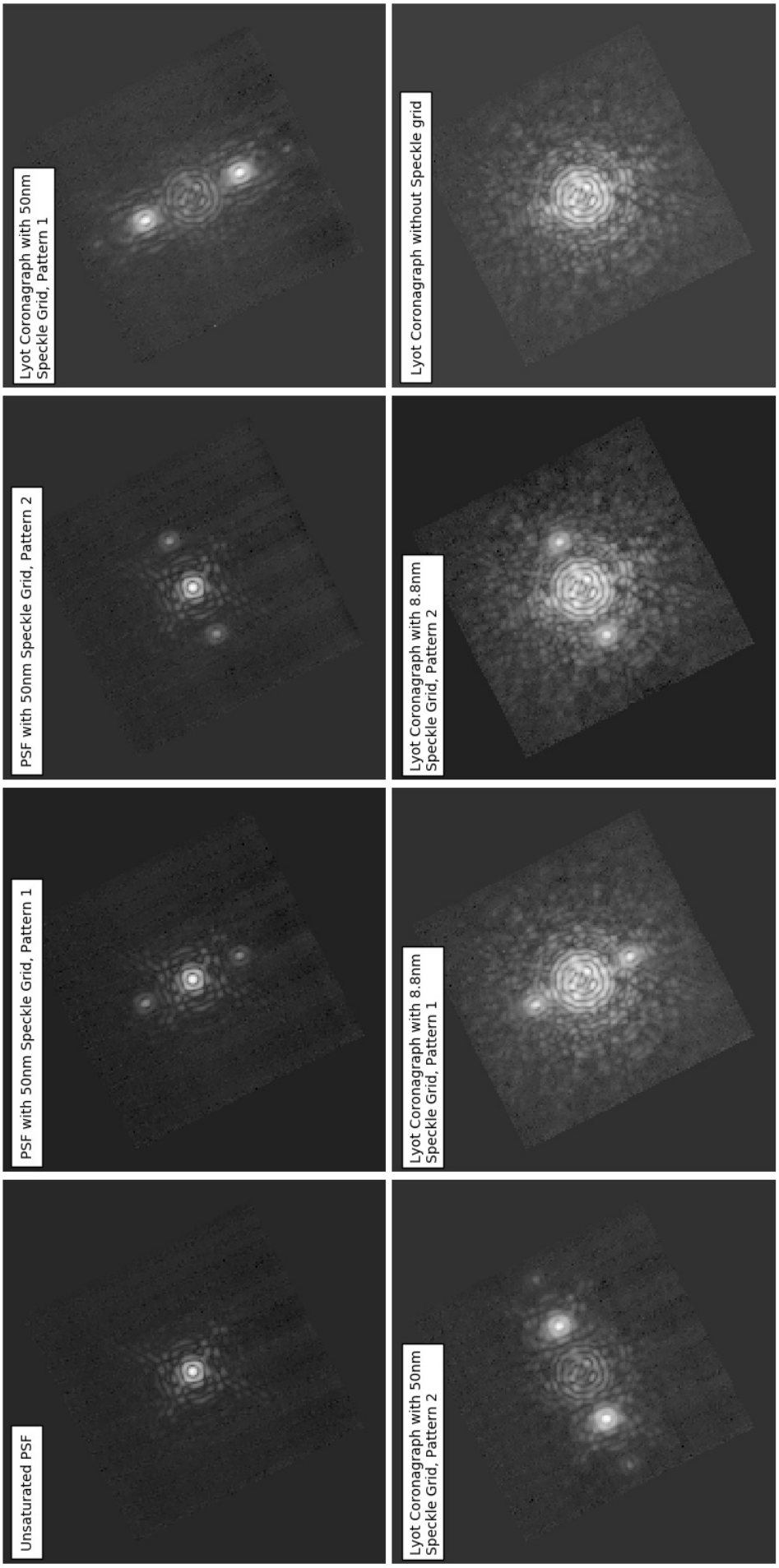

Figure 4.10 Ladder frame for calculating the contrast curve.

following equations:

$$\begin{aligned} I &= |\mathcal{FT}[Ae^{i\phi}]|^2 \\ &= |\mathcal{FT}[A] \star \mathcal{FT}[e^{i\phi}]|^2 \\ &\propto |A \star e^{i\phi}|^2 \end{aligned} \tag{4.1}$$

I is the intensity at the focal plane, $\star$ denotes the convolution operator, A is the amplitude and ϕ is the phase of the pupil plane. In the case of pupil plane phase modulation, is the phase on the DM responsible for generating satellite speckles and introduces optical phase difference (OPD) of $\Delta\phi$. The relation between optical path difference (Δx) and phase difference ($\Delta\phi$) can be written as:

$$\Delta\phi = \frac{2\pi\Delta x}{\lambda} \tag{4.2}$$

For small phase aberrations, we can consider $e^{i\Delta\phi} \approx 1 + i\Delta\phi$, A is uniform within the pupil plane aperture, hence equation (4.1) can be further reduced such that the image complex amplitude is linear with the phase of the pupil plane:

$$\begin{aligned} I &\propto |(1 + i\Delta\phi)|^2 \\ &\propto 1 + \Delta\phi^2 \\ &\propto 1 + \frac{1}{\lambda^2} \end{aligned} \tag{4.3}$$

In equation (4.3), the constant term '1' corresponds to the intensity of the central PSF and the $\frac{1}{\lambda^2}$ corresponds to the intensity of the satellite speckle and it is inversely proportional to the square of the wavelength, and this is in agreement with the flux measured in figure 4.11. The measured contrast in figure 4.11 will be used later on to scale the average pixel-counts obtained for a satellite speckle with the contrast-value at a particular wavelength.

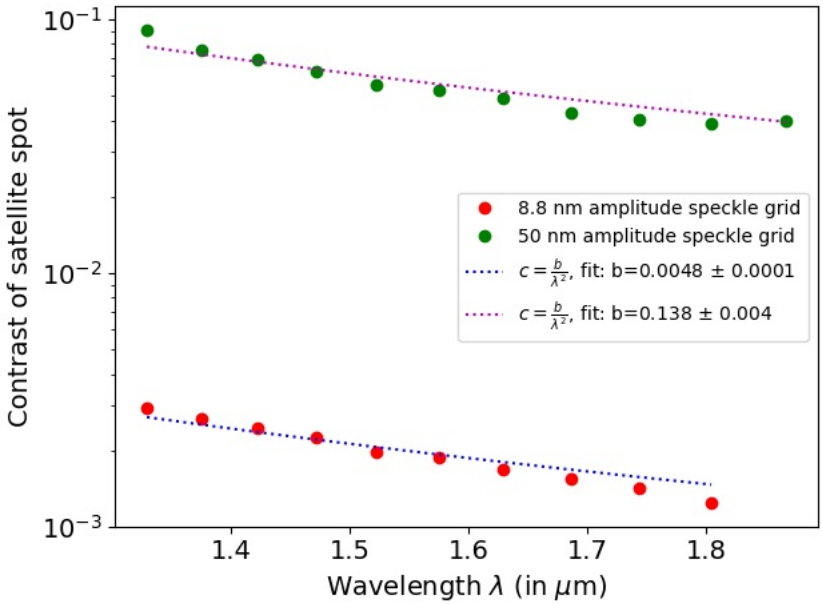

Figure 4.11 Variation of the contrast of the 8.88 nm and 50 nm Speckle grid with the wavelength of the incident beam.

4.4 Summary

In this chapter I discussed the optical layout of the SCExAO instrument with different multipurpose modules, the software control architecture for implementing the *Alternating Speckle Technique* and the ladder frame method used to determine the absolute contrast of the fainter incoherent satellite spots. The upcoming chapters discusses the on-sky photometric and astrometric precision achieved using the alternating technique. The quantitative comparison of our alternating scheme with the commonly used photometric techniques is also demonstrated in the next chapter.

Chapter 5

On-Sky Validation

In this chapter, I discuss some of the on-sky astrometric and photometric precision obtained using the *Alternating Speckle technique*. Section 5.1 discusses the on-sky results obtained on-sky on the target βLeo (A3 star type, $H_{mag} = 1.92$) over a short duration of time (total experiment time =540s). Section 5.2 discusses the on-sky photometric precision achieved on the target tet Hyα(B9.5V star type, H_{mag}=4.0) over a long time duration (total experiment time $\sim$ 3 hours). The raw data were reduced using the CHARIS data reduction pipeline [T. D. Brandt et al. (2017)]. The relative flux and position of each speckle was measured by fitting the image of the satellite speckle to an analytical Airy disk function using least-square fitting method. The maximum flux count, coordinates of the pixel with maximum flux, average flux in an annulus surrounding the image (to estimate the background offset under the fitted-function) were given as an initial condition to estimate the PSF. From the fitting, we obtained the amplitude and center of the fitted function to compute the flux ratio and position coordinates of the satellite speckle w.r.t to PSF core.

5.1 Least Square Fitting Method

In specific, I used the Levenberg-Marquardt algorithm to fit the data points with an obscured airy pattern. This method is widely used to solve non-linear least square problems. As there are two possible options for the algorithm's direction at each iteration, the LM is more robust than the Gauss-Newton (Nelles, 2001). It's faster to converge than either the GN or gradient descent on its own. It can handle models with multiple free parameters which aren't precisely known (note that for very large sets, the algorithm can be slow). If your initial guess is far from the mark, the

algorithm can still find an optimal solution. The analytical form of this function is defined below.

$$I(r) = \frac{I_0}{1-\epsilon^{2^2}} \left(\frac{2J_1(R)}{R} - \frac{2\epsilon J_1(\epsilon R)}{R} \right)^2 \tag{5.1}$$

In equation, 5.1 $I(r)$ represents the intensity of the obscured airy function as function of the radial distance r from the center of the optical axis, I_0 is the maximum peak intensity of the function, ϵ is the ratio of the radius of the obscured disk to the radius of full aperture beam, $R = \frac{\pi r}{\lambda N}$ where λ is the wavelength of the incoming light, N is the f-number of the system and J_1 is the Bessel function of the first kind of the order one. A rectangular area (24×24 pixels) surrounding the PSF of the satellite spot was cropped out from the whole image. I chose a small window just to include the Satellite spot with its first Airy ring. Using bigger size window reduces the quality of the fit.

5.2 On-sky Validation of the *Alternating Speckle Technique*

Figure 5.1a shows two consecutive on-sky images of β Leo with incoherent satellite speckles generated using 8.8 nm DM amplitude. The level of the background speckles is much higher on-sky than in the laboratory due to the residual atmospheric wave front errors. Hence, 8.8 nm speckle spots which are clearly visible with the laboratory source are barely visible in on-sky reduced data cubes as shown in Figure 5(a). However, after subtracting two consecutive frames they can be easily located as seen in Figure 5(b). Each frame has a set of two speckles. The flux and separation of these speckles were measured.

For convenience, let the top right speckle in the left-hand panel of Figure 5.1b be I_1 and the bottom left speckle on the same image be I_2. Figure 5.2a and 5.2b shows the measured flux variation of I_1 without and with background subtraction over a duration of 540 seconds at three different near infrared wavelengths (J, H and K band) with a cadence of approximately every 30s. The exposure time for each frame was kept at 10.32 seconds. The changes in the flux of I_1, is possibly due to variations in SR and background. The standard deviation in the flux measurement improves after subtraction thanks to proper background subtraction. The results are summarized in the table 1.

Figure 5.3a and 5.3b shows the variation of separation between I_1 and I_2 with time before and after subtraction. After subtraction, the astrometric precision significantly improves from 50 milliarcsecond(mas) to 20 mas in J band and slightly improves from 23 mas to 20mas in H-band.

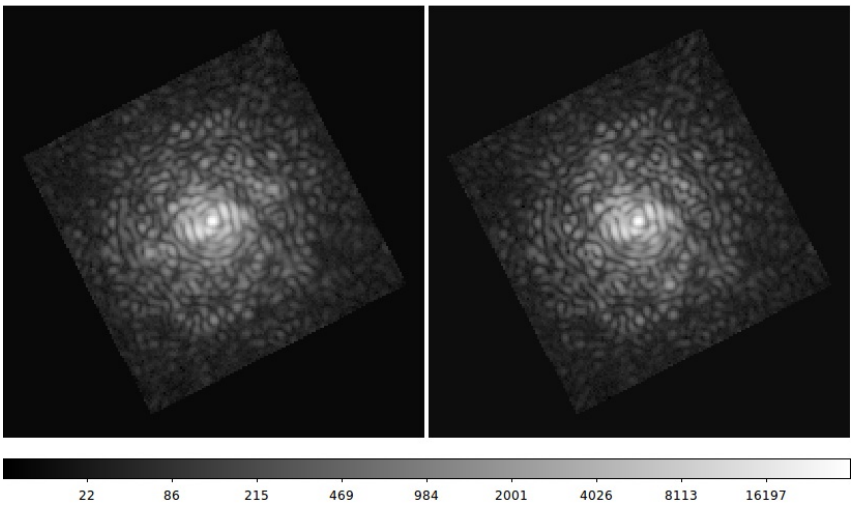

(a) Before subtraction

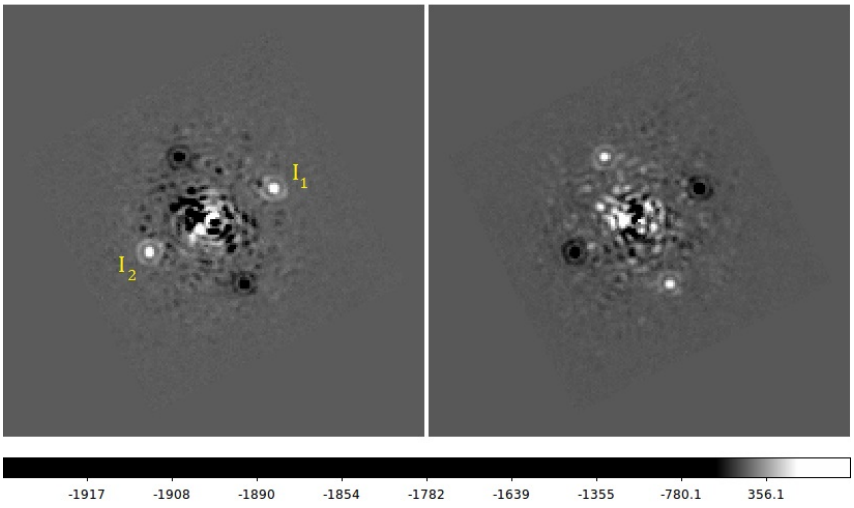

(b) After subtraction

Figure 5.1 On-sky images of two consecutive reduced data slices of β Leo (a)before subtraction and (b) after subtraction obtained from CHARIS at 1744 nm with two alternate fainter speckle patterns where they are barely visible.

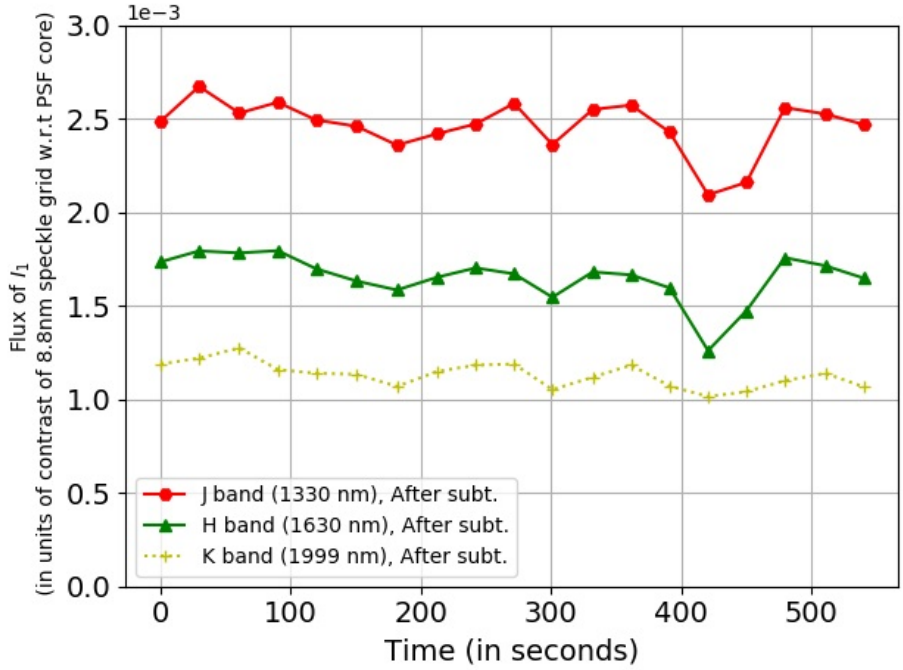

(a) Before subtraction

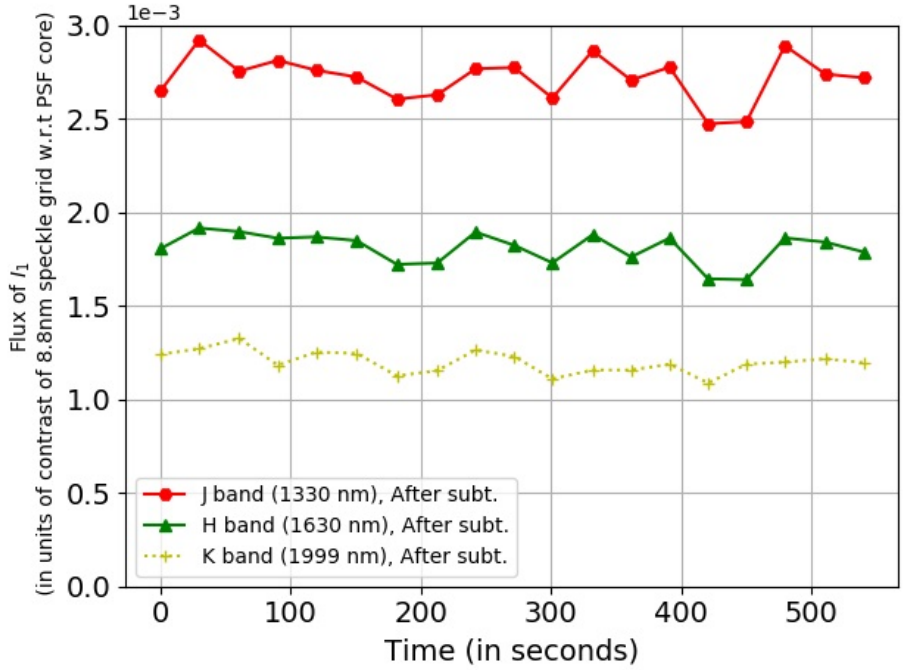

(b) After subtraction

Figure 5.2 Flux variation of one of the speckle before (upper panel) and after (lower panel) subtraction. Flux is expressed in unit of contrast based on static calibration from the previous Figure.

However, in K-band, due to low signal-to-noise ratio of the satellite speckle, I did not measure any improvements. These results are summarized in table 1.

Using two alternating speckle patterns, we estimate the relative error associated with the measurement of the flux ratio between the companion and the central star. For this, we consider one of the speckle spots (i.e. I_1) to be the companion and the other spot to be the calibrator (i.e. I_2). Recall in chapter 3 that the relative error (i.e.) in the measurement of the ratio of intensities of I_1 and I_2 is equal to error in the measurement of the companion and the central star flux. Figure 5.4a and 5.4b show the flux ratio between speckles I_1 and I_2 before and after subtraction respectively. The standard deviations in measurement improves by subtracting two frames from each other for J and H-band. I_1/I_2 in figure 5.4a for J and H-band is always less than unity, suggesting that there is a bias in the measurement of I_1/I_2 without subtraction. Whereas, in the figure 5.4b, I subtracted the underlying background sitting beneath the satellite speckle by taking two exposures with different satellite speckle pattern and measured the intensities of the clearly visible satellite spots. When I subtract two consecutive images, the common static background disappears, and the ratio is closer to unity. Since I expect the ratio between two satellite speckles to be constant over time, this indicates that even between consecutive images, the background changes by about 3.7% (H-band). Assuming this background level to be random, we expect the relative flux between the companion and central PSF can be measured to a precision of 3.7% (in H-band) using Equation 7 for a 10s frame exposure.

I binned N (where N is a positive integer) frames together and measured the relative flux (I_1/I_2) and separation ($|\vec{I_1}-\vec{I_2}|$) of the resultant pair of speckle spots in each binned frame. I then computed standard deviation in the measured relative fluxes and distances for each of the N-binned sets. Figure 5.5a and 5.5b shows the variation of the standard deviation between the measurements (before and after subtraction) with different binning numbers. In figure 5.5(b) the standard deviation without subtraction does not converge with increase in N, suggesting that with increase in number of exposures, the precision of measurement may not improve. However, for subtracted frames I observe that decreases with N in a way that is consistent with 1N. This indicates, that subtracting two consecutive frames has removed the biased incoherent speckle halo from I_1/I_2 measurements to significant extent. Therefore, with an increase in the number data points, I expect the residual uncorrelated noise to become further negligible and obtain an unbiased precise flux measurement.

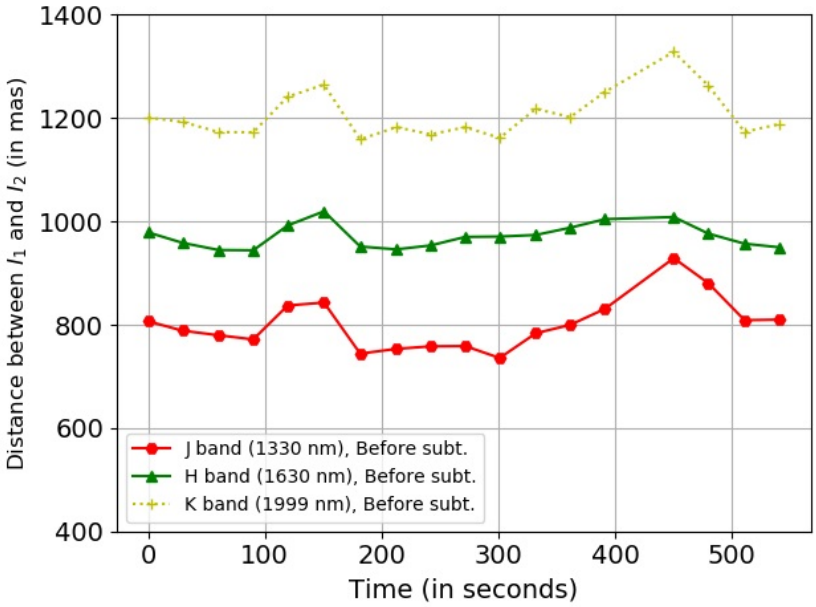

(a) Before subtraction

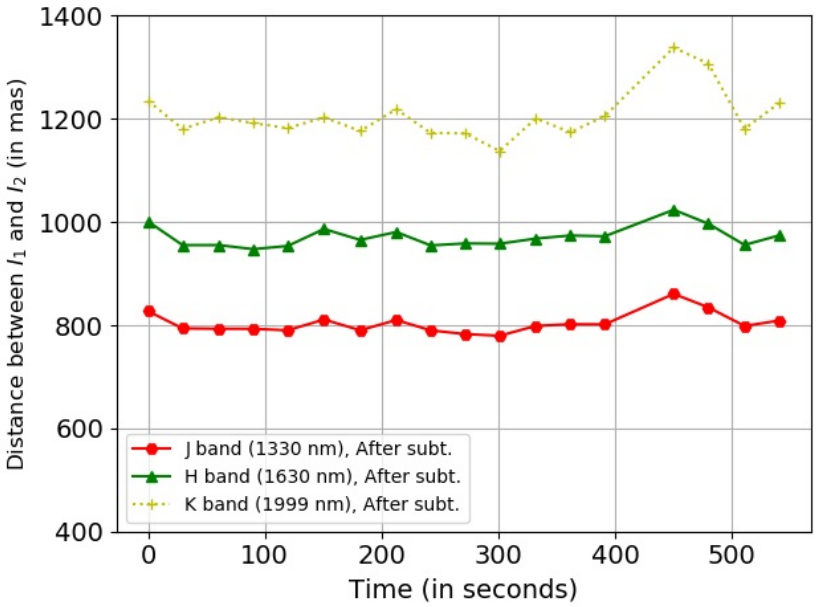

(b) After subtraction

Figure 5.3 Distance variation between I_1 and I_2 with time before and after subtraction.

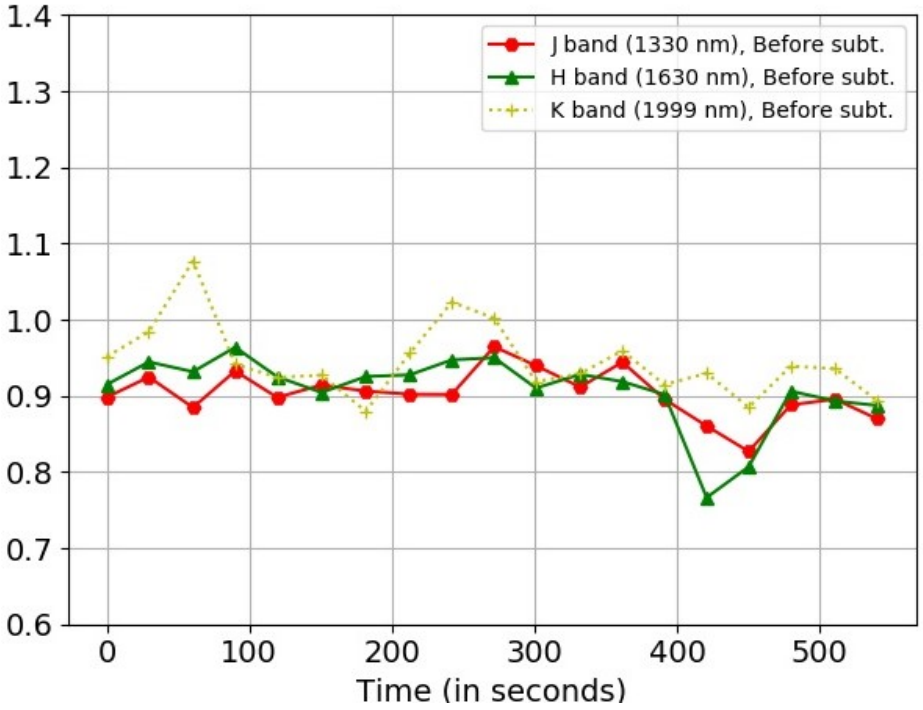

(a) Before subtraction

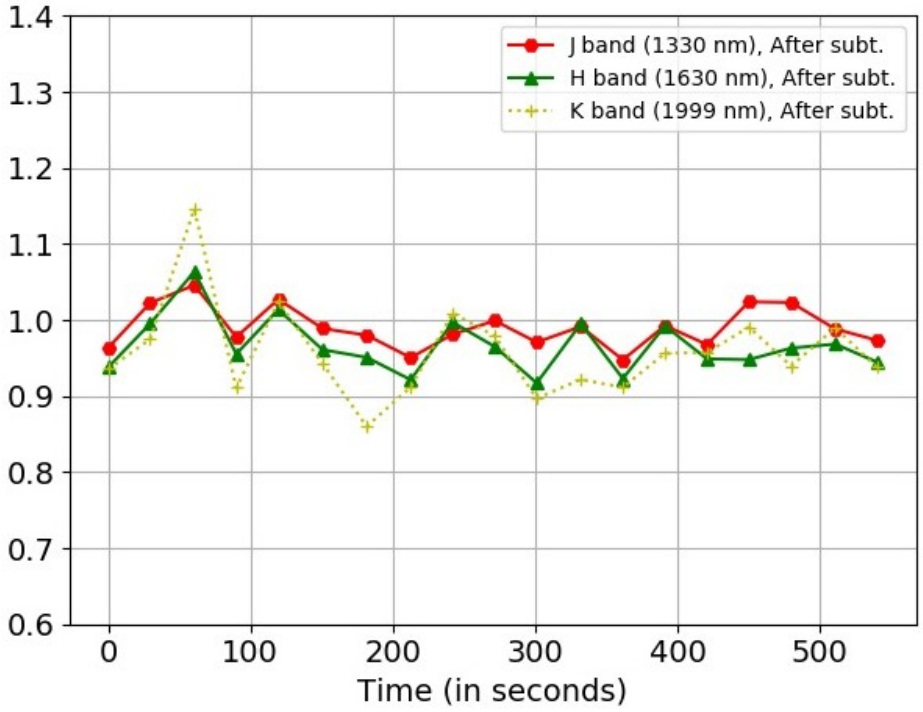

(b) After subtraction

Figure 5.4 Measured flux ratio of I_1 and I_2 as a function of time before (a) and after subtraction (b).

The term "correlated" or "uncorrelated" here means that any two flux measurements are not related in time. The measurement of one flux is unaffected by the past or future measurement. For a 80s frame exposures we can measure the relative flux between the companion and host to a precision of 1% as well as the position to a precision of 5-mas in H-band.

5.3 On Sky precision for a Science Observation

In this section, I discuss the on-sky result obtained on the stellar target tet Hya (B9.5V star type, H_{mag}=4.0) over a timescale of 2.7 hours with 15 nm DM grid amplitude. The main motivation to acquire data over a long time series was to do quantitative comparison with regular photometric or astrometric methods used in the community. The precision achieved with this data set provides a realistic approximation on the photometric precision that we can achieve during a regular science observation night. I carried similar analysis as described above. Figure 5.6 shows the flux as of the satellite spots as function of time with (red dots) and without (green dots) background subtraction. The flux slightly decreases after background subtraction, however it varies in the same fashion with time as without any background subtraction. This variation is solely attributed to variation of Strehl over the entire observation duration.

The effect of Strehl is eliminated by dividing two flux measurement as shown in Figure 5.7. This ratio is closer to unity in the case of measurements where the static background is subtracted (green dots in Figure 5.7).

I further binned several measurements as described in section 5.1 and calculated the standard deviation in the resultant binning sets (refer to figure 5.8 and 5.9). In figure 5.8, SR is present in the flux measurement. Even after the subtracting the background, the standard deviation do not converge as per $1/(\sqrt{N})$. Therefore, subtracting the background from measurement will not remove the correlated noise from the system. In figure 5.9, effect of Strehl is eliminated as we take the ratio of two measurements. When the background is not subtracted from the relative flux, the standard deviation does not converge with binning (refer to red dots in figure 5.9). Taking more exposures will not improve the photometric precision. Whereas, in the case when the background is subtracted from the relative measurements, the standard deviation converges with binning as per $1/\sqrt{N}$ law (refer to green dots in figure 5.9). Taking more of data point will improve the accuracy

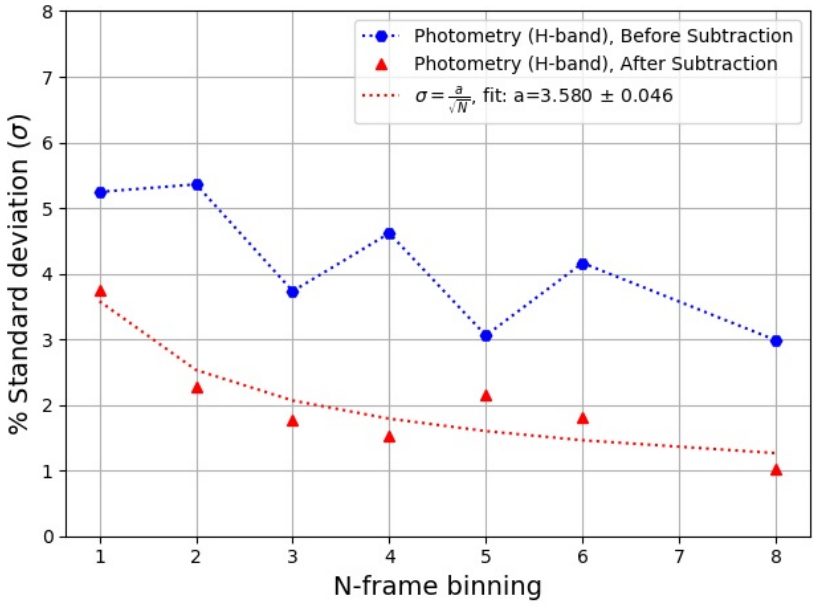

(a) Photometry

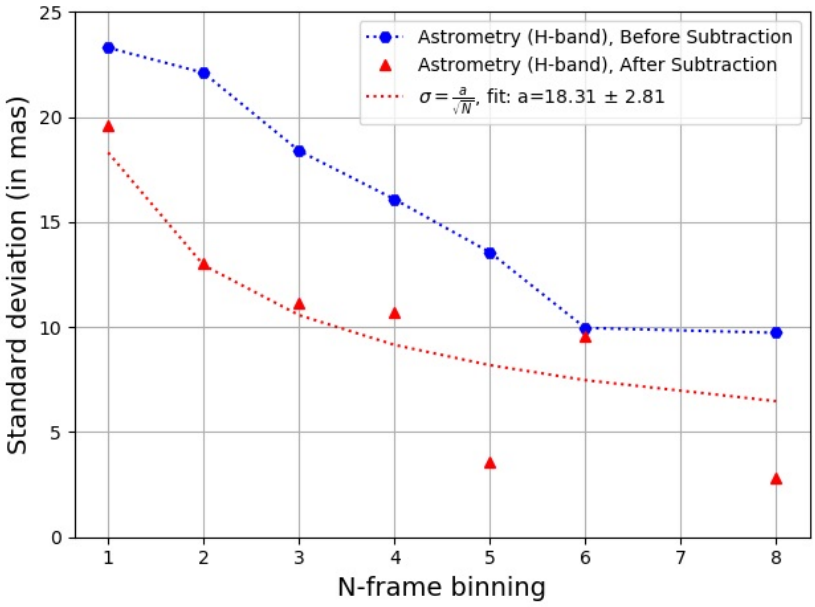

(b) Astrometry

Figure 5.5 Photometric and Astrometric Precision with different Binning Numbers. (a)Photometry: Variation of Standard deviation in the measurement I_1/I_2 with different binning numbers. (b)Astrometry: Variation of Standard deviation in the measurement of $|\vec{I_1} - \vec{I_2}|$ with different binning numbers.

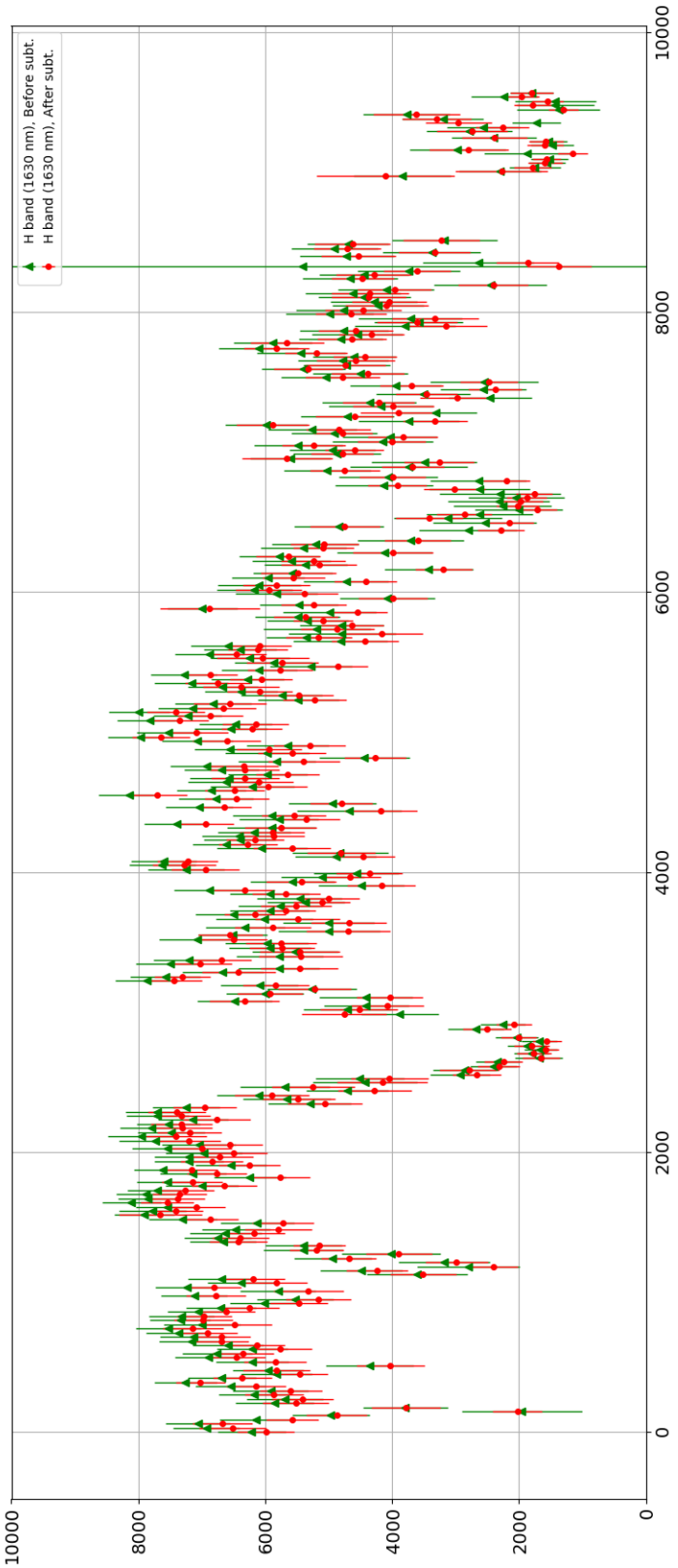

Figure 5.6 Variation of the flux of one of the satellite speckle over a longer time-series in H-band. The flux slightly decreases after background subtraction, however it varies in the same fashion with time as without any background subtraction. This variation is solely attributed to variation of Strehl over the entire observation duration.

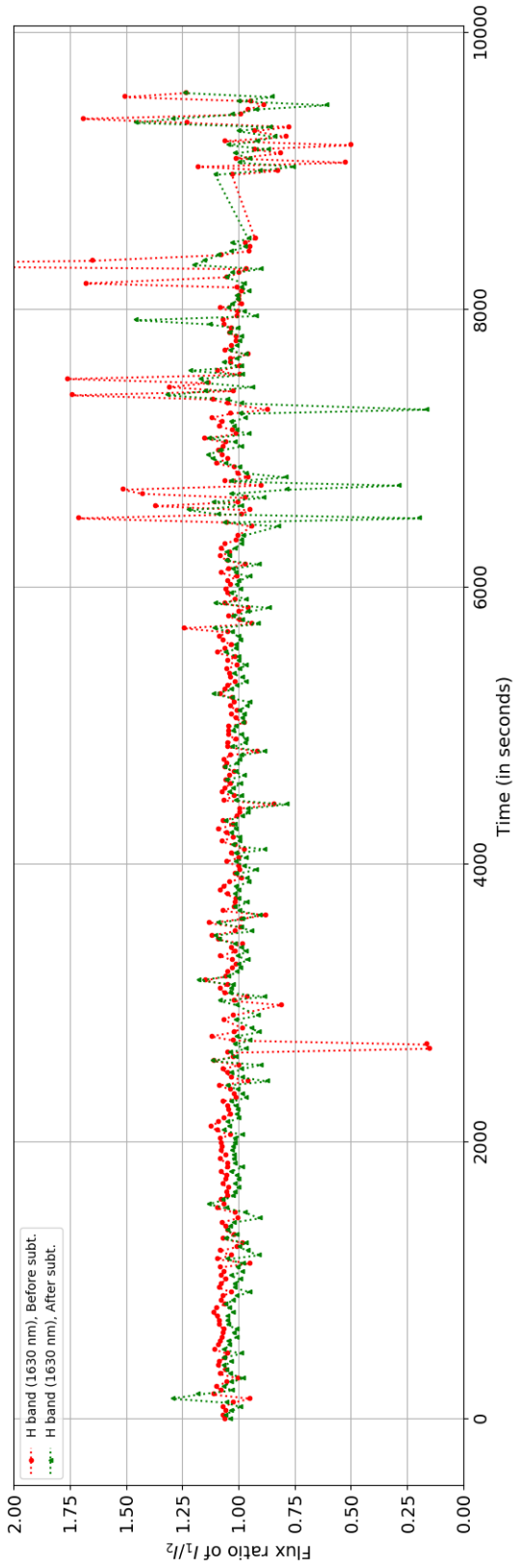

Figure 5.7 Ratio of flux variation of a pair of incoherent Satellite Speckles.The effect of Strehl is eliminated by dividing two flux measurement. This ratio is closer to unity in the case of measurements where the static background is subtracted (green dots).

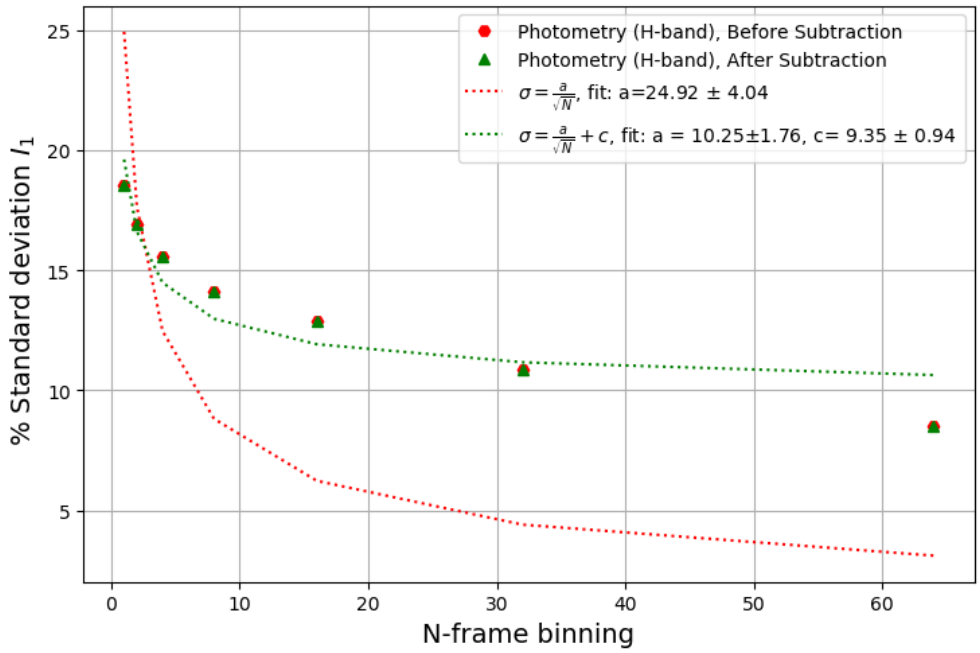

Figure 5.8 Variation of standard deviation on the flux measurement of one of the satellite speckles with different binning number. Here, SR is present in the flux measurement. Even after the subtracting the background, the standard deviation do not converge as per $1/(\sqrt{N})$. Therefore, subtracting the background from measurement will not remove the correlated noise from the system.

of our measurement. This is because our measurement is limited by random uncorrelated noise. Whereas when the F_{bg} term is not subtracted from the measurement, we would achieve a photometric precision of 10% on the same stellar target under the same environmental conditions. With this data, we can clearly except, *Alternating Scheme* to produce a better photometric precision.

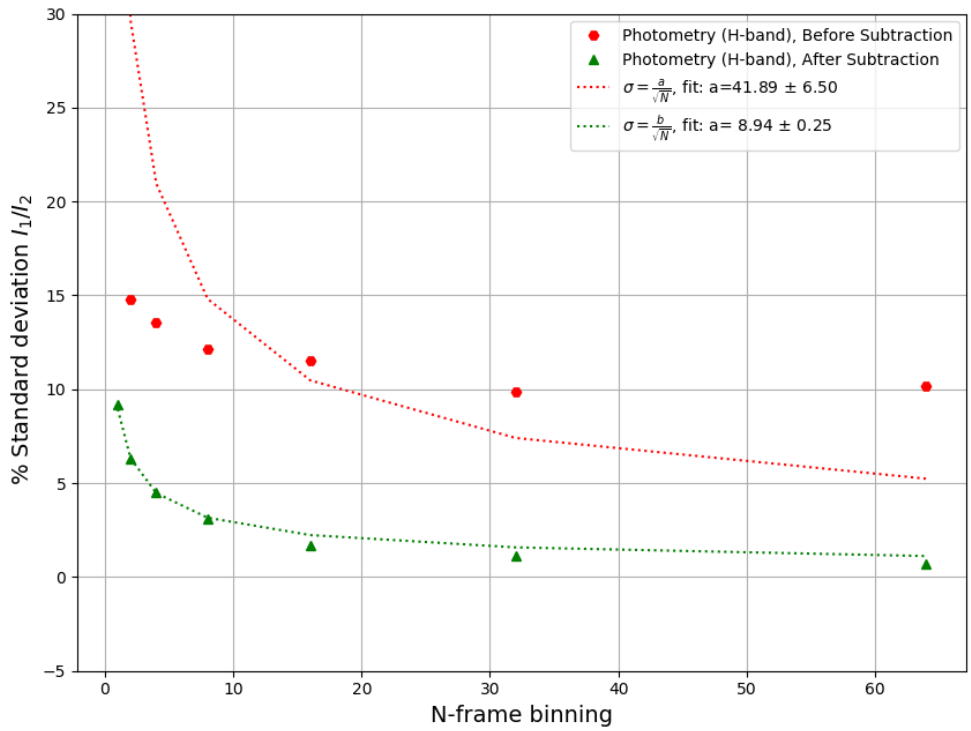

Figure 5.9 Variation of standard deviation on the relative flux measurement with different binning numbers. Here green dots represents standard deviation of the measurements, where both the SR and the underlying static background F_{bg} is absent. The standard deviation converges with binning as per $1/\sqrt{N}$ law (refer to green dots). Taking more data point will improve the accuracy of our measurement. This is because our measurement is limited by random uncorrelated noise. There is a clear improvement in photometric precision from 10% to 0.5% under the same environmental conditions, when the incoherent static background is subtracted from the measurement.

Table 5.1 Photometric and Astrometric Precision Obtained (for 10s frame exposure)

Wavelength (in nm)	Photometry (I_1) % Standard Deviation σ	Astrometry $\lvert\vec{I_1} - \vec{I_2}\rvert$ Angular Separation (in mas)	Ratio ($\frac{I_1}{I_2}$) % Standard Deviation σ
	Before Subtraction		
1330	5.8	51	3.5
1630	7.7	23	5.2
1999	6.0	45	5.1
	After Subtraction		
1330	4.5	20	2.8
1630	4.6	20	3.7
1999	5.0	47	6.4

5.4 Background Signals and Noises

5.4.1 Noise in Laboratory Conditions:

Laboratory conditions refer to an environment free of any wavefront aberration. Therefore, the PSF is a perfect Airy disc. The major sources of error in laboratory conditions which affects the position and flux measurement of the PSF are described below:

- **Photon Noise** Photon noise is generated due to the uncertainty associated with the particle the nature of light. This is a fundamental physical phenomenon which reflects the quantum fluctuations of an electromagnetic wave. Thus, the photons generated by any light source reach the detector at different times. At equally spaced time stamps, the number of photons collected within a particular aperture area follows Poisson distribution. Let N_s be the numbers photons from the actual source signal. Therefore, the photon noise associated with the signal is: $\sigma_{phot} \approx \sqrt{N_s}$.

- **Readout noise:** This noise is generated by the detector in the process of converting an analog signal to a digital value i.e. converting the number of photons collected to a corresponding number of electrons and then to the digital signal (or pixel value). The readout noise can be simply be measured by subtracting two images and measuring the standard deviation of the resultant subtracted image: $\sigma_{read} \approx \frac{\sigma_{im1-im2}}{\sqrt{2}}$

The final pixel value can be expressed in terms of detector gain and readout noise as follows:

$$F \pm \sigma_F = (g * N_s + c) \pm \sigma_{tot} \tag{5.2}$$

where F = the pixel count

g = gain of the detector

c = Base pixel value / detector dark counts, (a non-zero constant quantity)

$\sigma_{tot} = \sqrt{{\sigma_{phot}}^2 + {\sigma_{read}}^2}$

A Numerical Example: The total photons F from a star (HR8799, $m_H = 5.3$) collected by a telescope can be expressed in terms of telescope's diameter D, global throughput in front of the detector q, flux density for a zero magnitude star in the H band f_0, spectral band width ($\Delta\lambda$) and exposure time t be expressed as follows:

$$F = \frac{\pi}{4} D^2 q f_0 10^{-0.4*m} t * \Delta\lambda \tag{5.3}$$

The zero point flux density in the H-band is 9.444×10^9 photons $m^{-2}s^{-1}\mu m^{-1}$ (to calculate flux in other bands, refer to Figure 5.10). The flux (in terms of number of photons) accumulated for a 20.65s CHARIS exposure (total throughput before the detector $\sim 15\%$, quantum efficiency ~ 0.8 in H-band [N. Jovanovic et al. (2015a), T. D. Groff et al. (2016), Finger et al. (2008)], the throughput at other wavelength is summarised in Table 5.2) can be calculated as follows:

$$\begin{aligned} F &= \frac{\pi}{4}(7.9)^2 * 0.15 * 0.8 * 9.444 * 10^9 * 10^{-0.4*5.3} * 20.65 * 0.08 \\ &\approx 7 * 10^8 photons \end{aligned} \tag{5.4}$$

In the above equation is for a perfect Airy disk and 90% of the total photons lie within the first Airy ring. For a satellite spot formed by 25nm sine-wave amplitude, the contrast of the satellite spot w.r.t to the central PSF is $\sim 2.5 * 10^{-3}$. The flux of one of 25nm satellite spot is $2.5 * 10^{-3} * F = 1.75 * 10^6 photons$. The photon noise for this satellite spot is $\sqrt{1.75 * 10^6} = 1.32 * 10^3$ photons. This photon noise corresponds to a photometric error of 0.08% (i.e $1/\sqrt{1.75 * 10^6} = 0.0008$) when the peak intensity of the satellite spot is calculated. The astrometric error associated with the photon noise is 0.015mas which is computed as follows [Cameron, Britton, and Kulkarni (2008)]:

$$\sigma_{astro} = \frac{\sqrt{2}\lambda}{D} \frac{1}{\sqrt{1.87 * 10^6}} \tag{5.5}$$

For CHARIS instrument, $\frac{\lambda}{D} \approx 3$ pixels, so $\frac{\lambda}{D} = 48mas$. Thus equation 5.5, can be reduced to:

$$\sigma_{astro} = 3 * 16.2 \frac{\sqrt{2}}{\sqrt{1.87 * 10^6}}, \tag{5.6}$$

$$= 0.02mas \tag{5.7}$$

The background noise (dominated by readout noise) $\sigma_{read} \approx 7$ ADU $=2240$ *photons* (refer to §5.3.2 for the calculation in units of photon). The total noise in the system $\sigma_{tot} \approx \sqrt{F}$. In laboratory condition I estimated, the error due to photon noise and background noise are of similar strength (i.e. $\sigma_{phot} = 1320$, and $\sigma_{read} = 2240$ (in units of number of photons)). Signal to noise ratio can be further improved by increasing the exposure time.

Table 5.2 Total Instrument Throughput

Band	Atmos.	Teles.	HWP	ADC	AO188	SCExAO	CHARIS (internal)	QE
R	91	82	93	95	68	-	-	-
I	96	75	95	95	69	-	-	-
z	97	79	95	95	69	-	-	-
y	98	80	94	95	72	-	-	-
J	95	91	96	94	77	60	40	79
H	97	92	94	92	79	58	40	79
K	92	93	92	70	82	-	40	80
(J+H+K)	-	-	-	-	-	-	53	-

Throughput in terms of % for each wavelength band through atmosphere, telescope, AO188's Half Waveplate (HWP), Atmospheric Dispersion Compensator (ADC), AO188, SCExAO bench, CHARIS and quantum efficiency (QE). In my case of the numerical example, the global throughput is $0.97 * 0.92 * 0.94 * 0.92 * 0.79 * 0.78 * 0.53 * 0.79 = 0.18$.

Photometry

Conversion between Jy and ph.s-1.m-2.um-1:
1 Jy = 1.5091904E7 / lambda(um) ph.s-1.m-2.um-1

Band	B	V	R	I	J	H	K	L	M
Effective wavelength (um)	0.436	0.545	0.638	0.797	1.22	1.63	2.19	3.45	4.75
zeroth mag flux (Jy) (Johnson-Cousins-Glass)	4000	3600	3060	2420	1570	1020	636	281	154
ph.s-1.m-2.um-1	1.3846E11	9.9690E10	7.2384E10	4.5825E10	1.9422E10	9.4440E9	4.3829E9	1.2292E9	4.8930E8

Figure 5.10 Vega Flux Zeropints [Bessell, Castelli, and Plez (1998), Girardi et al. (2002)]

5.4.2 Noise during On-sky Observation

During an observation sequence, the main sources of noises are residual speckle noise, readout noise, photon noise and error in measurement of detector flat-fields. Residual speckles present in a post coronagraphic AO images can be formed due to imperfect AO corrections or due to non common path aberrations (NCPA). NCPA give rises to static speckles in the image. Non-common path error is minimized using various real time algorithm such as focal plane wavefront sensing (FPWFS) [Martinache, Nemanja Jovanovic, and Olivier Guyon (2016), Olivier Guyon, Gallet, et al. (2006)]. I use one of this technique to stabilize the satellite spot PSF. Background sky emission, stray light, error in detector QE and stellar source; all of these parameters can be grouped together to estimate the resultant total photon noise.

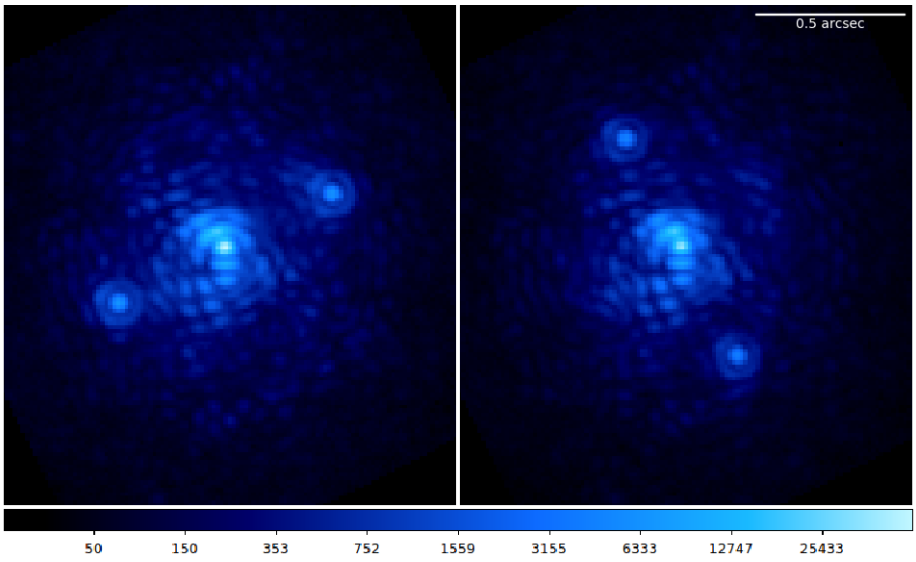

Figure 5.11 Two consecutive images of HR8799 with 25 nm DM amplitude speckle grid at separation of $11.25\lambda/D$ from the core.

To estimate the strength of these noise sources, I took two consecutive on-sky CHARIS data (see figure 5.11) with two different satellite speckle patterns. The satellite speckles are of the order 10^3 fainter than the central star. The total error in the system is computed as follows:

- **Photon noise**
  - The contrast of the 25nm satellite speckle w.r.t to the central PSF is $2.5 * 10^{-3}$. The photon noise for this satellite spot is $\sqrt{1.75 * 10^6} = 1.32 * 10^3$ photons. This photon noise corresponds to a photometric error of 0.08% (i.e $1/\sqrt{1.75 * 10^6} = 0.0008$) and astrometric error of 0.02mas as calculated in the §5.4.1.

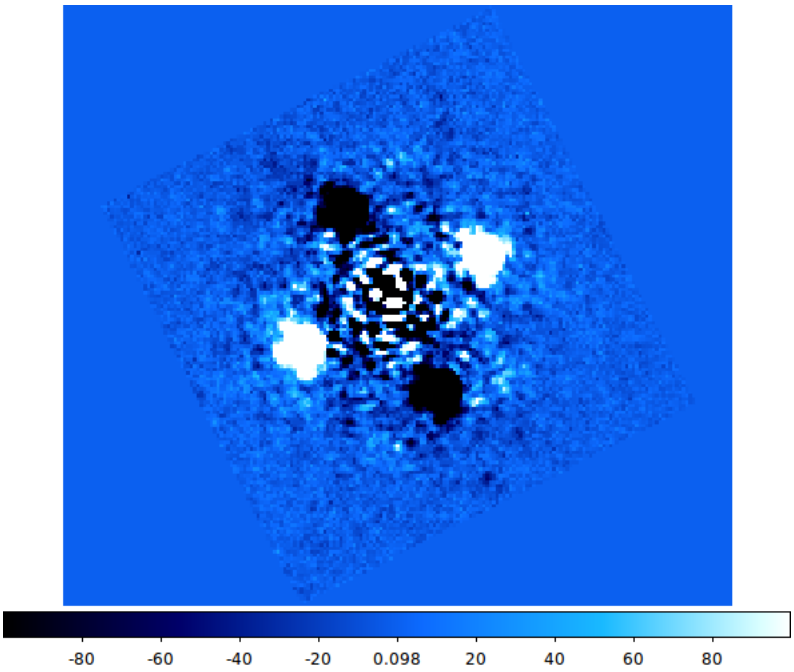

Figure 5.12 Difference between two consecutive images of HR8799 with 25 nm DM amplitude speckle grid at separation of $11.25\lambda/D$

- **Speckle Noise**

  - The number of photons per pixel in the halo of the subtracted image is $\sim 1.3{*}10^{-5} \times F = 8.125 * 10^3$. This is the noise (in terms of number of photons) due to the motion of the speckles between two images. Hence the speckle noise, $\sigma_s \approx 9750$ photons. Also, the contrast (after background subtraction) of the speckle halo w.r.t to the 25 nm satellite spot is 10^{-2}. This contrast give rises to a photometric error of 1% (i.e. (Mean intensity of halo)/Intensity of the spot)*100).

  - To estimate the astrometric error associated with speckle halo of relative contrast of 10^{-2} w.r.t to the spot, I simulated a 1-D Airy function and with a sinusoidal speckle background as shown in Figure 5.14. For astrometric error estimation, I monitored only on how the peak radially shifts in presence of an underlying background. In a subtracted image, there would be negative as well as positive pixel values of the speckle halo just beneath the Airy disk within an circular region of diameter $2\lambda/D$. A sine wave is close approximation of the intensity profile from the speckle noise in the halo. In this case, the relative amplitude of the sine-wave and the Airy function was kept at 0.01 (i.e. equal to the contrast of the speckle halo w.r.t to the spot as obtained from

Figure 5.12). I estimated that the peak of the resultant added function shifts by 0.01 radial units. For CHARIS camera, $\lambda/D \approx 3$ pixels. This 0.01 shift (in radial units from Figure 5.14) corresponds to a shift 0.012 CHARIS pixels, and thus an astrometric error of $0.012 * 16.2 = 0.2$ mas. For a 2D PSF, the resultant astrometric error $= \sqrt{2} * 0.2 = 0.3$ mas.

- **Background Noise**

  - Similarly, the background noise (primarily dominated by readout noise) is calculated by subtracting two close dark frames and calculating the resultant pixel deviation in the subtracted image. In this case, I calculated the readout noise by measuring the RMS pixel value at the edge of the Figure 5.12. In Figure 5.11, the edge of the images has no light, therefore, subtraction of these two images and looking at the edge in the subtracted image will give me an estimation of the readout noise. The RMS pixel value ≈ 7 ADU in the edge of Figure 5.12. Technically, this would also include photon noise from thermal background. But due to short exposure time, the readout noise dominates over the photon noise from background.

  - The relative contrast of the read noise w.r.t to the satellite spot was measured to be 10^{-3}. To estimate the photometric error associated with this read noise, I simulated a 1D Airy function similar to that of the CHARIS's satellite spot (i.e. same sampling as that of the satellite spot where the peak constitutes of 2 data points; see Figure 5.15). I added a set of random numbers having variance 0.1% and mean of 0 to the Airy function as shown in Figure 5.15 . I did a Monte Carlo Simulation to generate 10^5 possible outcomes of relative change in the peak intensity due to a 0.1% random error. The histogram in Figure 5.16 shows all the possible outcomes. And the root mean square values of these outcomes is ~ 0.00066. This leads to a photometric error of 0.06%.

  - Similarly, the astrometric error due to detector read noise was calculated by estimating the relative shift in the photo-center of the peak intensity of the satellite spot's PSF when each pixel has a random error of 0.1%. Figure 5.17 shows all the possible outcomes when the each pixel of the under sampled Airy function has a random error of 0.1%. The root mean square of all these outcomes is 0.00039 pixels of the under sampled airy

function. This scales to 0.01 mas in CHARIS pixel.

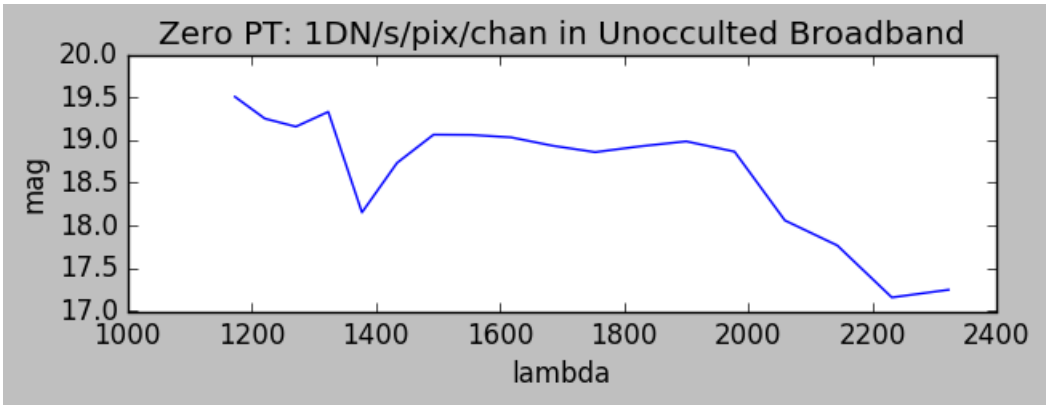

Figure 5.13 The zero point flux-magnitude for CHARIS. The estimated zero point of CHARIS in broadband mode is H = 18.7. This will yield 1 count/s/spectral channel.

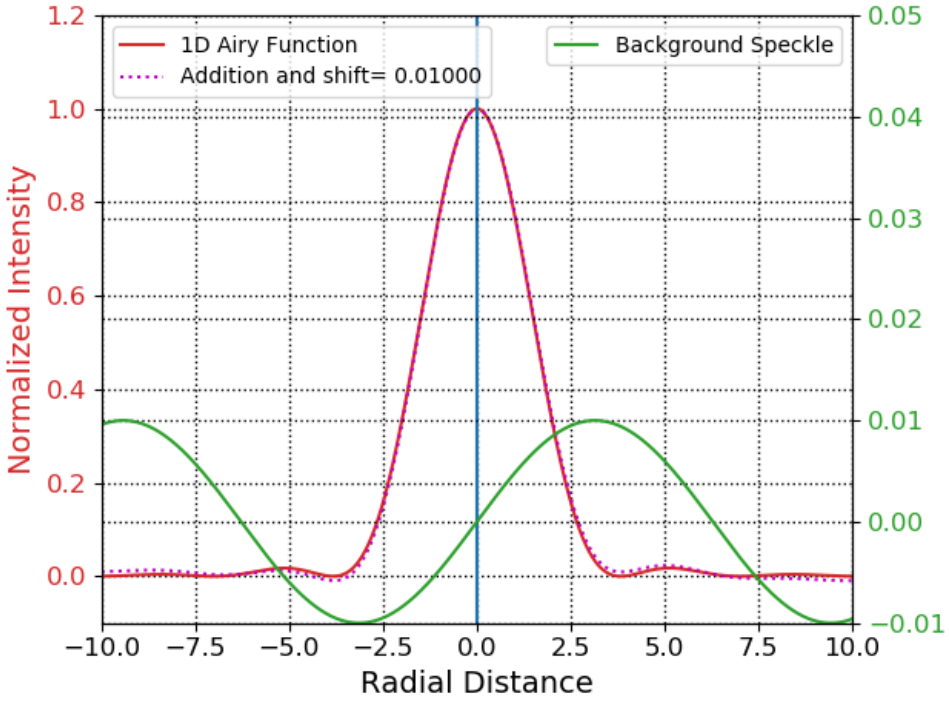

Figure 5.14 The astrometric error due to speckle noise was calculated by estimating the relative shift in the peak intensity of the satellite spot's PSF when a simple sinusoidal speckle background is added.

5.4.3 Detector Flat fielding

A field flat is basically an image taken with the detector where the illumination is uniform across the entire FOV. Flat field images are taken to measure response of each the pixel to a uniform

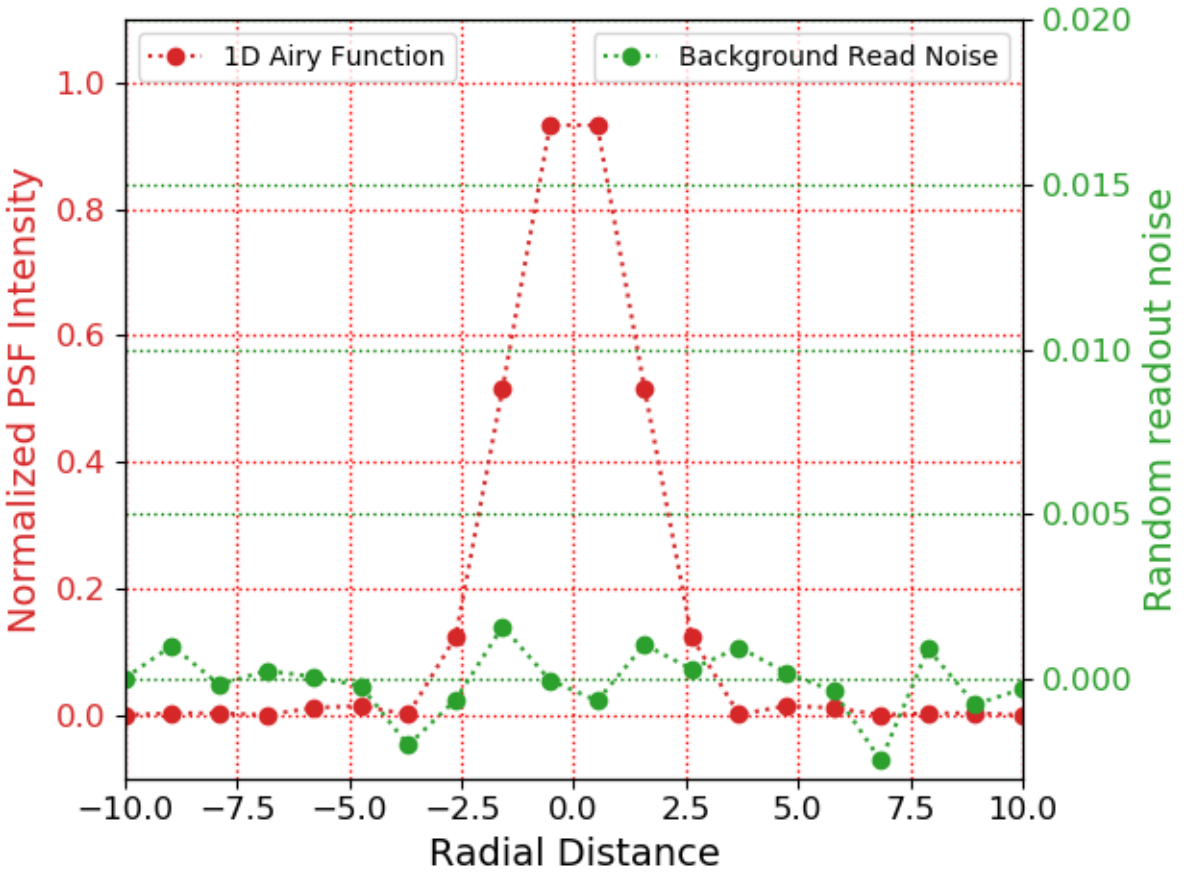

Figure 5.15 A simulated image of an Airy function having same pixel sampling as that of the CHARIS with additional background readout noise (green curve). The photometric and astrometric error associated with the background noise is calculated by measuring the relative shift and change of peak intensity of the satellite spot when a extra random background is added to the PSF.

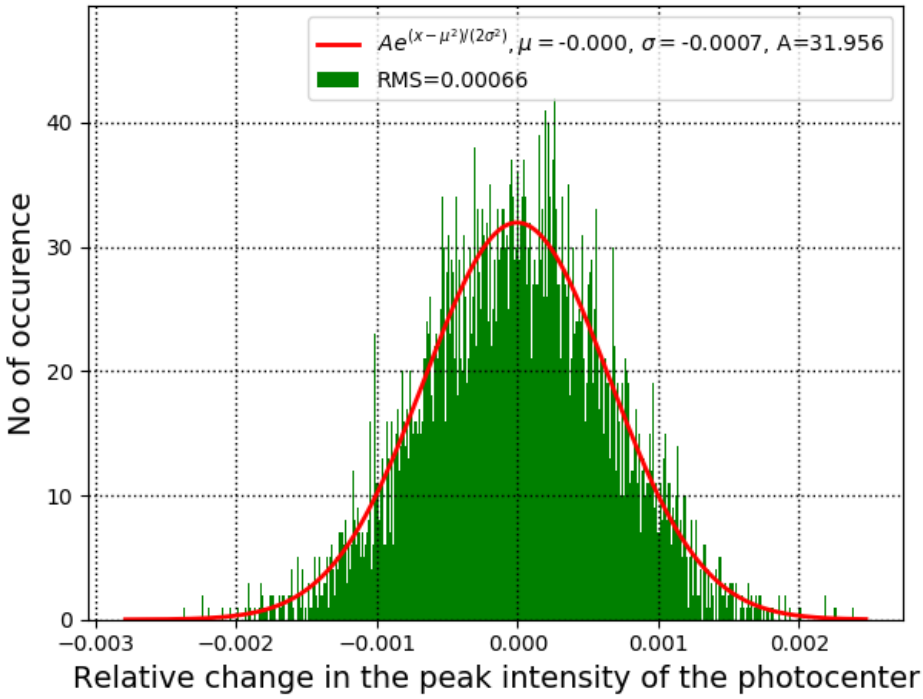

Figure 5.16 The photometric error due to background noise (dominated by detector read noise) was calculated by estimating the relative change in the peak intensity of the satellite spot's PSF when each pixel has a random error of 0.1%.

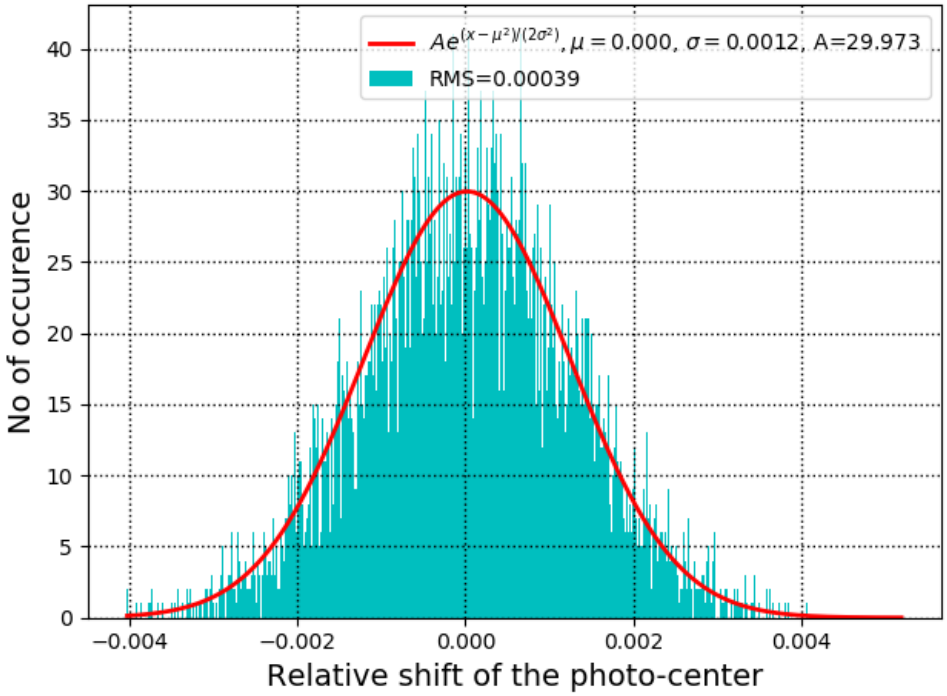

Figure 5.17 The astrometric error due to background noise (or primarily detector read noise) was calculated by estimating the relative shift in the photo-center of the peak intensity of the satellite spot's PSF when each pixel has a random error of 0.1%.

illumination. This also is done to correct vignetting, dust in the optical path. Dividing a science image with a normalized flat image will correct these static aberrations from the image. Figure 5.18's top row shows three flat images taken with CHARIS and the bottom row shows the subtracted images. I measured the pixel variations of these subtracted images. Figure 5.19 shows the mean pixel counts for each of the CHARIS monochromatic slices and Figure 5.20 shows the standard deviation of pixels in the subtracted images. I normalized the flat field images by dividing each pixels with the mean value. I then subtracted each of the normalized images. I measured the RMS pixel variation in the subtracted image. For H-band, I inferred that the width of the pixel variation is about 0.5% as shown in Figure 5.21. The standard deviation in the flat images at other wavelengths can be found in Figure 5.22.

- **Photometric Error** Two calculate the photometric error and astrometric error associated with 0.5% flat fielding error, I simulated a 1D airy function similar to that of the CHARIS's satellite spot (i.e. same sampling as that of the satellite spot where the peak constitutes of 2 data points; see Figure 5.15). I multiplied this Airy function with a set of random numbers having variance 0.5% and mean of 1. I did a Monte Carlo Simulation to generate 10^5 possible outcomes of relative change in the peak intensity due to a 0.5% random error. The histogram in Figure 5.23 shows all the possible outcomes. And the root mean square values of these outcomes is ~ 0.003. This leads to a photometric error of $0.003 * 100 = 0.3\%$.

- **Astrometric Error** To compute the astrometric error, I repeated the same Monte Carlo simulation as described in the above step and noted down the relative shift in the photo-center. The distribution of all the possible outcomes is shown in the Figure 5.24. The root mean square of this distribution is 0.004 (in units of CHARIS pixels). This corresponds to an astrometric error of $0.004 * 16.2 = 0.06$ mas. For a 2D Airy function the final astrometric error $= \sqrt{2} * 0.06 = 0.1$ mas.

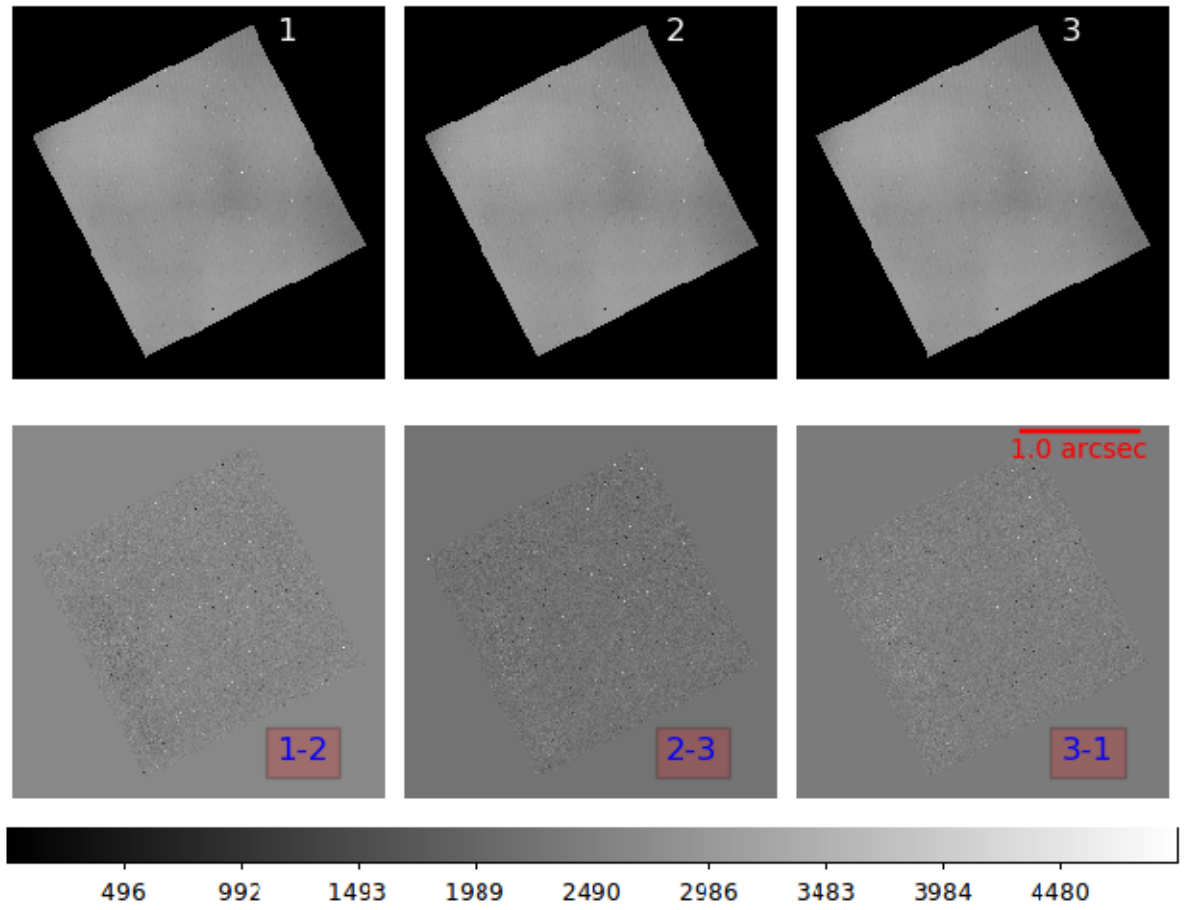

Figure 5.18 Top: Images of detector flat field with CHARIS, Bottom: Two consecutive-subtracted flat field images. The pixel variations in the subtracted flat field images is monitored to estimate the error in obtaining a single flat field image. The scale bar is for the top row.

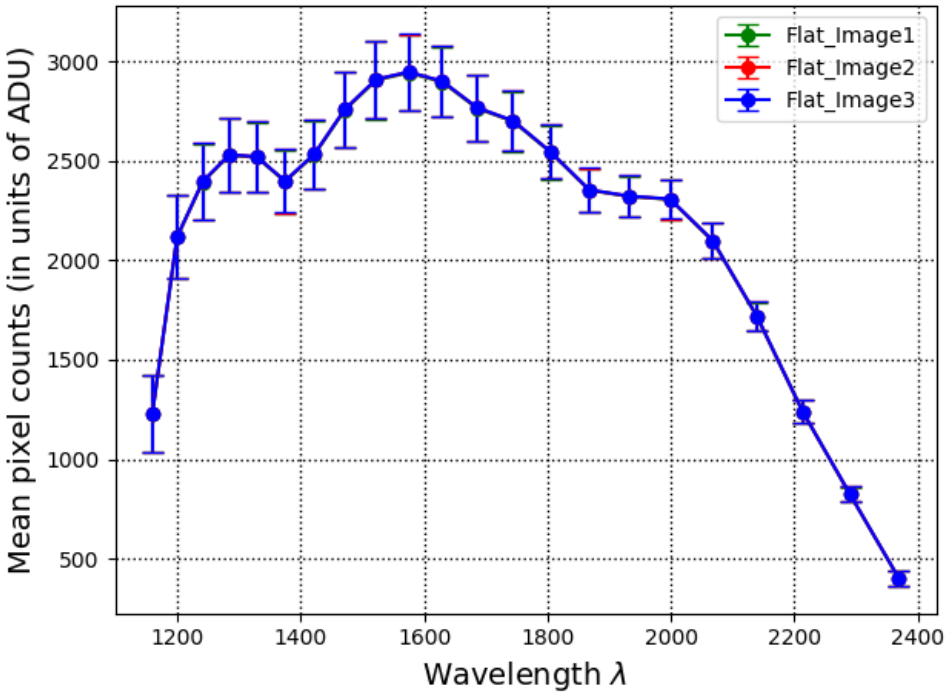

Figure 5.19 Variation of Mean Pixel Counts of Flat field images across the entire FOV with wavelength

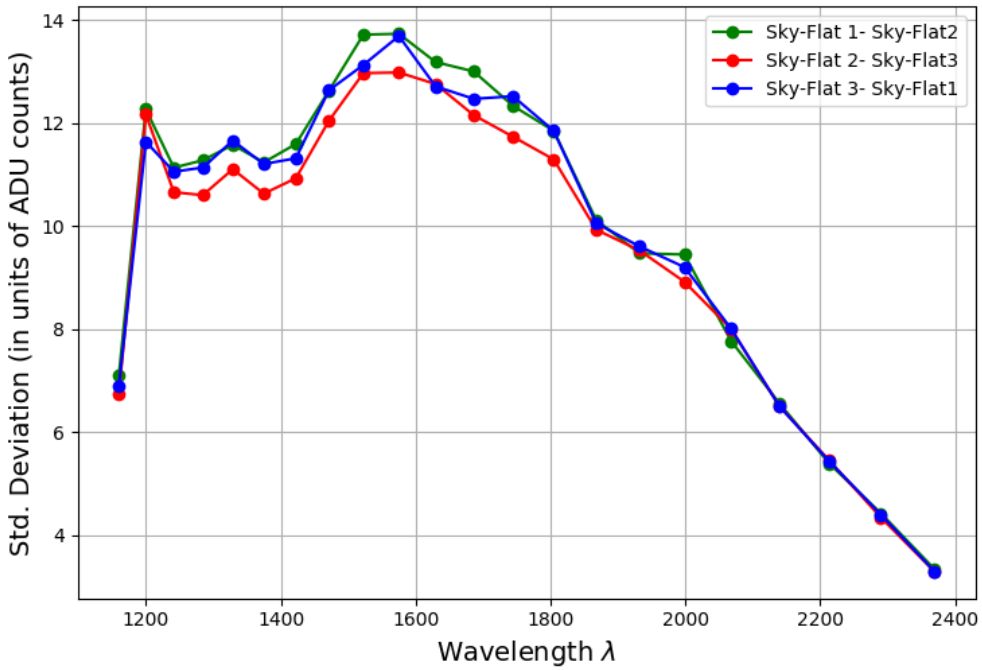

Figure 5.20 Standard deviation in the pixel counts of the subtracted flat field images(in units of ADU).

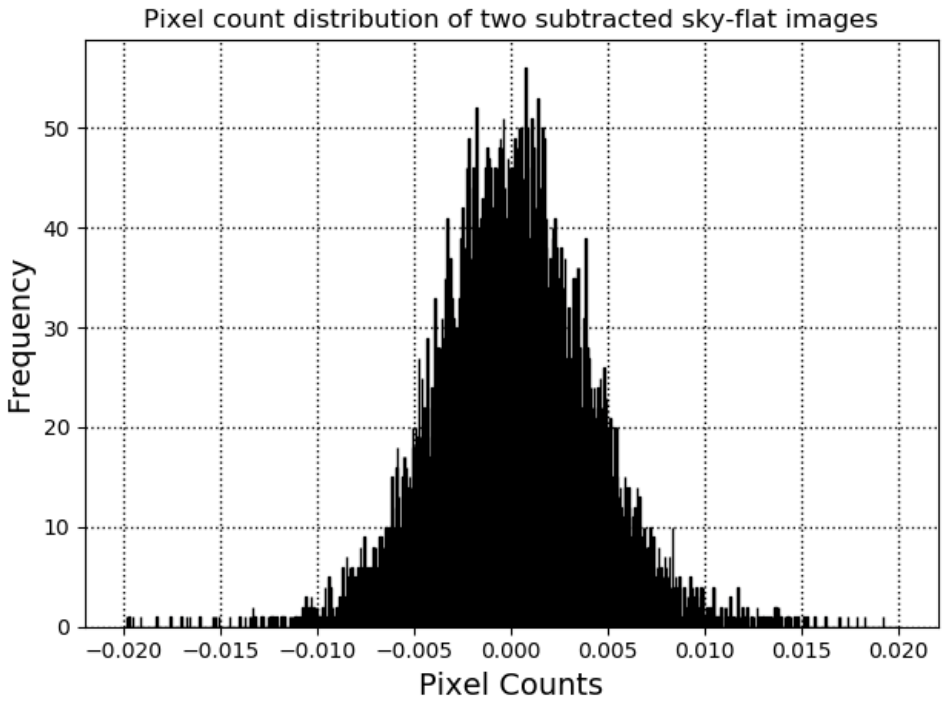

Figure 5.21 Pixel count distribution after subtracting two flat field images (in H-band).

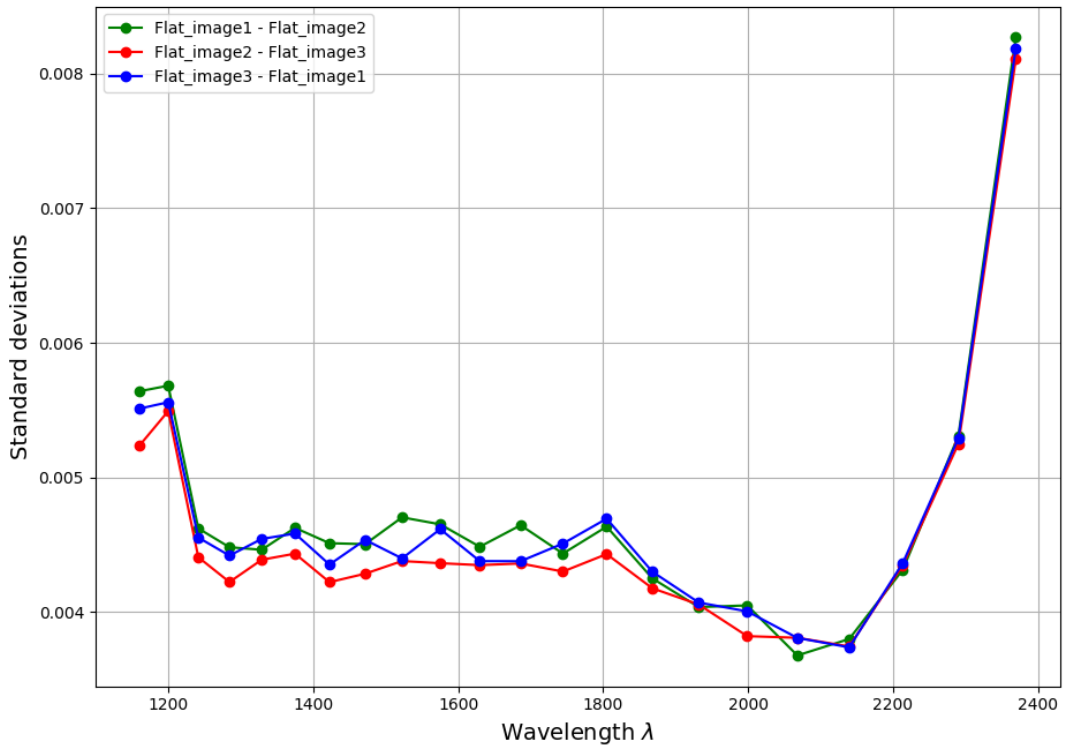

Figure 5.22 Standard deviation in the pixel counts of the subtracted normalized flat-field images

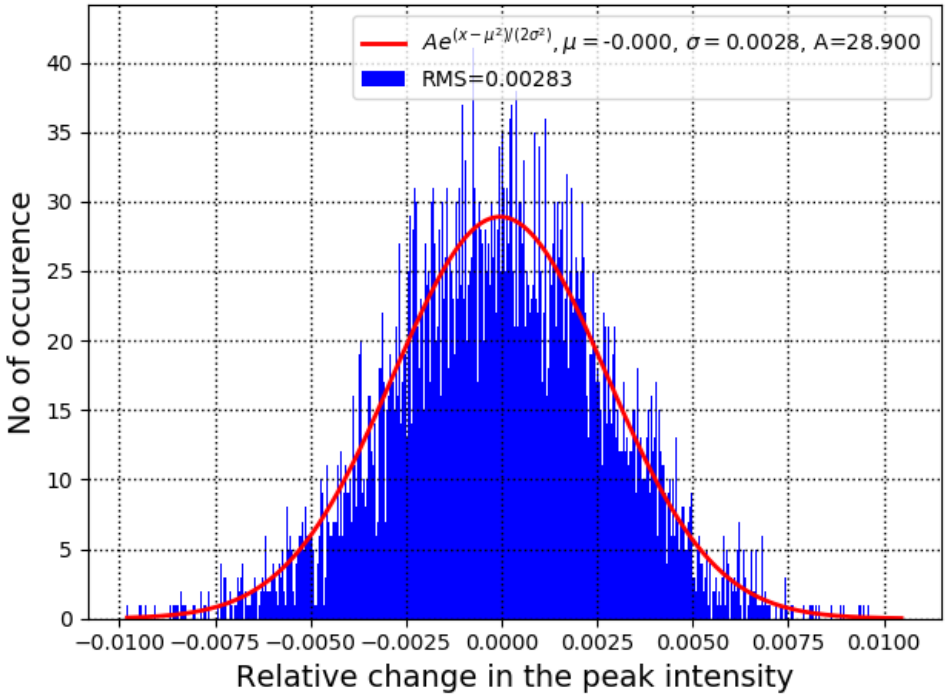

Figure 5.23 Distribution of all the possible outcomes (i.e relative change in peak-intensity) from the Monte Carlo simulation.

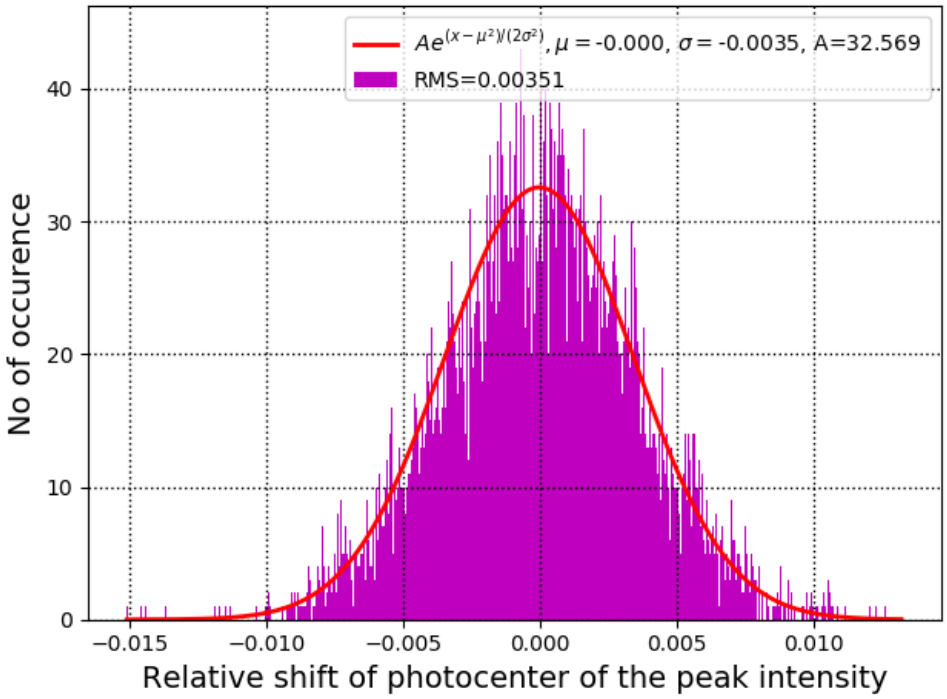

Figure 5.24 Distribution of all the possible outcomes (i.e relative shift in the photo-center of the satellite spot) from the Monte Carlo simulation.

5.4.4 Error Budget

In this section, I summarised all possible sources of error and their effect on photometry and astrometry in the form of Table 5.3.

Table 5.3 Total Photometric and Astrometric Error Budget

Physical Parameters	Photometry (%)	Astrometry (in mas)
1. Speckle Noise -Adaptive Optics -Non-common Path Aberrations	1	0.3
2. Photon Noise -Stellar Source -Background sky emission -stray light -Detector quantum efficiency	0.08	0.02
3. Background Noise **(dominated by readout noise)**	0.06	0.01
4. Flat fielding (or pixel sensitivity)	0.3	0.1

Note: This table is for one frame (HR8799, $m_H = 5.3$, satellite spot contrast = $2.5 * 10^{-3}$) with a 20.65s exposure time. With more number of frames, the error due to speckle noise, photon noise and readout noise will scales as the inverse of $\sqrt{N}$, where N is the number of frames. Whereas, the error due to flat fielding will not scale with $\frac{1}{\sqrt{N}}$, this is because I use only one flat field per observation sequence and thus the response of each of the pixel remains same during the entire observation sequence.

The total noise in the system is now:

$$\begin{aligned} \sigma_{tot} &= \sqrt{{\sigma_s}^2 + {\sigma_{phot}}^2 + {\sigma_{read}}^2 + {\sigma_{flat}}^2} \\ &\approx \sigma_s \end{aligned} \tag{5.8}$$

The total noise is therefore dominated by the speckle noise. It is of the order of 50 times stronger than the readout and photon noise. Therefore, during on-sky observation, the speckle noise dominates the total error in the system.

Effect of Strehl on Error Budget

In the case of low Strehl, the height of the maximum flux count will further decrease. This is equivalent to increase in relative intensity of the speckle noise with respect to the satellite spot , and thus increase in sine-wave amplitude for simulation as described in above paragraph. In the case Figure 5.12, I measured the contrast of 10^{-2} of halo where the PSF has already been aberrated due to the Strehl. This contrast will vary for frame to frame of the subtracted images (as Strehl will vary from frame to frame), and thus resultant astrometric error will also vary from frame to frame depending on how fast the contrast varies. The astrometric error of 0.3 mas I estimated in the above paragraph is for 1 frame. I assume this error to be closely similar for other frames too as long as the contrast of speckle halo doesn't drastically change from frame to frame. When averaged together, this error will scale down to $1/\sqrt{N}$; where N is the number of frames binned together. Similarly, readout noise and photon noise will also increase.

Chapter 6

Conclusion and Future Work

Precise photometry and astrometry is essential for characterization of companion, or debris disk nearby to the host star and also to study planetary formation theory. In post-coronagraphic images, due to lack of nearby astronomical objects accurate calibration is challenging. With the help of the SCExAO instrument, I developed and validated my photometric and astrometric calibration technique which would be quite useful in confirming companionship and characterizing exoplanets. To do this, I generated off-axis copies of the central PSF named as satellite spots which are independent (or incoherent) of the static background speckle halo and are generated by modulating the surface of the DM. These satellite spots are used measure the relative position and flux of the companion with respect to the central host. Several factors such as the atmosphere, detector background level, inaccurate phase modulation on the DM surface e.t.c. affect the stability of the satellite spots and thus can limit our photometric and astrometric precision. I demonstrated on-sky that by subtracting two images with different incoherent satellite speckle pattern, I remove the static speckle halo background from each of the satellite spot's flux measurement. For this, I wrote my own synchronization code between CHARIS data acquistion computer and SCExAO instrument's Real Time Computer (RTC). I took several sets of on-sky data with various amplitude of sine-wave ranging from 6.25nm to 50nm and also at different separations from the central PSF. I reduced all the CHARIS raw data cubes and wrote my own photometry and astrometry code to estimate flux of the satellite spot. I also tested the fast synchronization using the fast frame infrared camera; C-RED2. For this, I measured the time-offset between the between command to the deformable mirror in the SCExAO instrument and arrival of C-RED2 images in the shared memory of the RTC.

I used this offset to align the spatial switching-commands with C-RED2 exposures. I achieved 5% and 20 mas photometric and astrometric (angular separation) stability on the artificial calibrators on 10s CHARIS exposure for a duration of over 540s. Further, the measured fluxes (at a cadence of 30s) of a satellite speckle after subtraction do not show any correlated residuals suggesting that with more number of measurements we can achieve an unbiased value of flux and position. I also demonstrated that our technique is insensitive to the Strehl variation. The technique will be crucial in the regime where the satellite speckles are to be placed within the speckle halo (limited by the size of DM) and quite fainter than the central host (limited the by efficiency of the coronagraph, extreme AO corrections). It is applicable for orbits, spectra and time variation measurements from high-contrast images. I operate this synchronization command and support observers to take science data sets with my new calibration technique during a regular SCExAO observation night.

Additionally, I have taken part in the development of the REACH module in the SCExAO bench. REACH takes well AO-corrected light from SCExAO, and injects it to the IRD radial velocity instrument through single mode multi-core fibers. Some output fibers from this multi-core fiber is again sent back to the SCExAO instrument through a v-groove fiber bundle to be imaged on the C-RED2 camera. The light is then sent to the IRD instrument for spectral characterization. In the initial development of this project I characterized and measured the coupling efficiency of the V- groove fiber array through the re-imaging system. I also used the satellite spot to map field distortion for C-RED2 camera, aligning a fiber efficiently on top of a companion. I believe this would be relevant in injecting efficiently faint companion light and calibrating the high dispersion spectra. In the future, I plan to use these incoherent satellite spots along with radial velocity measurements of the host star to constrain the orbits, companion mass over a shorter baseline than previously possible. To implement this, at first, well-calibrated incoherent satellite spots are inserted in the science images with the help of DM modulation to improve astrometric measurement accuracy. Second, the radial velocity measurement of the companion light revealing its velocity along the line-of-sight, will be used to constrain the companion mass. With this technique we can achieve an astrometric precision of 10 mas and simultaneously measure radial velocity to a precision of 1m/s. This high precision technique can also be extended to determine the orbits and characterize young massive planets around M-type stars.

APPENDICES

The Astronomical Journal, 159:250 (9pp), 2020 June https://doi.org/10.3847/1538-3881/ab88cd

Precision Photometric and Astrometric Calibration Using Alternating Satellite Speckles

Ananya Sahoo[1,2], Olivier Guyon[1], Julien Lozi[1], Jeffery Chilcote[3], Nemanja Jovanovic[4], Timothy Brandt[5], Tyler Groff[6], and Frantz Martinache[7]
[1] Subaru Telescope, National Astronomical Observatory of Japan (NAOJ), 650 N Aohoku Pl, Hilo, HI 96720, USA; ananya@naoj.org
[2] Department of Astronomical Science, SOKENDAI (The Graduate University for Advance Studies), 2-21-1 Osawa, Mitaka, Tokyo 181-8588, Japan
[3] Department of Physics, University of Notre Dame, 225 Nieuwland Science Hall, Notre Dame, IN 46556, USA
[4] California Institute of Technology, 1200 East California Boulevard, Pasadena, CA 91125, USA
[5] University of California, Santa Barbara, CA 93106, USA
[6] Goddard Space Flight Center, 8800 Greenbelt Road, Greenbelt, MD 20771, USA
[7] Laboratoire Lagrange, Université Côte d'Azur, Observatoire de la Côte d'Azur, CNRS, Parc Valrose, Bât.H. FIZEAU, Nice, F-06108, France
Received 2020 January 8; revised 2020 April 8; accepted 2020 April 10; published 2020 May 6

Abstract

Photometric and astrometric calibration of high-contrast images is essential for the characterization of companions at small angular separation from their stellar host. The main challenge to performing accurate relative photometry and astrometry of high-contrast companions with respect to the host star is that the central starlight cannot be directly used as a reference, as it is either blocked by a coronagraphic mask or saturating the detector. Our approach is to add fiducial incoherent faint copies of the host star in the image plane and alternate the pattern of these copies between exposures. Subtracting two frames with different calibration patterns removes measurement bias due to static and slowly varying incoherent speckle halo components, while ensuring that calibration references are inserted on each frame. Each calibration pattern is achieved by high-speed modulation of a pupil-plane deformable mirror to ensure incoherence. We implemented the technique on-sky on the Subaru Coronagraphic Extreme Adaptive Optics instrument with speckles which were of the order of 10^3 times fainter than the central host. The achieved relative photometric and astrometric measurement precisions for 10 s exposure were respectively 5% and 20 milliarcsecond. We also demonstrate, over a 540 s measurement span, that residual photometric and astrometric errors are uncorrelated in time, indicating that residual noise averages as the inverse square root of the number of exposures in longer time-series data sets.

Unified Astronomy Thesaurus concepts: Astronomical instrumentation (799); Astrometry (80); Photometry (1234); Coronagraphic imaging (313); Astronomical techniques (1684); Direct imaging (387); Artificial satellites (68)

1. Introduction

Direct imaging of a faint companion at small angular separations from the host star is extremely difficult as the companion is obscured by the residual starlight, which forms a bright halo around the point-spread function (PSF) core. High-contrast imaging instruments such as the Gemini Planet Imager (GPI; Macintosh et al. 2014), Spectro-Polarimetric High-contrast Exoplanet REsearch (SPHERE; Beuzit et al. 2008), Magellan Adaptive Optics (MagAO; Males et al. 2018), P1640 (Hinkley et al. 2011), and the Subaru Coronagraphic Extreme Adaptive Optics (SCExAO; Jovanovic et al. 2015) have been pushing the detection limit at small angular separation (typically within 5 au for the nearest objects) from stellar hosts. These instruments share a common architecture, including one or two deformable mirrors (DM) with a large number of actuators to compensate for high-order wave front errors, wave front sensors to measure static and dynamic aberrations, coronagraphs to occult the on-axis starlight, and a highly sensitive science detector with minimal readout noise. With these existing technologies, instruments can provide high-contrast imaging capabilities delivering images and spectra of exoplanets. Accurate measurement of the exoplanet flux and position in such images is essential for orbit determination and characterization (chemical composition, mass, effective temperature). Yet, in post-coronagraphic images it becomes quite difficult to determine the relative position and intensity of a companion as the central starlight has been blocked by a coronagraph. The position of a star behind a coronagraph can be predicted using image centroid, image symmetry, and instrument feedback (Digby et al. 2006). Often astronomers measure the flux and position of the host before and after inserting the coronagraph for calibration. This leads to inaccurate measurements of the companion as the signal from the host fluctuates in time owing to variation in Strehl or background level. In addition, any drifts of the PSF behind the coronagraphic mask will be lost as well. Sivaramakrishnan & Oppenheimer (2006) address this issue by demonstrating that a regular diffractive grid placed in the pupil plane of a telescope can create a set of copies (or satellite speckles) of the host in the coronagraphic dark region to track the position of the central star behind the coronagraphic mask. This technique has been implemented in GPI to create satellite speckles for image calibration (Wang et al. 2014). The relative motion between nearby point-source and the satellites spots formed by this pupil plane grid has been used to establish companionship for Alcor b (also known as HD 116842/HIP 65477) and also constrain the properties of the companion over a shorter observation timescale than otherwise possible (Zimmerman et al. 2010). One of the limitations of this technique is that it lacks flexibility, i.e., the spatial frequency and brightness of the satellite speckles are fixed and cannot be changed without changing the pupil mask. Also there is a slight loss in total throughput before the detector as the amplitude of the pupil function is modulated. A simultaneous independent study by Marois et al. (2006) shows that a periodic phase mask or amplitude mask in the pupil plane creates off-axis copies of the primary PSF, which can be used to track the PSF position and

the Strehl ratio (SR), constraining the orbital parameters precisely (Bacchus et al. 2017; Macintosh et al. 2014). Imposing a periodic phase grid on the DM provides flexibility both in terms of controlling the speckle's intensity as well as position and also can also be used to eliminate quasi-static speckles (Martinache et al. 2014). Further, the radial elongation feature of the fiducial spots in a broadband image can be used to constrain the position of the star behind a coronagraph (Pueyo et al. 2015) and correct the residual atmospheric dispersion (Pathak et al. 2016). We have deployed this feature in the SCExAO instrument to generate artificial speckles. When created with a static DM pattern, these artificial speckles interfere with the underlying speckles from the PSF halo, warping the satellite spots, reducing the accuracy with which the PSF can be located and its brightness be determined. To address this limitation, the phase of these speckles can be rapidly (>kilohertz) switched between 0 and π within a single exposure. This effectively averages the coherently interfered speckle images in time generating a single image with temporarily incoherent calibration speckles that appear to not interfere with the underlying speckle halo. Stable, high-fidelity replicas of the PSF enable an enhanced astrometric and photometric determination of the central PSF (Jovanovic et al. 2015). Thus, modulating the phase of the grid in the pupil plane is an ideal approach for improving the precision of calibration.

Although the fast modulation ensures that calibration speckles do not interfere with the underlying PSF speckle halo, the measured intensity will be the incoherent sum of the calibration speckle flux (which we seek to measure) and the pre-existing PSF speckle halo component (which is unknown). To mitigate this measurement error, the artificial speckles could be made significantly brighter than the speckles in the halo, but doing so will divert a large fraction of starlight within or nearby the high-contrast observing region, and could also disrupt other instrument functions such as wave front sensing or short-wavelength imaging. For example, the SCExAO instrument uses a large DM amplitude (~25–50 nm) to generate satellite spots. These bright spots are still within the dynamic range of the near-infrared (NIR) integral field spectrograph (CHARIS; Groff et al. 2017), but are too bright for the visible light polarimetric imager (VAMPIRES; Norris et al. 2015), as speckle intensity is inversely proportional to the square of the wavelength (Guyon 2005). Another solution is to locate the calibration speckles in the dark part of the coronagraphic PSF halo (dark hole), allowing for their amplitude to be greatly reduced and comparable to the companion. This is critical for calibrating the flux and astrometry of faint exoplanets as the satellite speckles must be within a few orders of magnitude in brightness to avoid dynamic range issues with the detector. However fainter speckles that meet this requirement could potentially be buried under the residual starlight halo and can therefore be challenging to locate in post-coronagraphic images. So as a general point, the calibration speckle brightness is a painful trade-off between photometric and astrometric measurement accuracy and high-contrast imaging performance.

In[8] this article we present a new technique to subtract the residual starlight present under the calibration speckle. We generate a pair of incoherent fiducial copies of the host in the image plane and switch two fiducial patterns between exposures to create a set of images having alternated patterns of satellite speckles. Two images (or frames) with alternating speckle patterns are then subtracted from each other to remove the slowly varying background level and yield a bias-free measurement of the calibration speckle brightness and position. In Section 2 we give a brief overview of speckle formation and discuss the need to alternate between speckle patterns. The implementation of our approach using the SCExAO-CHARIS instrument is described in Section 3. In Section 4 we discuss some of the on-sky results obtained on the stellar target β Leo. In Section 5 we conclude the article by quantifying the on-sky precision obtained for flux and position measurement.

[8] Based on data collected at Subaru Telescope, which is operated by the National Astronomical Observatory of Japan.

2. Rationale

The principle behind speckle formation can be understood using Fourier optics, considering a pupil-plane diffraction grating. A periodic diffractive grid placed in the pupil plane generates speckles (or copies of the central host) in the focal plane. Figure 1(a) represents the sinusoidal phase modulation in the pupil plane of a telescope with a similar central obstruction and spiders as the Subaru Telescope. Figure 1(b) shows the corresponding focal plane image. Two or more diffraction spots (or speckles) can be seen in the focal plane, as in Figure 1(b), depending on the amplitude of the modulation. Each speckle has its own amplitude and phase. Interference between the artificial speckles generated by the phase modulation in the pupil and those in the PSF is governed by the addition of complex amplitude. The intensity of the artificial speckles varies proportionally with the square of the amplitude of the sine wave. The relative distance of the speckles from the PSF core scales with the sine wave's spatial frequency. Azimuthal rotation of the phase modulation about the optical axis rotates the spots in the image plane. The 1D sinusoidal phase map shown in Figure 1(a) can be used to generate a single pair of speckles (we do not consider here higher-order fainter spots). By adjusting the amplitude, phase, and orientation of the sinusoidal grid, speckles can be placed at a known location with a predefined contrast with respect to the central PSF. These spots are used in this work as the calibration yardstick to characterize the flux and position of the companion.

Sine waves can be applied as described above to generate pairs of speckles that can be used for calibration, sometimes referred to as a calibration grid. As outlined in the 1, the speckles formed by these static grids will coherently interfere with the light in the speckle halo. This will warp the satellite speckles and vary with time reducing the precision with which the astrometry and photometry of a companion can be calibrated. Therefore, more advanced dynamic speckle modulation techniques, which modulate the phase of the modulation between 0 and π at kilohertz rates, must be used to obtain temporally incoherent speckles and maximize speckle robustness. This eliminates the coherent interference between the satellite speckle and the background speckle. Jovanovic et al. (2015) have already demonstrated that there is a clear improvement of ~2–3 times in photometric as well as astrometric stability of the satellite spots when their phases are swapped at high speed within an exposure. However there still remains an incoherent underlying background (i.e., A_h^2 in Equation (4) of Jovanovic et al. 2015), which can ultimately limit the precision of calibration. This incoherent background becomes the dominant source of error for relatively faint satellite spots. Therefore we need a dynamic quantitative

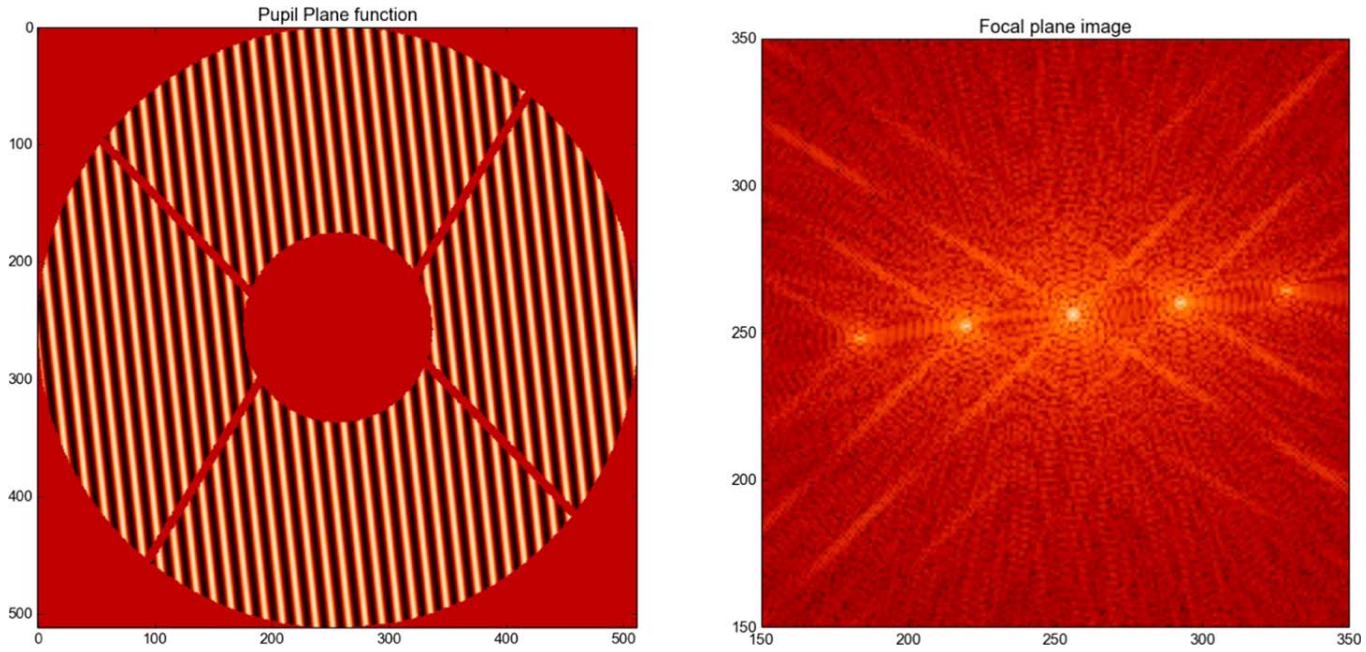

(a) Sinusoidal phase modulation in pupil plane (b) Corresponding focal plane image

Figure 1. Sinusoidal phase modulation in the pupil plane (a) generates satellite speckles in the focal plane (b).

measurement of the incoherent background so as to remove it from each frame for precise calibration. This measurement can be made by turning the speckle pattern on/off between exposures. Here we demonstrate the power of utilizing a dynamic speckle grid that creates incoherent speckles and allows for the background to be removed simultaneously. What follows is a mathematical description of this process.

The relative flux measurement between the companion and the host is the goal of photometric calibration (i.e., F_p/F_s, where F_p is the companion flux and F_s is the flux of stellar host). In post-coronagraphic images, F_p/F_s is derived from measurement of F_p/F_{ss} where F_{ss} is the measured flux of one of the satellite speckles. The grid parameters can be adjusted to provide a given contrast between the host star and the satellite speckle, i.e., $F_{ss}/F_s = c$, where c is fixed for a given sine-wave amplitude. F_p/F_s can be computed as

$$\frac{F_p}{F_s} = \frac{F_p}{F_{ss}} \times \frac{F_{ss}}{F_s} \tag{1}$$

$$= \frac{F_p}{F_{ss}} \times \frac{1}{c}. \tag{2}$$

The error in measurement of F_p/F_s is directly proportional to the error in F_p/F_{ss}. Hence one needs to measure F_p/F_{ss} precisely. The measured flux of the satellite speckle (or companion) is the sum of the flux from the actual speckle (or companion) and the incoherent background level and can be expressed as

$$\tilde{F}_{ss} = \mathrm{SR} \times F_{ss} + F_{\mathrm{bg}} \tag{3}$$

$$\tilde{F}_p = \mathrm{SR} \times F_p + F'_{\mathrm{bg}}, \tag{4}$$

where $\tilde{F}_{ss}$ and $\tilde{F}_p$ are the measured satellite speckle and companion flux respectively, F_{ss} and F_p are the actual satellite speckle and companion flux, F_{bg} and F'_{bg} are the incoherent background levels at the locations of the satellite speckle and companion respectively, and SR is the Strehl ratio. In Equations (3) and (4) we have considered incoherent artificial speckles instead of a static grid that renders coherent speckles, using the later will additionally introduce a coherent mixing term.

For slowly varying quasi-static speckles, we can eliminate F_{bg} or F'_{bg} by subtracting a frame from an adjacent frame in time where the satellite speckle and companion are absent at the position where they used to be in the previous frame. This leads to the following revised equations:

$$\tilde{F}_{ss} \approx \mathrm{SR} \times F_{ss} \tag{5}$$

$$\tilde{F}_p \approx \mathrm{SR} \times F_p. \tag{6}$$

Alternating the satellite speckles pattern (i.e., spatially modulating the speckle pattern so as to put them at a location different from the previous frame) for each exposure can give us an estimate of F_{bg} without losing calibration spots for each frame. F'_{bg} can be carefully estimated using dedicated advanced post-processing techniques such as spectral differential imaging (SDI) or angular differential imaging (ADI), which are not discussed in this paper. High-contrast imaging systems use a very narrow field of view (FOV) ($<2''$) and the SR can be assumed to be constant across the FOV neglecting off-axis and chromatic aberrations. Thus the SR can be assumed to be the same in Equations (5) and (6) to the first order. The effect of Strehl on the measured fluxes can be eliminated by dividing the two measurements as shown below.

$$\frac{\tilde{F}_p}{\tilde{F}_{ss}} = \frac{F_p}{F_{ss}} = c \times \frac{F_p}{F_s} \tag{7}$$

By using two different speckle patterns, generated by a single distinct sinusoid each, and alternating them between adjacent frames, it is possible to produce all the data needed to remove

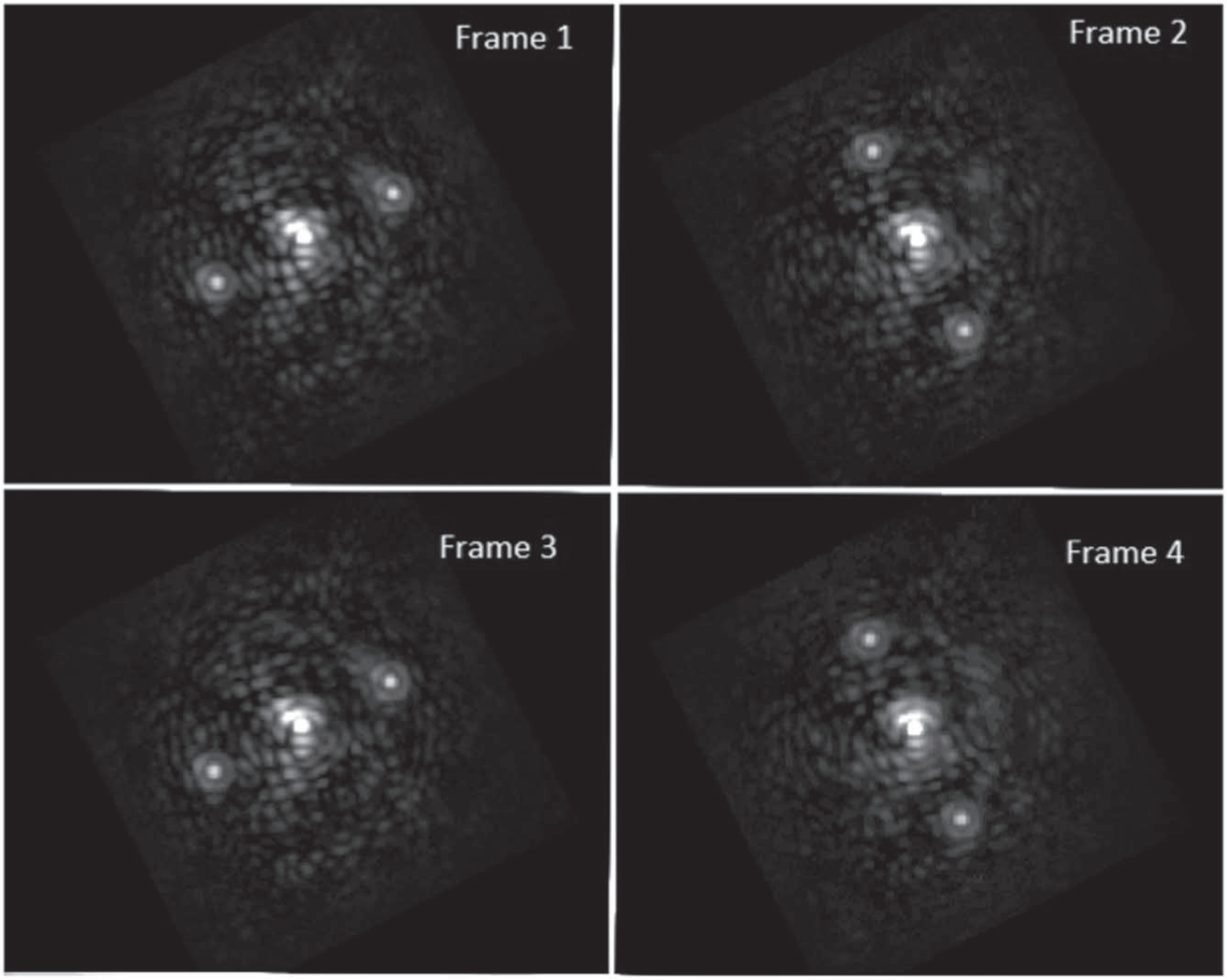

Figure 2. Images of four consecutive reduced data slices of HR8799 obtained from CHARIS at 1630 nm showing two alternate speckle patterns created by a single sine wave with an amplitude of 25 nm applied on the DM, at a separation of approximately $0\farcs46$ from the central PSF.

the effect of the background and SR and achieve a precise relative photometry and astrometry, while maintaining calibration speckles in every science frame. Further, as a sinusoid generates at least two satellite speckles (i.e., the simplest pattern of adding satellite spots to a frame), each exposure has several calibration points that can improve precision. This can of course be scaled by adding more sinusoids to a single exposure at the expense of flux in the PSF core.

3. Implementation and Test on the SCExAO-CHARIS Instrument

We tested the modulation scheme described above on-sky with SCExAO instrument to determine the improvement in the astrometric and photometric precision. To do this, a single unique sinusoidal pattern was applied to the DM in each frame and oscillated between frames. Figure 2 demonstrates the oscillating speckles that were generated for experiments from frame to frame. Each sine wave applied to the DM generates a pair of speckles. To measure photometry and astrometry precision, we considered one of the speckles to be the companion, and the second one to be the calibration speckle. The relative error in the measurement of these two spots in each frame can give us an estimate of the error associated with F_p/F_s assuming a random background level.

The SCExAO instrument is dedicated to high angular resolution imaging at small angular separation down to $\approx 1.5\lambda/D$ (where D is the diameter of the primary mirror of the Subaru Telescope). Its DM has 45 actuators across the pupil, hence satellite spots can be placed at a maximum separation of $22.5\lambda/D$ from the center. We applied a sinusoidal phase command to the DM to create speckles. In a typical observing night, we generate four bright satellite spots at a separation of $15.9\lambda/D$ from the central PSF by giving two orthogonal sinusoidal phase commands to the DM. The amplitude of the sine wave on the DM is set to be $\sim$25 nm or $\sim$50 nm. However, in order to demonstrate our new approach we generated fainter incoherent satellite speckles with brightness similar to the background speckles. Therefore, we used a sine wave of amplitude 8.8 nm (i.e., $25/\sqrt{8}$) on the DM to generate speckles of a brightness eight times lower than the regular 25 nm amplitude.

On-sky data was taken on the target β Leo on the engineering night of 2019 January 12, 14:21–14:30 (UTC) with CHARIS. The average atmospheric seeing was approximately 0.3 arcsec during this period. CHARIS is an integral field spectrograph imaging the post-coronagraphic light

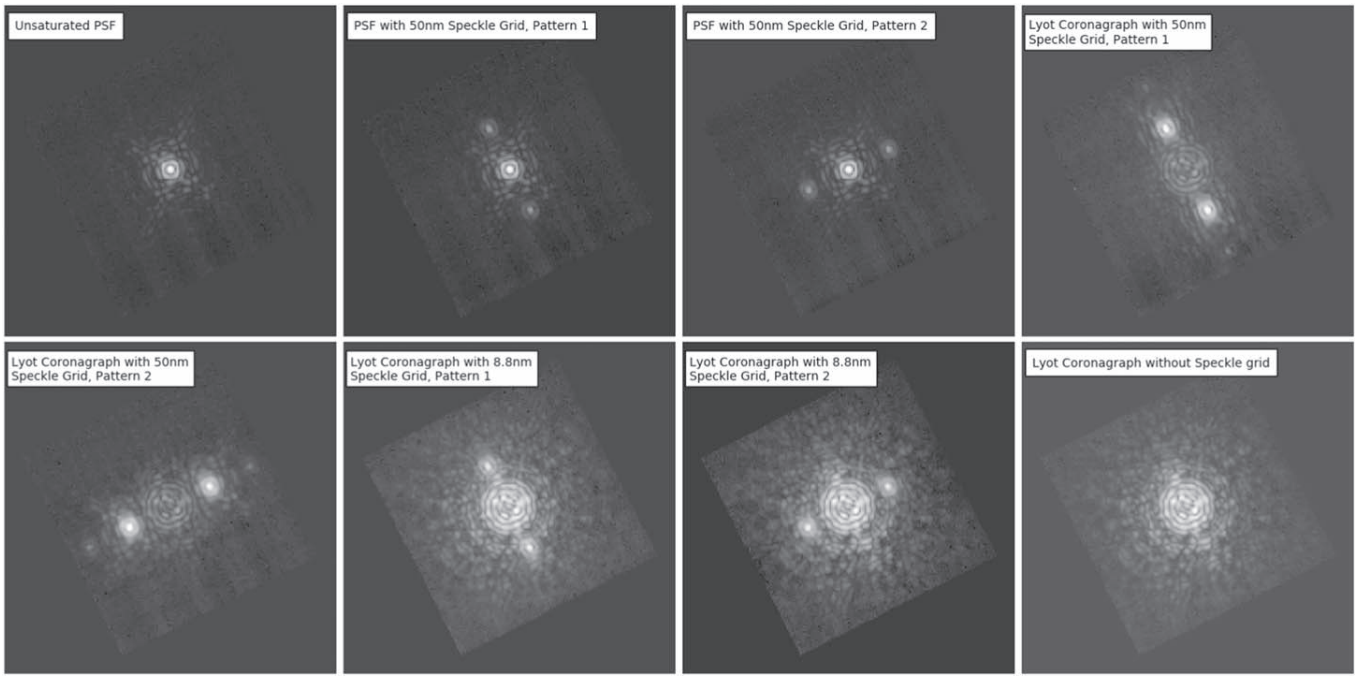

Figure 3. Classical set of ladder frames taken using the laboratory source to compute the absolute contrast between the PSF core and satellite speckles of an 8.8 nm DM amplitude.

provided by SCExAO over a $2'' \times 2''$ FOV. The CHARIS pixel size is 16.2 mas. CHARIS operates in the NIR wavelength region, from the *J* band to the *K* band (1160 nm to 2370 nm). The low spectral resolution mode has a resolving power ($\Delta\lambda/\lambda$) of 18.4 which covers the *J* band to the *K* band in a single shot and was used for these observations. Each CHARIS raw exposure produces a 3D data cube of 22 wavelength slices, each slide being a monochromatic 2D spatial image.

The central star was blocked by a Lyot coronagraph with an inner working angle of 113 milliarcsecond. The switching of the speckle pattern (spatial modulation) was synchronized to the CHARIS data acquisition. The exposure time of CHARIS was set to 10 s. The speckle pattern was switched between exposures, i.e., every 10 s. The phase of the sine wave on the DM during each exposure was varied (phase modulation) between 0 and π each 500 μs. SCExAO's extreme AO loop typically runs at a 2 $\sim$ kHz frame rate, hence the wave front sensor in SCExAO can detect this phase modulation. However, the typical loop gain is $\sim$0.3, so it has a much slower response time ($\sim$200 Hz), so the fast sinusoidal phase modulation applied on the DM was uncorrected by the extreme AO loop.

The absolute contrast between the 8.8 nm speckle grid and the central PSF was measured using a laboratory super-continuum laser source stimulating the central star. CHARIS lacks a sufficient dynamic range to calibrate the contrast between the satellite speckles generated by an 8.8 nm amplitude and the central PSF. Therefore, a speckle grid of higher DM amplitude (50 nm) was used to register the relative flux between the PSF core and the 50 nm non-coronagraphic satellite speckles at first, and then the relative flux between the 50 and 8.8 nm satellite spots was computed by inserting a focal plane mask and increasing the exposure time. The spots generated by the 8.8 nm amplitude were expected to be 32 times fainter than the 50 nm amplitude. We obtained a set of eight images as presented in Figure 3 for one wavelength for absolute contrast calibration using the super-continuum laser source. This set consists of an unsaturated image of the central PSF (top left), the central PSF with the 50 nm speckles for two different speckle patterns (top middle), the 50 nm speckle grid with the Lyot coronagraph for the two patterns (top right and bottom left), the 8.8 nm speckles with the Lyot coronagraph for the two patterns (bottom middle), and an exposure with the Lyot coronagraph and no additional speckles (bottom right). We address this set of images as "ladder frames" as we acquired them in steps of decreasing order of the DM amplitude. The relative flux and position of the central PSF and the 50 nm speckle grid without any coronagraph was measured at first, and then we measured the flux and position between the 50 nm and the 8.8 nm speckle grids with the Lyot coronagraph. Using these measurements we computed the relative flux and position between the central source and the 8.8 nm speckle. The exposure with the Lyot coronagraph without any satellite speckles applied is used to subtract the background speckle halo in the coronagraphic images. Figure 4 shows the measured contrast variation of the 50 nm and 8.8 nm speckle grids as a function of wavelength. The flux ratio between the 50 nm and 8.8 nm speckle grids was measured to be $\sim$29. The flux ratio between the central PSF and the 8.8 nm grid at 1630 nm was measured to be $\sim 1.6 \times 10^{-3}$. The flux ratio, as shown in Figure 4, is used later on to scale the average pixel counts obtained for a satellite speckle with the contrast value at a particular wavelength.

4. On-sky Results

In this section we discuss results obtained on-sky on the target β Leo (A3 star type, $H_{\rm mag} = 1.92$). The raw data were reduced using the CHARIS data reduction pipeline (Brandt et al. 2017). The level of the background speckles is much higher on-sky than in the laboratory due to the residual

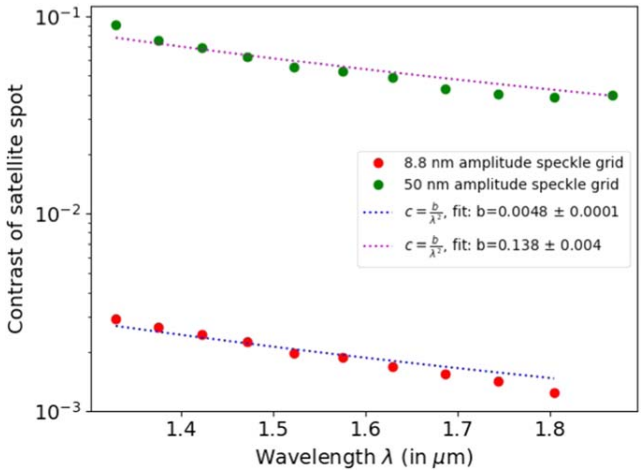

Figure 4. Variation of the contrast of the 50 nm and the 8.8 nm speckle grids as functions of wavelength.

atmospheric wave front errors. Hence, 8.8 nm speckle spots that are clearly visible with the laboratory source are barely visible in on-sky reduced data cubes as shown in Figure 5(a). However, after subtracting two consecutive frames they can be easily located as seen in Figure 5(b). Each frame has a set of two speckles as shown in Figure 2. The relative flux and position of each speckle was measured by fitting the image of the satellite speckle to an analytical Airy disk function using a least-square fitting method. The maximum flux count, coordinates of the pixel with maximum flux, and the average flux in an annulus surrounding the image (to estimate the background offset under the fitted function) were given as initial conditions to estimate the PSF. From the fitting, we obtained the amplitude and center of the fitted function to compute the flux ratio and position coordinates of the satellite speckle with respect to the PSF core.

For convenience, let the top right speckle in the left-hand panel of Figure 5(b) be I_1 and the bottom left speckle on the same image be I_2. Figures 6(a) and (b) show the measured flux variation of I_1 without and with subtraction over a duration of 540 s at three different NIR wavelengths (J, H, and K band) with a cadence of approximately every 30 s. The exposure time for each frame was kept at 10.32 s. Figure 6(a) shows changes in the flux of I_1, possibly due to variations in the SR and background. The standard deviation in the flux measurement improves after subtraction thanks to proper background subtraction, as shown in Figure 6(b). Results are summarized in the Table 1.

Figure 7 shows the variation of the separation between I_1 and I_2 with time before and after subtraction. After subtraction, the astrometric precision significantly improves from ∼50 milli-arcsecond(mas) to ∼20 mas in the J band and slightly improves from ∼23 mas to ∼20 mas in the H band. However, in the K band, due to a low signal-to-noise ratio of the satellite speckle, we did not see any improvements. These results are summarized in Table 1.

Using two alternating speckle patterns, we estimate the relative error associated with the measurement of the flux ratio between the companion and the central star. For this, we consider one of the speckle spots (i.e., I_1) to be the companion and the other spot to be the calibrator (i.e., I_2). Equation (7) shows that the relative error (i.e., σ) in the measurement of the ratio of intensities of I_1 and I_2 is equal to error in the measurement of the companion and the central star flux. Figures 8(a) and (b) show the flux ratio between speckles I_1 and I_2 before and after subtraction respectively. The standard deviations in measurement improve by subtracting two frames from each other for the J and H bands. $\frac{I_1}{I_2}$ in Figure 8(a) for the J and H bands is always less than unity, suggesting that there is a bias in the measurement of $\frac{I_1}{I_2}$ without subtraction. Whereas, in Figure 8(b), we subtracted the underlying background sitting beneath the satellite speckle by taking two exposures with different satellite speckle patterns and measured the intensities of the clearly visible satellite spots. When we subtract two consecutive images, the common static background disappears, and the ratio is closer to unity. Since we expect the ratio between two satellite speckles to be constant over time, this indicates that even between consecutive images, the background changes by about 3.7% (H band). Assuming this background level to be random, we expect that the relative flux between the companion and central PSF can be measured to a precision of 3.7% (in the H band) using Equation (7) for a 10 s frame exposure.

We binned N (where N is a positive integer) frames together and measured the relative flux ($\frac{I_1}{I_2}$) and separation ($|\boldsymbol{I}_1 - \boldsymbol{I}_2|$) of the resultant pair of speckle spots in each binned frame. We then computed the standard deviation (σ) in the measured

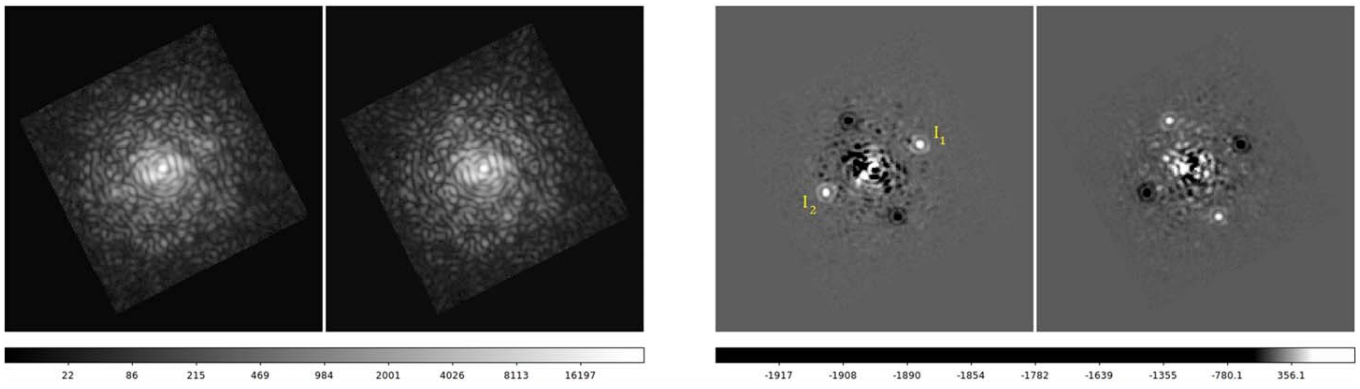

(a) Before Subtraction (b) After Subtraction

Figure 5. (a) Images of two consecutive reduced data slices of β Leo before subtraction obtained from CHARIS at 1744 nm with two alternate fainter speckle patterns where they are barely visible. (b) Images of the same data slices of β Leo after subtracting the frames from each other where the calibration speckles can be clearly seen.

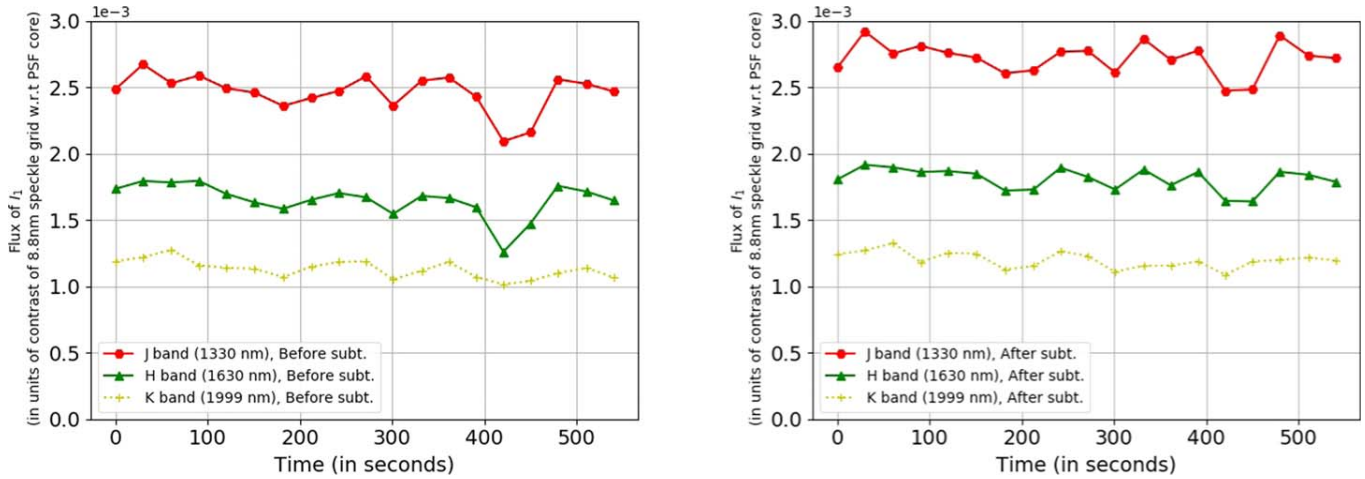

(a) Before Subtraction (b) After Subtraction

Figure 6. Flux variation of one of the speckles before (left panel) and after (right panel) subtraction. Flux is expressed in units of contrast based on static calibration from the previous Figure 4.

Table 1
Photometric and Astrometric Precision Obtained (for 10 s Frame Exposure)

Wavelength (in nm)	Photometry (I_1) % Standard Deviation σ	Astrometry $\lvert \boldsymbol{I}_1 - \boldsymbol{I}_2 \rvert$ Angular Separation (in mas)	Ratio ($\frac{I_1}{I_2}$) % Standard Deviation σ
Before Subtraction			
1330	5.8	51	3.5
1630	7.7	23	5.2
1999	6.0	45	5.1
After Subtraction			
1330	4.5	20	2.8
1630	4.6	20	3.7
1999	5.0	47	6.4

relative fluxes and distances for each of the N-binned sets. Figure 9 shows the variation of the standard deviation (σ) between the measurements (before and after subtraction) with different binning numbers. In Figure 9(a), the standard deviation without subtraction (blue curve) does not converge with an increase in N, suggesting that with an increase in the number of exposures, the precision of the measurement may not improve. However, for subtracted frames (red curve) we observe that σ decreases with N in a way that is consistent with $1/\sqrt{N}$. This indicates that subtracting two consecutive frames has removed the biased incoherent speckle halo from $\frac{I_1}{I_2}$ measurements to a significant extent. Therefore, with an increase in the number data points, we expect the residual uncorrelated noise to become further negligible and obtain an unbiased precise flux measurement. Figure 9 shows a comparison of precision obtained using the regular incoherent speckle grid where we do not change the spatial pattern (blue curve) and the precision obtained by our new technique of alternating the speckle pattern (red curve). From the figure there is a clear improvement in photometric as well as astrometric precision during the same interval of time and under the same environmental conditions. For an 80 s frame exposure we can measure the relative flux between the companion and host to a precision of 1% as well as the position to a precision of $\leqslant$5 mas in the H band. Extrapolating

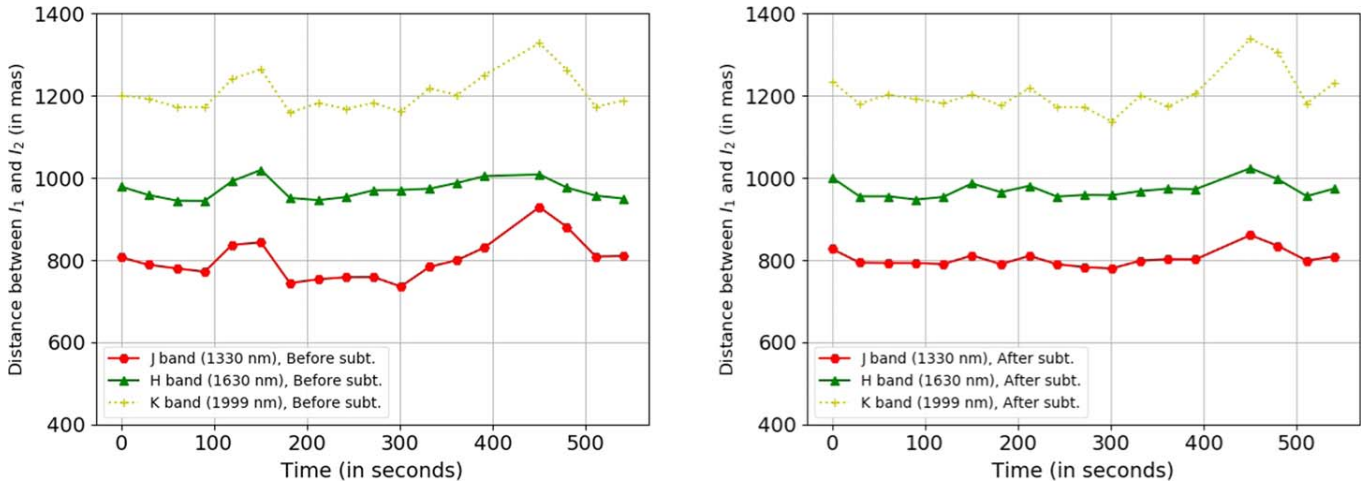

(a) Before Subtraction (b) After Subtraction

Figure 7. Distance variation between I_1 and I_2 with time before and after subtraction.

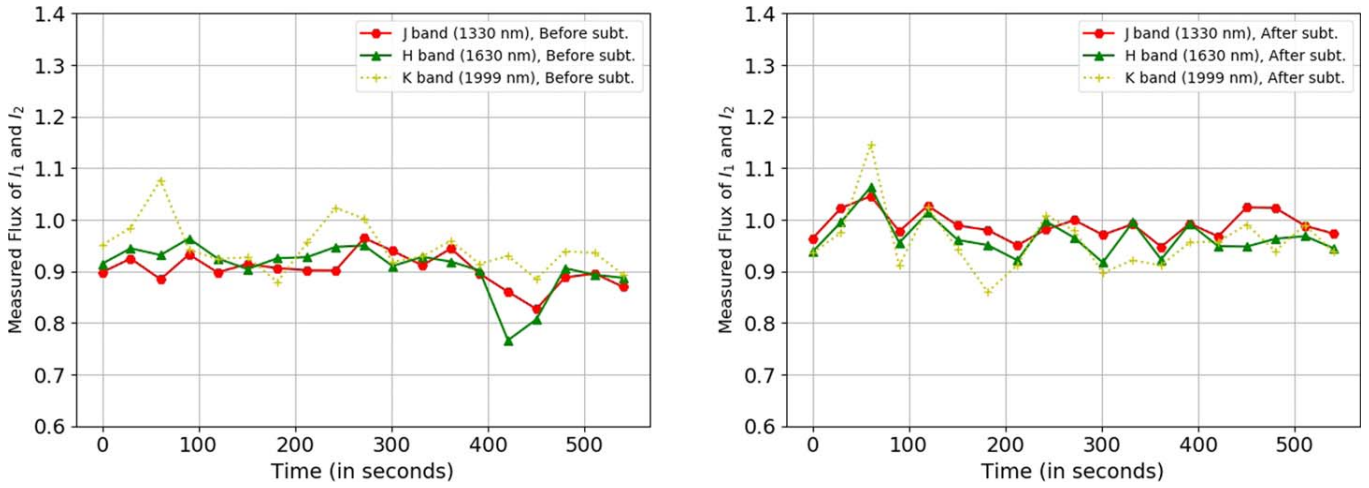

(a) Before Subtraction (b) After Subtraction

Figure 8. Ratio of intensity variation of a pair of speckle before and after subtraction.

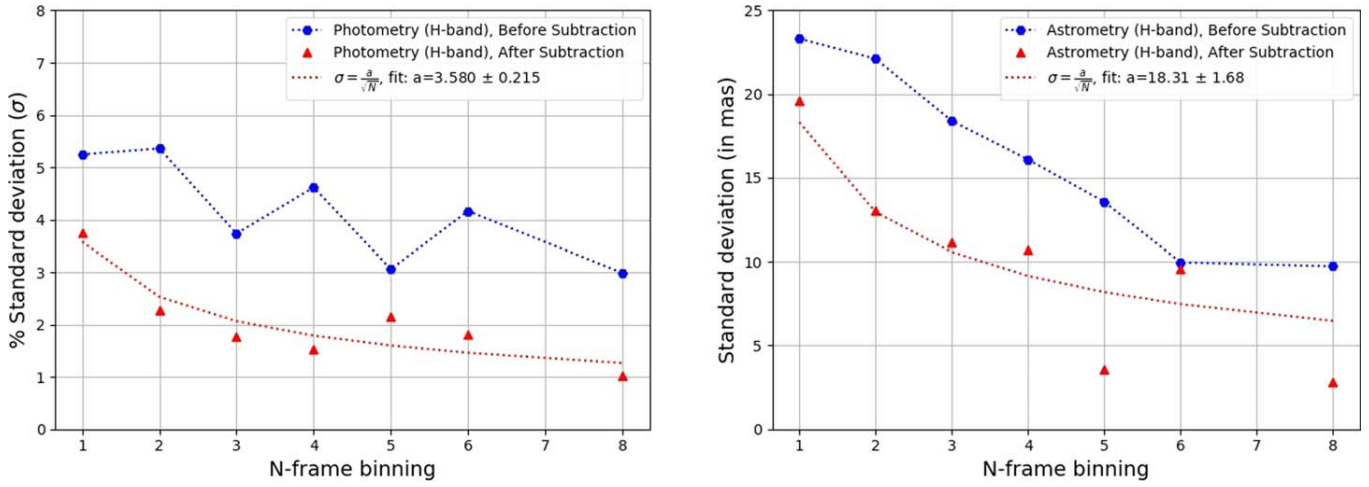

(a) Photometry (b) Astrometry

Figure 9. Photometric and astrometric precision with different binning numbers. (a) Photometry: variation of standard deviation in the measurement $\frac{I_1}{I_2}$ with different binning numbers. (b) Astrometry: variation of standard deviation in the measurement of $|\boldsymbol{I}_1 - \boldsymbol{I}_2|$ with different binning numbers.

the fitting parameters from Figure 9 to a total integration time of 1912 s, assuming similar environmental conditions, we arrive at a astrometric precision of 1.3 mas ,which is ∼2–3 times better than what has been achieved to confirm the companionship of Alcor in Zimmerman et al. (2010). The total integration time for our experiment was ∼540 s. More on-sky data is needed to perform a meaningful quantitative comparison of our technique with the previously used techniques. This will be the goal of an upcoming publication.

5. Conclusion

In this article we discuss the importance of satellite spots in post-coronagraphic images and the need to change their patterns for each exposure. This article provides a new approach to simultaneous photometric and astrometric calibration in the visible and NIR region using fainter satellite spots. This would be relevant to instruments such as MagAO-X (with VisAO (visible) and Clio2 (infrared) as science cameras) and SCExAO (with VAMPIRES (visible) and CHARIS (infrared) as science cameras). We considered the simplest case to demonstrate our alternating scheme, i.e., 1 kHz phase swapped sine waves in two alternating directions. The single sine-wave pair of speckles imaged on each exposure is sufficient for photometric and 2D astrometric referencing, as the star lies in the center of the line joining the spots. We deployed artificial incoherent satellite spots with alternating patterns on a high-resolution integral field spectrograph to do precision photometry and astrometry. We quantitatively demonstrated that relative flux measurements between the companion and host are insensitive to Strehl. Using this technique we determined that the relative flux between the companion and the host can be measured to an accuracy of 3.7% (for a 10 s frame exposure) in the regime where the satellite speckles and PSF halo are of similar brightness (both at $\sim 10^{-3}$ contrast ratio). A photometric precision of $<1\%$ and astrometric precision of <5 mas is achieved with eight-frame binning (80 s frame exposure). Using more satellite spots in a frame should improve the precision by a factor of $\sqrt{n}$, where n is the number of sine waves. However, adding more satellite spots will diffract more

light from the central host, which may limit the performance of the extreme AO loop. We demonstrated a practical solution to photometric and astrometric calibrations, which are challenging in high-contrast imaging. This technique is applicable for orbits, spectra, and time variation measurements from high-contrast images.

The authors acknowledge the support from Subaru Telescope, NAOJ for lending out their facility. The development of SCExAO was supported by the Japan Society for the Promotion of Science (grant-in-aid for research No. 23340051, 26220704, 23103002, 19H00703, and 19H00695), the Astrobiology Center of the National Institutes of Natural Sciences, Japan, the Mt. Cuba Foundation, and the director's contingency fund at Subaru Telescope. The work of F.M. is supported by the ERC award CoG-683029. The authors wish to recognize the very significant cultural role and reverence that the summit of Maunakea has always had within the indigenous Hawaiian community. We are most fortunate to have the opportunity to conduct observations from this mountain.

ORCID iDs

Ananya Sahoo https://orcid.org/0000-0003-2806-1254
Olivier Guyon https://orcid.org/0000-0002-1097-9908
Julien Lozi https://orcid.org/0000-0002-3047-1845
Jeffery Chilcote https://orcid.org/0000-0001-6305-7272
Nemanja Jovanovic https://orcid.org/0000-0001-5213-6207
Timothy Brandt https://orcid.org/0000-0003-2630-8073
Tyler Groff https://orcid.org/0000-0001-5978-3247
Frantz Martinache https://orcid.org/0000-0003-1180-4138

References

Bacchus, E., Parry, I. R., Oppenheimer, B. R., et al. 2017, MNRAS, 469, 4796
Beuzit, J. L., Feldt, M., Dohlen, K., et al. 2008, Proc. SPIE, 7014, 701418
Brandt, T. D., Rizzo, M., Groff, T., et al. 2017, JATIS, 3, 048002
Digby, A. P., Hinkley, S., Oppenheimer, B. R., et al. 2006, ApJ, 650, 484
Groff, T., Chilcote, J., Brandt, T. D., et al. 2017, Proc. SPIE, 10400, 1040016
Guyon, O. 2005, ApJ, 629, 592
Hinkley, S., Oppenheimer, B. R., Zimmerman, N., et al. 2011, PASP, 123, 74
Jovanovic, N., Guyon, O., Martinache, F., et al. 2015, ApJL, 813, L24
Jovanovic, N., Martinache, F., Guyon, O., et al. 2015, PASP, 127, 890
Macintosh, B., Graham, J. R., Ingraham, P., et al. 2014, PNAS, 111, 12661
Males, J. R., Close, L. M., Miller, K., et al. 2018, Proc. SPIE, 10703, 1070309
Marois, C., Lafreniere, D., Macintosh, B., et al. 2006, ApJ, 647, 612
Martinache, F., Guyon, O., Jovanovic, N., et al. 2014, PASP, 126, 565
Norris, B., Schworer, G., Tuthill, P., et al. 2015, MNRAS, 447, 2894
Pathak, P., Guyon, O., Jovanovic, N., et al. 2016, PASP, 128, 124404
Pueyo, L., Soummer, R., Hoffman, J., et al. 2015, ApJ, 803, 31
Sivaramakrishnan, A., & Oppenheimer, B. R. 2006, ApJ, 647, 620
Wang, J. J., Rajan, A., Graham, J. R., et al. 2014, Proc. SPIE, 9147, 914755
Zimmerman, N., Oppenheimer, B. R., Hinkley, S., et al. 2010, ApJ, 709, 733

Precision Photometric Calibration with Alternating Incoherent Satellite Speckles

Ananya Sahoo[a,b], Olivier Guyon[a], Julien Lozi[a], Jeffery Chilcote[c], Timothy Brandt[d], Nemanja Jovanovic[e], Tyler Groff[f], Frantz Martinache[g], Sebastien Vievard[a], Yosuke Minowa[a]

[a]Subaru Telescope, National Astronomical Observatory of Japan(NAOJ), 650 N Aohoku Pl, Hilo, Hawaii, 96720, U.S.A, [b]Department of Astronomical Science, SOKENDAI (The Graduate University for Advance Studies), 2-21-1 Osawa, Mitaka, Tokyo 181-8588, Japan, [c]Department of Physics, University of Notre Dame, 225 Nieuwland Science Hall, Notre Dame, IN 46556, [d] University of California, Santa Barbara,California 93106, [e]California Institute of Technology, 1200 East California Boulevard Pasadena, California 91125, [f]Goddard Space Flight Center, 8800 Greenbelt Rd, Greenbelt, MD 20771, U.S.A, [g]Laboratoire Lagrange, Université Côte d'Azur, Observatoire de la Côte d'Azur, CNRS, Parc Valrose, Bât. H. FIZEAU, 06108 Nice, France

ABSTRACT

Exoplanet characterization relies on extracting precision astrometry (orbits) and photometry (spectra, time variation) measurements from high contrast images. Obtaining such measurements is challenging due to residual starlight speckles and the fact that the central stellar PSF core is blocked by the coronagraph. In post coronagraphic images it becomes quite difficult to measure the relative position and intensity of companion with respect to the stellar as it is blocked by the coronagraph. This issue has been addressed by imposing a periodic phase grid on the Deformable Mirror of SCExAO system to generate satellite speckles which are incoherent with underlying speckle halo for calibration. We report on-sky measurements of the photometric stability of such incoherent speckles over a 15 minute period time. We demonstrate that for relatively fainter speckles, unknown background noise (speckles) creates a bias in the photometric measurement. We show that, by subtracting two frames with two different speckle patterns, we address this issue and obtain unbiased measurements. This technique will be beneficial for future large telescopes where they have the potential to obtain diffraction limited images.

Keywords: Photometry, Satellite Speckles, High Contrast Imaging, Coronagraphy, Instrumentation, Adaptive Optics

1. INTRODUCTION

Direct imaging of nearby faint companion, circumstellar disk gives an insight to the planet formation theory, characterization and allows astronomers to look for life beyond our solar system. Several high contrast imaging instruments such as Gemini Planet Imager (GPI)[1], Spectro-Polarimetric High-contrast Exoplanet REsearch instrument (SPHERE)[2], Magellan Adaptive Optics (MagAO)[3] and Subaru Coronagraphic Extreme Adaptive Optics (SCExAO)[4] are evolving to produce high resolution direct images of these objects at small angular separation from their stellar host. Relative accurate photometry plays a key role in determining the physical properties of the companion such as temperature, mass, spectra (chemical composition). In non-coronagraphic images, relative photometry(or astrometry) is easily obtained by simultaneously comparing the flux(or position) of the targeted object with their stellar host's Point Spread Function(PSF) in the same exposure. Whereas, in coranagraphic images, the central starlight is blocked by an occulter or mask and it becomes quite challenging to perform relative photometry or astrometry in these images. This issue has been addressed by placing a regular diffractive grid in the pupil plane to create a set of off-axis symmetric copies (or satellite spots) of the central PSF which are then used as calibrators for the nearby objects[5]. The off-axis copies thus formed may interfere

Further author information: (Send correspondence to A. Sahoo)
A. Sahoo: E-mail: ananya@naoj.org

with the background speckles to form spots which are not exact replicas of the central PSF. The phase of these calibrators are switched between 0 and π at high speed (typically $\sim$kHz)[6], time averaged within an exposure to get temporarily incoherent copies of the central PSF. However, there still remains incoherent flux beneath the satellite speckle which can ultimately limit our calibration. In subsequent sections in this article, we propose and demonstrate that by subtracting two closet frames with two different speckle patterns, we can achieve a much more precise photometric calibration with these satellite speckles.

2. SATELLITE SPOT FORMATION

The physics behind the formation of satellite spot is based on Huygens-Fresnel propagation principle after diffraction grating. Adding a periodic grid phase mask or amplitude mask in the pupil plane creates a pair or more off-axis symmetric copies of the central PSF. Each spot thus formed has its own phase and amplitude. These spots can be placed at a known location with a pre-defined contrast w.r.t PSF core by adjusting the grid parameters such as spatial grid frequency, amplitude of aberration etc. In the left of figure 1, a sinusoidal 1-D wave has been applied to the pupil plane phase function (similar to Subaru Telescope's pupil) and the right shows the corresponding focal plane image thus generated. Two or more satellite spots can be seen the right of figure 1. As the light from the central PSF is diffracted away to generate the satellite spots, these spots thus have low resolution spectra of the central star and can be used to track the obscured PSF core.

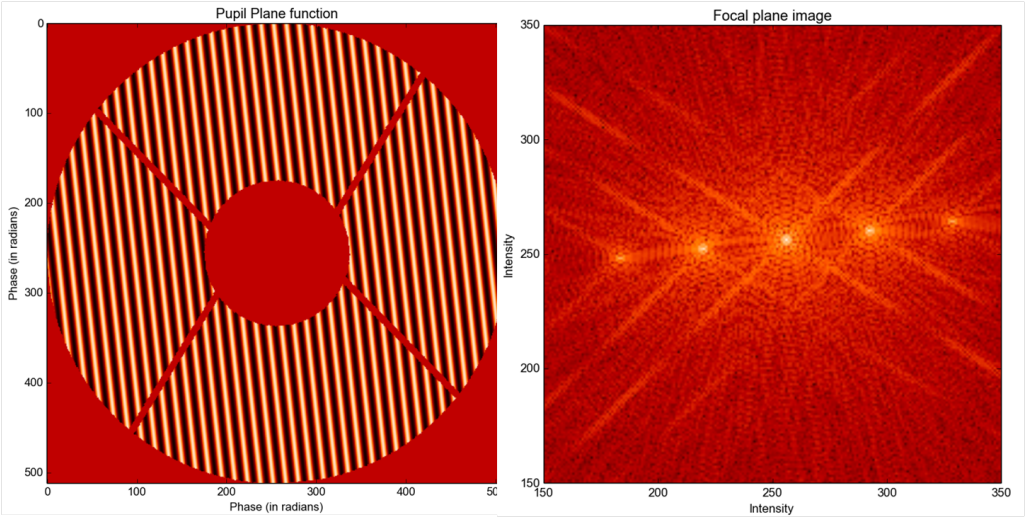

Figure 1. Sinusoidal phase modulation in the pupil plane creates monochromatic satellite spots in the focal plane

In post-coronagraphic images, the relative flux between the central PSF and the companion is registered through the satellite spot. At first, the relative flux between the satellite spot and the companion is measured and then this ratio is scaled with the pre-determined contrast of satellite spot and PSF core to compute the relative flux of the companion and the central star. Accurate measurement of the relative flux between satellite spot and the companion is the key to precise photometry. For ground based telescopes, several factors such as the object air mass, the telescope vibration, seeing, sky transmission lead to Strehl variation, thus introduce aberration in the flux measurement. The effect of Strehl variation on the satellite spot and the companion is uniform (neglecting chromatic and off-axis aberration). Therefore, relative flux measurement eliminates the strehl variation (neglecting the quasi-static background level). Other factors such as aberration in the instrument optics, non-common path adaptive optics error, detector readout noise etc can introduce quasi-static background speckles noise. These background speckle interferes with the satellite spots and thus form spots which are not true replicas of the host star. The intensity of the resultant spot thus formed comprises of the actual intensity of the satellite spot, background speckle(incoherent) and the coherent intensity due to their interference. The phase of the satellite spot is switched between 0 and π within an exposure, time averaged to remove the coherent

flux. However, the remaining incoherent flux (i,e A_h^2 in Equation 4 of Jovanovic et al. (2015)[6]) due to the background can create a bias in our flux measurement. A new approach to remove this incoherent background is to measure and subtract them dynamically from the true satellite spot. Subtracting two frames with different speckle patterns gives us an estimate of the amount of incoherent flux lying beneath the satellite spot without losing calibrators for each frame. Subtracting a frame from its closet(or most likely neighboring frame) frame can remove the underlying speckle halo, and then measuring the relative flux can eliminate the effect of Strehl, thus can lead to more accurate photometry.

3. ON-SKY IMPLEMENTATION

In this section, we briefly discuss the implementation of our technique of alternating the speckle pattern in SCExAO-CHARIS system. SCExAO is an extreme Adaptive Optics instrument dedicated towards imaging exoplanets, circumstellar disk and validating technology for future large telescopes. The Coronagraphic High Angular Resolution Imaging Spectrograph (CHARIS)[7] is an integral field spectrograph which takes extreme AO corrected light from SCExAO. Figure 2 gives the schematic representation of the SCExAO bench along with its real picture with all other modules at the Nasmyth platform of Subaru Telescope.

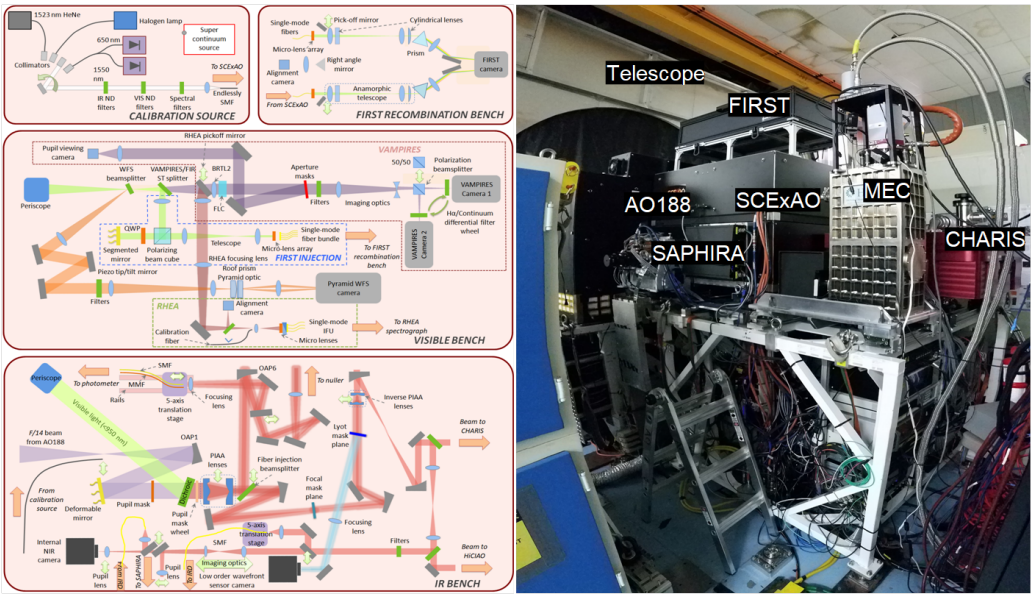

Figure 2. Left: A detailed optical layout the SCExAO bench, Right: The actual picture of the instrument mounted at the Nasmyth IR platform. AO188 gives partially coarse AO corrected light to SCExAO for further fine AO correction (can be seen in the middle,three tier instrument large black box), CHARIS (the red box) with other modules

We applied a sinsusoidal waffle pattern on the MEMs based Deformable Mirror(DM)in SCExAO system to generate artificial satellite spots. The phase of this sinsusoidal pattern was switched between 0 and π at 2kHz to generate incoherent satellite speckle. Between each CHARIS exposures, the grid pattern were switched. Figure 3 shows there consecutive CHARIS frames taken with target HR8799 with different speckle pattern.

On-sky data were taken on the target β-Leo (A3 star type, Hmag =1.92) using low resolution broadband mode(R=18.2) of CHARIS. The raw data were reduced using the CHARIS data reduction pipeline[8]. We applied sinsuoidal wave of amplitude 8.8 nm to create satellite spots which were $\sim 10^3$ times fainter than the central PSF. Regular satellite spots (formed with 50 nm, or 25nm DM amplitude) prevents simultaneous measurement in the visible and infrared regime as these spots tends to get much more brighter in visible instrument(VAMPIRES)and saturate the visible science detector. Also, with the fainter satellite speckle we can achieve higher contrast of the grid spot w.r.t PSF core which can act as an ideal calibrator for faint objects such as exoplanets. Figure 4 left, shows two consecutive CHARIS exposure for the target β-Leo having two alternated speckle patterns where

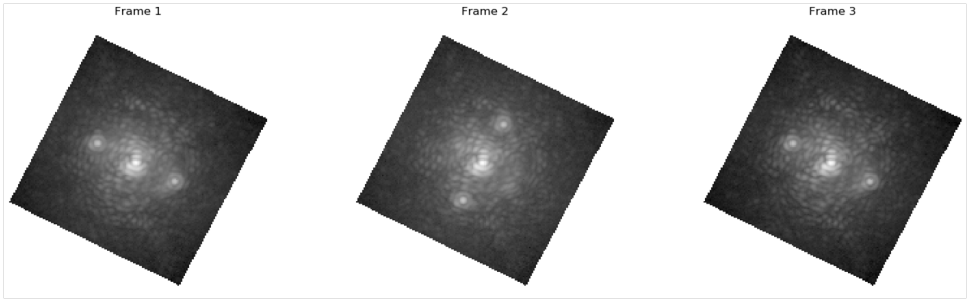

Figure 3. Images of three consecutive reduced data slices of HR8799 obtained from CHARIS at 1630 nm showing two alternate speckle pattern for illustration of our technique.

the grid spots are barely visible. The spots are placed at a separation of $11.25\lambda/D$ from the PSF center. While figure 4 right, shows the subtracted images of these frames where this speckle pattern are clearly visible. The flux and position of this subtracted speckle spots were measured using aperture photometry.

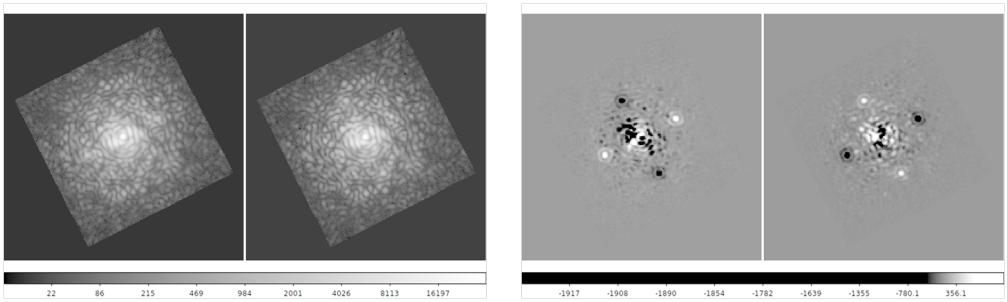

Figure 4. Left: Images of two consecutive reduced data slices of β Leo obtained from CHARIS at 1744 nm with two alternate fainter speckle patterns where they are barely visible. Right: Images of the same two data slices after subtraction frame. After subtracting two consecutive frames, the calibration speckles can be clearly seen.

The fluxes of these speckle grid flux (after subtraction) were measured to a precision of approximately 5% in H-band for 10 sec frame exposure over a period of 10 minutes. We also obtained a photometry precision of $\sim$7% in the ratio of fluxes of a pair of satellite speckle in an exposure. Assuming random background level, the error in the measurement of companion to host flux ratio directly scales to the error associated with the companion and satellite spot flux measurement. Therefore, we infer that the companion and host star contrast can be measured to an accuracy of 7%. Further, this precision increases with more number of data frames, indicating that our measurement has no significant biased background level.

4. CONCLUSION

In this article we discussed the importance of satellite spots in post-coronagraphic images and the need to change their patterns for each exposures. We deployed artificial incoherent satellite spots with alternating pattern on a high resolution integral field spectrometer to do precision photometry. This technique aims at improving the stability of satellite spots where the background level is dominated by quasi-static speckles. We demonstrated a practical solution to photometric calibration challenging in high contrast imaging. This technique is applicable for orbits, spectra and time variation measurements from high contrast images.

ACKNOWLEDGMENTS

The development of SCExAO was supported by the Japan Society for the Promotion of Science (Grant-in-Aid for Research #23340051, #26220704, #23103002, #19H00703 & #19H00695), the Astrobiology Center of the

National Institutes of Natural Sciences, Japan, the Mt Cuba Foundation and the director's contingency fund at Subaru Telescope. F. Martinache's work is supported by the ERC award CoG - 683029. The authors would like to acknowledge the support from Subaru Telescope for lending out their facility. The authors recognize the significant cultural role and reverence that the summit of Maunakea has always had within the native Hawaiian community. We are fortunate to have the opportunity conduct the observations from this mountain.

References

1. B Macintosh et al. First light of the gemini planet imager. *Proceedings of the National Academy of Sciences*,111(35):12661-12666, 2014. ISSN 0027-8424. doi: 10.1073/pnas.1304215111.

2. J.L. Beuzit et al. Sphere: a 'planet finder' instrument for the vlt. *Ground-based and Airborne Instrumentation for Astronomy II*, volume 7014, page 701418, 2008. doi: 10.1117/12.790120.

3. Jared R. Males et al. Magao-x: project status and first laboratory results, 2006. URL https://doi.org/10.1117/12.2312992.

4. N. Jovanovic et al. The subaru coronagraphic extreme adaptive optics system: Enabling high-contrast imaging on solar system scales. *Publications of the Astronomical Society of the Pacific*, 127(955):890, 2015b. URL http://stacks.iop.org 1538-3873/127/i=955/a=890.

5. Anand Sivaramakrishnan and Ben R. Oppenheimer. Astrometry and photometry with coronagraphs. *The Astrophysical Journal*, 647(1):620, 2006. URL http:// stacks.iop.org/ 0004-637X/647/i=1/a=620.

6. N. Jovanovic, O. Guyon, F. Martinache, P. Pathak, J. Hagelberg, and T. Kudo. Artificial incoherent speckles enable precision astrometry and photometry in high-contrast imaging. *The Astrophysical Journal Letters*, 813(2):L24, 2015a. URL http://stacks.iop.org/2041-8205/813/i=2/a=L24.

7. T. Groff et al. First light of the charis high-contrast integral field spectrograph. *Society of Photo Optical Instrumentation Engineers (SPIE) Conference Series, volume 10400 of Society of Photo-Optical Instrumentation Engineers (SPIE) Conference Series*, page 1040016, sep 2017. doi: 10.1117/12.2273525.

8. Timothy D. Brandt et al. Data reduction pipeline for the charis integral field spectrograph i: detector readout calibration and data cube extraction. *Journal of Astronomical Telescopes, Instruments, and Systems*, 3:048002, 2017. doi: 10.1117/1.JATIS.3.4.048002.

Subaru Coronagraphic Extreme-AO (SCExAO) wavefront control: current status and ongoing developments

Ananya Sahoo, Olivier Guyon, Christophe S. Clergeon, Nour Skaf, Yosuke Minowa, et al.

Ananya Sahoo, Olivier Guyon, Christophe S. Clergeon, Nour Skaf, Yosuke Minowa, Julien Lozi, Nemanja Jovanovic, Frantz Martinache , "Subaru Coronagraphic Extreme-AO (SCExAO) wavefront control: current status and ongoing developments," Proc. SPIE 10703, Adaptive Optics Systems VI, 1070350 (11 July 2018); doi: 10.1117/12.2314333

SPIE.

Event: SPIE Astronomical Telescopes + Instrumentation, 2018, Austin, Texas, United States

Subaru Coronagraphic Extreme-AO (SCExAO) Wavefront Control: Current Status and Ongoing Developments

Ananya Sahoo[a,b], Olivier Guyon[a,e,f,g], Christophe S. Clergeon[a], Nour Skaf[a], Yosuke Minowa[a], Julien Lozi[a], Nemanja Jovanovic[c], Frantz Martinanche[d]

[a]Subaru Telescope, National Astronomical Observatory of Japan, 650 North A'ohoku Place, Hilo, HI 96720, U.S.A.
[b]SOKENDAI(The Graduate University of Advanced Studies), Department of Astronomical Sciences, 2-21-1 Osawa, Mitaka, Tokyo 181-8588, Japan
[c]Caltech Optical Observatories, California Institute of Technology, 1200 E. California Boulevard,Pasadena, CA 91125, U.S.A
[d]Observatoire de la Cote dAzur, 96 Boulevard de lObservatoire, 06300 Nice, France
[e]College of Optical Sciences, University of Arizona, Tucson, AZ 85721, U.S.A.
[f]Jet Propulsion Laboratory, 4800 Oak Grove Drive, MS 183-901, Pasadena, CA 91109, U.S.A.
[g]Astrobiology Center of NINS, 2-21-1, Osawa, Mitaka, Tokyo, 181-8588, Japan

Abstract. Exoplanet imaging requires excellent wavefront correction and calibration. At the Subaru telescope this is achieved using the 188-element facility adaptive optics system(AO188) feeding the Subaru Coronagraphic Extreme Adaptive Optics (SCExAO) instrument; a multipurpose instrument built to deliver high contrast images of planets and disks around nearby stars. AO188 offers coarse correction while SCExAO performs fine correction and calibration of 1000 modes. The full system achieves $\sim$90$\%$Strehl Ratio in H-band and diffraction limited images. A new Real Time Computer allowing higher performance between SCExAO and AO188 is currently implemented. Future upgrades will include a new Pyramid Wavefront Sensor and (64x64) DM to achieve extreme AO correction inside AO188. We are progressing in the development of predictive control and sensor fusion algorithms across the system to improve performance and calibration. With the new upgrades, SCExAO will be able to image giant plan-ets in reflected light with Subaru and validate technologies necessary to image habitable Earth-like planets with the Thirty Meter Telescope (TMT).

Keywords: adaptive optics, exoplanet, wavefront sensors, astronomical instrumentations, wavefront control.

1 Introduction

Direct imaging of nearby exoplanets and the circumstellar disks can give crucial information about their atmospheric composition and can refine our understanding of planetary formation. These planetary mass companions typically within small angular separations are between 4 and 10 orders of magnitude fainter than their host star and makes direct imaging to be challenging. Extreme AO with coronagraphs are deployed in ground based telescopes to mitigate these challenges. The Subaru Coronagraphic Extreme Adaptive (SCExAO) is one such instruments.[1] It combines multiple wavefront sensor techniques with several state-of-the-art coronagraphs such as vector vortex coronagraph,[2] Phase Induced Amplitude Apodization (PIAA)[3] coronagraph to push the inner working angle (IWA) to less than λ/D. SCExAO takes light from the 188-element facility adaptive optics system (AO188)[4] which gives a partial correction of low order modes and feeds an integral field spectrograph CHARIS(Coronagraphic High Angular Resolution Spectrograph) at the IR Nasmyth platform of the Subaru Telescope. AO188 is comprised of a curvature based wavefront sensor which runs at 1KHz with Avalanch Photodiodes (APDs) and a 188-actuator bi-morph deformable mirror (DM) to achieve Strehl ratios (SR) up to 30-40 $\%$ in H band. A wavefront control system is the heart of operation of any extreme AO systems and act as key for high contrast imaging. SCExAO comprises of a pyramid based high order wavefront sensor (PyWFS) to measure higher order modes up to 1000 and a Lyot based low order wavefront sensor to identify low order modes such as tip-tilt, coma, defocus, astigmatism etc. The wavefront correction is performed by a MEM technology based 2000-actuator Deformable Mirror (DM) running at upto 3.5KHz. It is operated by a wavefront control algorithm using high sensitivity PyWFS to suppress the speckle noise. The current optical system is capable of achieving $\sim$ 90 Strehl Ratio(SR) in H-band and delivers diffraction limited images in visible light. Future plans include upgrading AO188's software and hardware components. We are currently implementing a new Real Time Computer (RTC) to

Adaptive Optics Systems VI, edited by Laird M. Close, Laura Schreiber, Dirk Schmidt, Proc. of SPIE Vol. 10703, 1070350 · © 2018 SPIE
CCC code: 0277-786X/18/$18 · doi: 10.1117/12.2314333

allow for higher performance real time communications between SCExAO and AO188. Future upgrades will include new PyWFS and new (64x64)DM to achieve extreme AO correction inside AO188, so that SCExAO's DM can be focused on the fine control and calibration of speckle noise. Presently, we are progressing in the development of predictive control and sensor fusion algorithms across the system to improve performance and calibration. SCExAO acts as an ideal platform to demonstrate technologies needed for future large telescopes.

2 SCExAO's Wavefront Control Architecture

Wavefront control primarily comes in two stages, a wavefront sensor and then wavefront corrector. The former measures the phase error and sends commands to the later rectify these errors. Figure 1 shows a schematic representation of the overall wavefront control architecture of SCExAO. It has several loops correcting different regions of the wavefront residuals. SCExAO feeds partially corrected light (600-2500 nm) from AO188. The 2k deformable mirror splits the light in two parts. The visible light (600-950 nm) is reflected to the visible bench which hosts the PyWFS and the rest of the light The IR light that is transmitted by the dichroic to the Infrared IR bench propagates through the coronagraphs and then to the science instruments. Some of the light which is reflected from the coronagraphs is used to drive Lyot based low order wavefront sensor (LLOWFS). It corrects chromatic and non common path errors such as tip/tilt between the visible and Infrared (IR) bench.

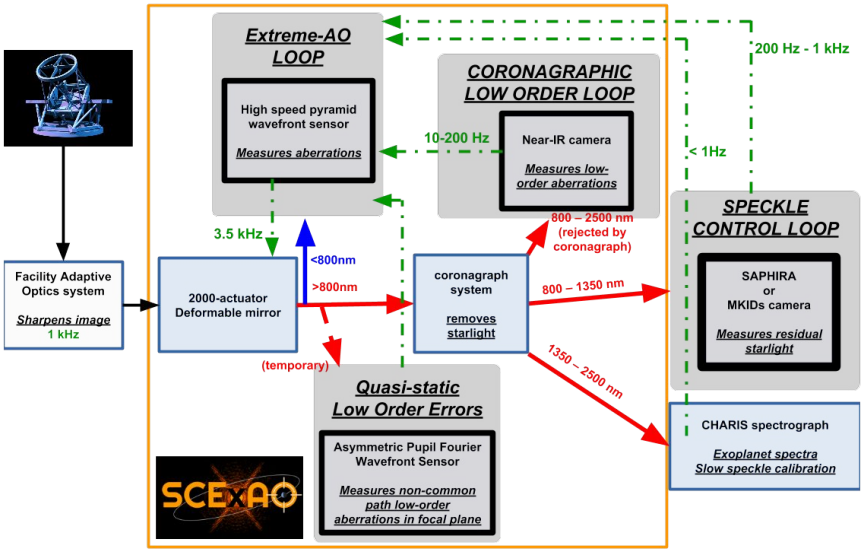

Fig 1 Schematic representation of SCExAO's wavefront control architecture

The 2k-actuator MEMs technology based deformable mirror has a controllable silicon reflective surface to correct distorted input wavefront. It is enclosed in a sealed chamber to control its environment. There are 45×45:5 actuators across the 18 mm beam therefore spatial frequencies out to $22.5\lambda/D$ from the PSF can be addressed. Figure 2 shows the actual picture of the DM installed on the SCExAO bench.

Since PyWFS has high sensitivity and large dynamic range, it chosen as the ExAO primary loop of the SCExAO's wavefront control system which sends the final commands to the DM.[5,6] Other Wavefront sensors' commands to the DM ,are sent as an offset to this PyWFS loop. The DM commands coming from the various sources are then co-added into a single DM map that is sent to the DM. Figure 6 shows various loop which sends command to the DM. The light in front of the PyWFS is modulated in circular trajectory using a tip tilt mirror to increase the to increase the range in which PyWFS responds linearly to

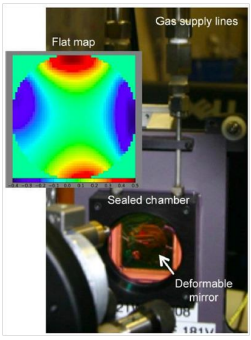

Fig 2 Deformable mirror mounted on SCExAO bench

the aberrations. Figure 3 Shows a picture of the pyramid optics. This loop corrects aberrations up to 1200 modes.

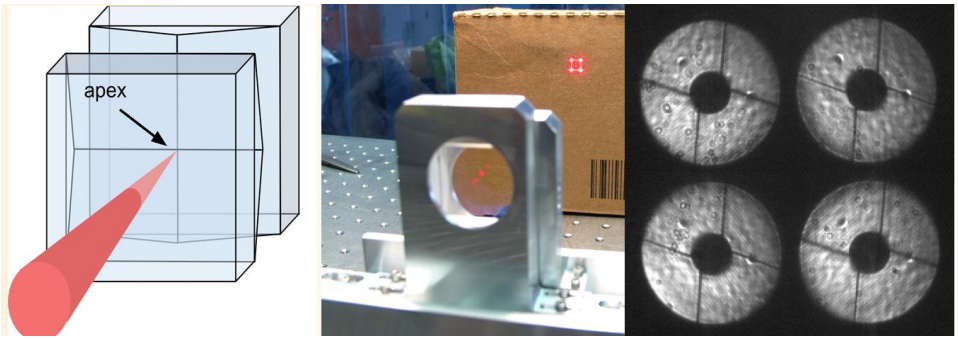

Fig 3 Image of the PyWFS prism with the four pupil images taken with camera OCAM2k

In addition to the ExAO loop, LLOWFS loop addresses the non-common path and chromatic low-order errors between the visible PyWFS and the IR coronagraphs. The light diffracted (see figure 4) by the focal plane masks of the coronagraphs is used by the LLOWFS to correct tip/tilt aberrations by taking into considerations asymmetries in the image.[7]

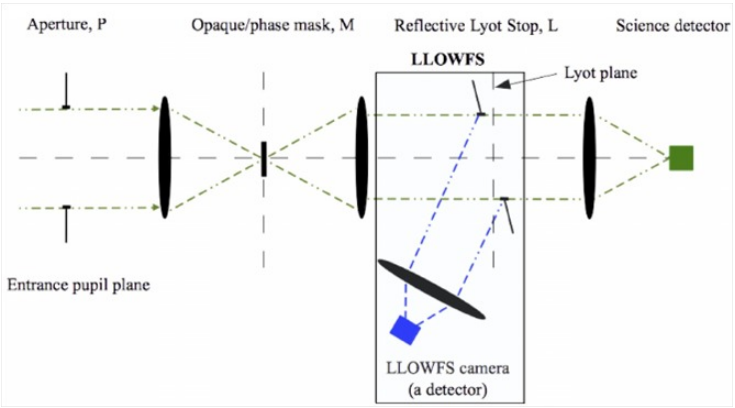

Fig 4 Schematic representation of the Lyot-based low order wavefront sensor (LLOWFS) with a high performance coronagraph and reflective Lyot stop (RLS.

In addition to the PyWFS and LLOWFS several other wavefront sensing techniques are implemented for statics and dynamic high-order aberrations. One such technique is known as focal plane wavefront sensing.[8] It is used to improve the contrast in the image by eliminating the speckles in the PSF (speckle nulling). The DM is modulated to generate speckles which interfere destructively with the speckles already present in the image. The brightest speckles are identified in the image, for which amplitudes and positions are measured. With these informations, speckles are created using sine waves on the DM, at the exact same spatial frequencies, and with similar amplitudes. The phase of the sinusoidal wave is varied. For a particular phase of the applied sinusoidal wave, the total intensity of the speckle becomes negligible. A few tens of speckles are corrected at the same time, and the control is performed in an iterative loop until the maximum contrast is reached. This method only allow the correction on one half of the speckle field when only one DM is used. Figure 5 shows the on sky result achieved with speckle nulling technique.

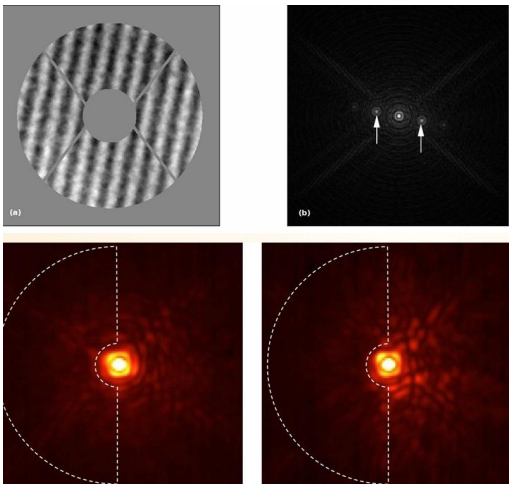

Fig 5 Top:Sinusoidal phase modulation is applied to DM to create speckles. Bottom: Left picture shows the PSF without speckle nulling and right image depicts speckle nulling performed on the region enclosed by white dashed line.

Further, the addition of artificial speckles to the focal plane image can be utilized for precision astrometry when the on-axis starlight has been suppressed post-coronagraph. Speckles can be made incoherent with the speckle in the halo by modulating their phase for superior astrometric performance. We can also measure the contrast of the companion by calibrating the flux ratio between the PSF core and the speckles.[9]

3 Future Upgrade

In order to improve the overall Subaru's AO performance, a few upgrades have been planed for AO188 and SCExAO. Presently there is a lack of communication between the two instruments. This limits us from sending any commands to the DM and transferring any telemetry between the instruments. The hardware and software of AO188 are relatively old and may obstruct us to achieve an optimal wavefront correction. A new Real Time Computer (RTC) is being currently in a phase of tests to make it compatible with the old RTC's hardware. The software upgrade for AO188 includes the use of GPUs for fast real-time computations. The curvature wavefront sensor of AO188 using APDs will be upgraded with a PyWFS, similar to the one inside SCExAO, with a First Light Imaging OCAM2K camera as the detector. The 188-actuator bimoprh DM will be replaced with a 64x64-actuator DM, twill give AO188 ExAO capabilities even without SCExAO. In this configuration, SCExAO's 2000-actuator DM would be exclusively used for speckle control to achieve higher contrast in one half of the image. A new predictive control algorithm is being implemented to reproduce future WFS measurements by linear combination of past WFS measurements for

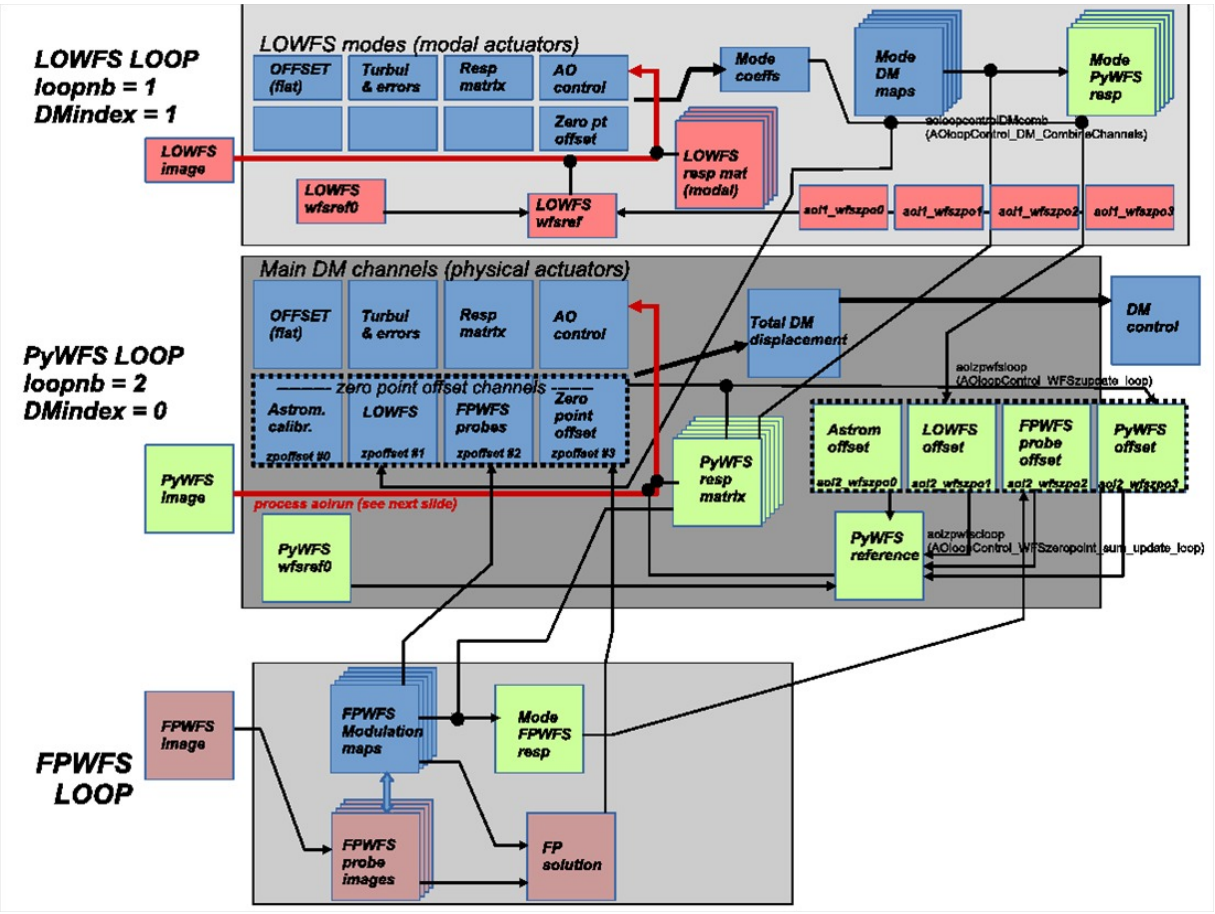

Fig 6 Schematic representation of the SCExAO's wavefront control architecture software. It shows the interactions between the various wavefront control loops. Blue boxes depicts commands in DM space, while green boxes are images in WFS space. The main loop uses the the PyWFS and sends commands to the DM. The DM commands coming from the various sources are then co-added into a single DM map that is sent to the DM.

optimal wavefront corrections.[10] The hardware upgrades of SCExAO includes installation of an Infrared camera; First Light Imaging CRED-2 and a Microwave Kinetic Inductance Detector (MKID)[11] which is a photon counting, energy discriminating in near Infrared. Both these cameras have a low readout noise and can be used for active speckle suppression. These upgrades will make the combination AO188 and SCExAO the ultimate testbed for a first generation high-contrast imager for future large telescopes.

4 Conclusion

The extreme adaptive optics system of SCExAO delivers the necessary wavefront correction and can push the detection limit for ground based telescopes to smaller inner working angles. SCExAO performs fine correction and calibration of $\sim$1000 modes. With the ExAO loop, the current system is capable of achieving $\sim$90% Strehl Ratio in H-band and delivers diffraction limited images in visible light. There has been progress in the development of predictive control and sensor fusion algorithms across the system to improve performance and calibration.With the new upgrades SCExAO will be able to image giant planets in reflected light with Subaru and validate technologies necessary to image habitable Earth-like planets with the Thirty Meter Telescope(TMT).

References

1 N. Jovanovic, F. Martinache, O. Guyon, *et al.*, "The subaru coronagraphic extreme adaptive optics system: Enabling high-contrast imaging on solar-system scales," *Publications of the Astronomical Society of the Pacific* **127**(955), 890 (2015).

2 D. Mawet, E. Serabyn, K. Liewer, *et al.*, "The vector vortex coronagraph: Laboratory results and first light at palomar observatory," *The Astrophysical Journal* **709**(1), 53 (2010).

3 O. Guyon, "Phase - induced amplitude apodization of telescope pupils for extrasolar terrestrial planet imaging," *Astron. Astrophys.* **404**, 379 (2003).

4 Y. Minowa, Y. Hayano, S. Oya, *et al.*, "Performance of subaru adaptive optics system ao188," in *Proceedings of SPIE - The International Society for Optical Engineering*, **7736** (2010).

5 O. Guyon, "Limits of adaptive optics for high contrast imaging," *Astrophys. J.* **629**, 592–614 (2005).

6 C. Clergeon, O. Guyon, F. Martinache, *et al.*, "The subaru coronagraphic extreme ao high speed and high sensitivity wavefront sensors," in *Proceedings of the Third AO4ELT Conference*, S. Esposito and L. Fini, Eds., INAF - Osservatorio Astrofisico di Arcetri, (Firenze) (2013).

7 G. Singh, F. Martinache, P. Baudoz, *et al.*, "Lyot-based low order wavefront sensor for phase-mask coronagraphs: Principle, simulations and laboratory experiments," *Publications of the Astronomical Society of the Pacific* **126**(940), 586 (2014).

8 F. Martinache, O. Guyon, N. Jovanovic, *et al.*, "On-sky speckle nulling demonstration at small angular separation with scexao," *Publications of the Astronomical Society of the Pacific* **126**(940), 565 (2014).

9 N. Jovanovic, O. Guyon, F. Martinache, *et al.*, "Artificial incoherent speckles enable precision astrometry and photometry in high-contrast imaging," *The Astrophysical Journal Letters* **813**(2), L24 (2015).

10 O. Guyon and J. Males, "Adaptive Optics Predictive Control with Empirical Orthogonal Functions (EOFs)," *ArXiv e-prints* (2017).

11 B. A. Mazin, B. Bumble, S. R. Meeker, *et al.*, "A superconducting focal plane array for ultraviolet, optical, and near-infrared astrophysics," *Opt. Express* **20**, 1503–1511 (2012).

References

Apai, Dániel et al. (2016). "High-cadence, high-contrast imaging for exoplanet mapping: Observations of the HR 8799 planets with VLT/SPHERE satellite-spot-corrected relative photometry". In: *The Astrophysical Journal* 820.1, p. 40.

Babcock, Horace W (1953). "The possibility of compensating astronomical seeing". In: *Publications of the Astronomical Society of the Pacific* 65.386, pp. 229–236.

Barstow, Joanna K and Patrick GJ Irwin (2016). "Habitable worlds with JWST: transit spectroscopy of the TRAPPIST-1 system?" In: *Monthly Notices of the Royal Astronomical Society: Letters* 461.1, pp. L92–L96.

Bessell, MS, F Castelli, and Bertrand Plez (1998). "Model atmospheres broad-band colors, bolometric corrections and temperature calibrations for O-M stars". In: *Astronomy and astrophysics* 333, pp. 231–250.

Beuzit, J.L. et al. (2008). "SPHERE: a 'Planet Finder' instrument for the VLT". In: *Ground-based and Airborne Instrumentation for Astronomy II*. Vol. 7014, p. 701418. DOI: 10.1117/12.790120.

Brandt, Timothy D et al. (2017). "Data reduction pipeline for the CHARIS integral-field spectrograph I: detector readout calibration and data cube extraction". In: *Journal of Astronomical Telescopes, Instruments, and Systems* 3.4, p. 048002.

Cameron, PB, MC Britton, and SR Kulkarni (2008). "Precision astrometry with adaptive optics". In: *The Astronomical Journal* 137.1, p. 83.

Canovas, H et al. (2013). "Near-infrared imaging polarimetry of HD 142527". In: *Astronomy & Astrophysics* 556, A123.

Chiang, E et al. (2009). "Fomalhaut's debris disk and planet: constraining the mass of Fomalhaut b from disk morphology". In: *The Astrophysical Journal* 693.1, p. 734.

Day, Peter K et al. (2003). "A broadband superconducting detector suitable for use in large arrays". In: *Nature* 425.6960, pp. 817–821.

Digby, Andrew P et al. (2006). "The challenges of coronagraphic astrometry". In: *The Astrophysical Journal* 650.1, p. 484.

Fabrycky, Daniel C and Ruth A Murray-Clay (2010). "Stability of the directly imaged multiplanet system HR 8799: resonance and masses". In: *The Astrophysical Journal* 710.2, p. 1408.

Finger, Gert et al. (2008). "Performance evaluation, readout modes, and calibration techniques of HgCdTe Hawaii-2RG mosaic arrays". In: *High Energy, Optical, and Infrared Detectors for Astronomy III*. Vol. 7021. International Society for Optics and Photonics, 70210P.

Fried, David L (1966). "Optical resolution through a randomly inhomogeneous medium for very long and very short exposures". In: *JOSA* 56.10, pp. 1372–1379.

Girardi, Léo et al. (2002). "Theoretical isochrones in several photometric systems-I. Johnson-Cousins-Glass, HST/WFPC2, HST/NICMOS, Washington, and ESO Imaging Survey filter sets". In: *Astronomy & Astrophysics* 391.1, pp. 195–212.

Groff, T. et al. (Sept. 2017). "First light of the CHARIS high-contrast integral-field spectrograph". In: *Society of Photo-Optical Instrumentation Engineers (SPIE) Conference Series*. Vol. 10400. Society of Photo-Optical Instrumentation Engineers (SPIE) Conference Series, p. 1040016. DOI: 10.1117/12.2273525.

Groff, Tyler D et al. (2016). "Laboratory testing and performance verification of the CHARIS integral field spectrograph". In: *Ground-based and Airborne Instrumentation for Astronomy VI*. Vol. 9908. International Society for Optics and Photonics, 99080O.

Guyon, Olivier (2018). "Extreme adaptive optics". In: *Annual Review of Astronomy and Astrophysics* 56, pp. 315–355.

Guyon, Olivier, Basile Gallet, et al. (2006). "High contrast imaging with focal plane wavefront sensing for ground based telescopes". In: *Advances in Adaptive Optics II*. Vol. 6272. International Society for Optics and Photonics, p. 62723C.

Guyon, Olivier, EA Pluzhnik, et al. (2006). "Theoretical limits on extrasolar terrestrial planet detection with coronagraphs". In: *The Astrophysical Journal Supplement Series* 167.1, p. 81.

Hardy, John W (1998). *Adaptive optics for astronomical telescopes*. Vol. 16. Oxford University Press on Demand.

Hartmann, J (1900). "Bermerkungen über den bau und die justierung von spektrographen". In: *Zeitschrift für Instrumentenkunde* 20, p. 47.

Hayano, Yutaka, Hideki Takami, Olivier Guyon, et al. (2008). "Current status of the laser guide star adaptive optic system for Subaru Telescope". In: *Adaptive Optics Systems*. Vol. 7015. International Society for Optics and Photonics, p. 701510.

Hayano, Yutaka, Hideki Takami, Shin Oya, et al. (2010). "Commissioning status of Subaru laser guide star adaptive optics system". In: *Adaptive Optics Systems II*. Vol. 7736. International Society for Optics and Photonics, 77360N.

Huby, Elsa et al. (2012). "First, a fibered aperture masking instrument-i. first on-sky test results". In: *Astronomy & Astrophysics* 541, A55.

Ichikawa, Takashi et al. (2006). "MOIRCS: multi-object infrared camera and spectrograph for SUBARU". In: *Ground-based and Airborne Instrumentation for Astronomy*. Vol. 6269. International Society for Optics and Photonics, p. 626916.

Jenkins, Jon M et al. (2015). "Discovery and validation of Kepler-452b: a 1.6 R $\bigoplus$ super Earth exoplanet in the habitable zone of a G2 star". In: *The Astronomical Journal* 150.2, p. 56.

Jovanovic, N. et al. (2015a). "The Subaru Coronagraphic Extreme Adaptive Optics System: Enabling High-Contrast Imaging on Solar-System Scales". In: *Publications of the Astronomical Society of the Pacific* 127.955, p. 890. URL: http://stacks.iop.org/1538-3873/127/i=955/a=890.

Jovanovic, N. et al. (2015b). "Artificial Incoherent Speckles Enable Precision Astrometry and Photometry in High-contrast Imaging". In: *The Astrophysical Journal Letters* 813.2, p. L24. URL: http://stacks.iop.org/2041-8205/813/i=2/a=L24.

Kalas, Paul et al. (2008). "Optical images of an exosolar planet 25 light-years from Earth". In: *science* 322.5906, pp. 1345–1348.

Kashikawa, Nobunari et al. (2000). "FOCAS: faint object camera and spectrograph for the Subaru Telescope". In: *Optical and IR Telescope Instrumentation and Detectors*. Vol. 4008. International Society for Optics and Photonics, pp. 104–113.

Kataza, Hirokazu et al. (2000). "COMICS: the cooled mid-infrared camera and spectrometer for the Subaru telescope". In: *Optical and IR Telescope Instrumentation and Detectors*. Vol. 4008. International Society for Optics and Photonics, pp. 1144–1152.

Kobayashi, Naoto et al. (2000). "IRCS: infrared camera and spectrograph for the Subaru Telescope". In: *Optical and IR Telescope Instrumentation and Detectors*. Vol. 4008. International Society for Optics and Photonics, pp. 1056–1066.

Kotani, Takayuki, Motohide Tamura, Jun Nishikawa, et al. (2018). "The infrared Doppler (IRD) instrument for the Subaru telescope: instrument description and commissioning results". In: *Ground-based and Airborne Instrumentation for Astronomy VII*. Vol. 10702. International Society for Optics and Photonics, p. 1070211.

Kotani, Takayuki, Motohide Tamura, Hiroshi Suto, et al. (2014). "Infrared Doppler instrument (IRD) for the Subaru telescope to search for Earth-like planets around nearby M-dwarfs". In: *Ground-based and Airborne Instrumentation for Astronomy V*. Vol. 9147. International Society for Optics and Photonics, p. 914714.

Lovis, Christophe and Debra Fischer (2010). "Radial velocity techniques for exoplanets". In: *Exoplanets*, pp. 27–53.

Lozi, Julien et al. (2018). "SCExAO, an instrument with a dual purpose: perform cutting-edge science and develop new technologies". In: *Adaptive Optics Systems VI*. Vol. 10703. International Society for Optics and Photonics, p. 1070359.

Lyot, Bernard (1939). "The study of the solar corona and prominences without eclipses (George Darwin Lecture, 1939)". In: *Monthly Notices of the Royal Astronomical Society* 99, p. 580.

Madhusudhan, Nikku, Adam Burrows, and Thayne Currie (2011). "Model atmospheres for massive gas giants with thick clouds: Application to the HR 8799 planets and predictions for future detections". In: *The Astrophysical Journal* 737.1, p. 34.

Males, Jared R. et al. (2006). *MagAO-X: project status and first laboratory results*. DOI: 10.1117/12.2312992. URL: https://doi.org/10.1117/12.2312992.

Marcy, Geoffrey W and R Paul Butler (1996). "A planetary companion to 70 Virginis". In: *The Astrophysical Journal Letters* 464.2, p. L147.

Marley, Mark S and Sujan Sengupta (2011). "Probing the physical properties of directly imaged gas giant exoplanets through polarization". In: *Monthly Notices of the Royal Astronomical Society* 417.4, pp. 2874–2881.

Marois, Christian, René Doyon, et al. (2000). "Efficient speckle noise attenuation in faint companion imaging". In: *Publications of the Astronomical Society of the Pacific* 112.767, p. 91.

Marois, Christian, David Lafreniere, René Doyon, et al. (2006). "Angular differential imaging: a powerful high-contrast imaging technique". In: *The Astrophysical Journal* 641.1, p. 556.

Marois, Christian, David Lafreniere, Bruce Macintosh, et al. (2006). "Accurate astrometry and photometry of saturated and coronagraphic point spread functions". In: *The Astrophysical Journal* 647.1, p. 612.

Marois, Christian, Bruce Macintosh, et al. (2008). "Direct imaging of multiple planets orbiting the star HR 8799". In: *science* 322.5906, pp. 1348–1352.

Marois, Christian, B Zuckerman, et al. (2010). "Images of a fourth planet orbiting HR 8799". In: *Nature* 468.7327, pp. 1080–1083.

Martinache, Frantz, Nemanja Jovanovic, and Olivier Guyon (2016). "Closed-loop focal plane wavefront control with the SCExAO instrument". In: *Astronomy & Astrophysics* 593, A33.

Mayor, Michel and Didier Queloz (1995). "A Jupiter-mass companion to a solar-type star". In: *Nature* 378.6555, pp. 355–359.

Mazin, Ben (2014). "MKIDs for TMT". In: *tmt*, p. 23.

Minowa, Yosuke et al. (2010). "Performance of Subaru adaptive optics system AO188". In: *Adaptive Optics Systems II*. Vol. 7736. International Society for Optics and Photonics, 77363N.

Miyazaki, Satoshi et al. (2018). "Hyper Suprime-Cam: System design and verification of image quality". In: *Publications of the Astronomical Society of Japan* 70.SP1, S1.

Nakajima, Tadashi (1994). "Planet detectability by an adaptive optics stellar coronagraph". In: *The Astrophysical Journal* 425, pp. 348–357.

Noguchi, Kunio et al. (2002). "High dispersion spectrograph (HDS) for the Subaru telescope". In: *Publications of the Astronomical Society of Japan* 54.6, pp. 855–864.

Norris, B. et al. (Jan. 2015). "The VAMPIRES instrument: imaging the innermost regions of protoplanetary discs with polarimetric interferometry". In: *Monthly Notices of the Royal Astronomical Society* 447.3, pp. 2894–2906. ISSN: 0035-8711. DOI: 10.1093/mnras/stu2529.

Norris, Barnaby RM et al. (2012). "A close halo of large transparent grains around extreme red giant stars". In: *Nature* 484.7393, pp. 220–222.

Okamoto, Yoshiko Kataza et al. (2003). "Improved performances and capabilities of the Cooled Mid-Infrared Camera and Spectrometer (COMICS) for the Subaru Telescope". In: *Instrument Design and Performance for Optical/Infrared Ground-based Telescopes*. Vol. 4841. International Society for Optics and Photonics, pp. 169–180.

Oppenheimer, Ben R et al. (2004). "The Lyot project: toward exoplanet imaging and spectroscopy". In: Society of Photo-optical Instrumentation Engineers (SPIE).

Perryman, Michael (2018). *The exoplanet handbook*. Cambridge University Press.

Platt, Ben C and Roland Shack (2001). "History and principles of Shack-Hartmann wavefront sensing". In: *Journal of refractive surgery* 17.5, S573–S577.

Racine, René et al. (1999). "Speckle noise and the detection of faint companions". In: *Publications of the Astronomical Society of the Pacific* 111.759, p. 587.

Ragazzoni, Roberto (1996). "Pupil plane wavefront sensing with an oscillating prism". In: *Journal of modern optics* 43.2, pp. 289–293.

Ragazzoni, Roberto and J Farinato (1999). "Sensitivity of a pyramidic wave front sensor in closed loop adaptive optics". In: *Astronomy and Astrophysics* 350, pp. L23–L26.

Roddier, Francois (1988). "Curvature sensing and compensation: a new concept in adaptive optics". In: *Applied Optics* 27.7, pp. 1223–1225.

Roddier, François (1999). *Adaptive optics in astronomy*. Cambridge university press.

Roelfsema, Ronald et al. (2010). "The ZIMPOL high-contrast imaging polarimeter for SPHERE: design, manufacturing, and testing". In: *Ground-based and Airborne Instrumentation for Astronomy III*. Vol. 7735. International Society for Optics and Photonics, 77354B.

Rousset, G et al. (1990). "First diffraction-limited astronomical images with adaptive optics". In: *Astronomy and Astrophysics* 230, pp. L29–L32.

Sahoo, Ananya et al. (2018). "Subaru Coronagraphic Extreme-AO (SCExAO) wavefront control: current status and ongoing developments". In: *Adaptive Optics Systems VI*. Vol. 10703. International Society for Optics and Photonics, p. 1070350.

Sartoretti, P and J Schneider (1999). "On the detection of satellites of extrasolar planets with the method of transits". In: *Astronomy and Astrophysics Supplement Series* 134.3, pp. 553–560.

Sato, Bun'ei et al. (2002). "Development of iodine cells for the Subaru HDS and the Okayama HIDES: II. New software for precise radial velocity measurements". In: *Publications of the Astronomical Society of Japan* 54.6, pp. 873–882.

Schneider, J (1994). "On the occultations of a binary star by a circum-orbiting dark companion". In: *Planetary and Space Science* 42.7, pp. 539–544.

Seager, Sara and Drake Deming (2010). "Exoplanet atmospheres". In: *Annual Review of Astronomy and Astrophysics* 48, pp. 631–672.

Shack, Roland V (1970). "Image processing by an optical analog device". In: *Pattern Recognition* 2.2, pp. 123–126.

Sivaramakrishnan, Anand, Christopher D Koresko, et al. (2001). "Ground-based coronagraphy with high-order adaptive optics". In: *The astrophysical journal* 552.1, p. 397.

Sivaramakrishnan, Anand and Ben R. Oppenheimer (2006). "Astrometry and Photometry with Coronagraphs". In: *The Astrophysical Journal* 647.1, p. 620. URL: http://stacks.iop.org/0004-637X/647/i=1/a=620.

Strehl, K (1895). "Aplanatische und fehlerhafte Abbildung im Fernrohr". In: *Zeitschrift für Instrumentenkunde* 15.7, pp. 362–370.

Suzuki, Ryuji et al. (2008). "Multi-Object Infrared Camera and Spectrograph (MOIRCS) for the Subaru Telescope* I. Imaging". In: *Publications of the Astronomical Society of Japan* 60.6, pp. 1347–1362.

Tamura, M et al. (2012). "Infrared Doppler instrument for the Subaru telescope (IRD)". In: *Ground-Based and Airborne Instrumentation for Astronomy IV*. Vol. 8446. International Society for Optics and Photonics, 84461T.

Tokunaga, Alan T et al. (1998). "Infrared camera and spectrograph for the SUBARU Telescope". In: *Infrared Astronomical Instrumentation*. Vol. 3354. International Society for Optics and Photonics, pp. 512–524.

Turbet, Martin et al. (2016). "The habitability of Proxima Centauri b-II. Possible climates and observability". In: *Astronomy & Astrophysics* 596, A112.

Tyson, Robert K (2015). *Principles of adaptive optics*. CRC press.

Vievard, S et al. (2019). "Capabilities of a fibered imager on an extremely large telescope". In:

Walter, Alex et al. (2018). "MEC: the MKID exoplanet camera for high contrast astronomy at Subaru (Conference Presentation)". In: *Ground-based and Airborne Instrumentation for Astronomy VII*. Vol. 10702. International Society for Optics and Photonics, p. 107020V.

Wang, Jason J. et al. (2014). "Gemini planet imager observational calibrations VIII: characterization and role of satellite spots". In: vol. 9147. DOI: 10.1117/12.2055753. URL: https://doi.org/10.1117/12.2055753.

Wang, Jason J et al. (2018). "Dynamical constraints on the HR 8799 planets with GPI". In: *The Astronomical Journal* 156.5, p. 192.

Wolszczan, Aleksander and Dail A Frail (1992). "A planetary system around the millisecond pulsar PSR1257+ 12". In: *Nature* 355.6356, pp. 145–147.

Zhou, Yifan et al. (2016). "Discovery of rotational modulations in the planetary-mass companion 2M1207b: intermediate rotation period and heterogeneous clouds in a low gravity atmosphere". In: *The Astrophysical Journal* 818.2, p. 176.

Zimmerman, Neil et al. (2010). "Parallactic motion for companion discovery: An M-dwarf orbiting Alcor". In: *The Astrophysical Journal* 709.2, p. 733.